7-31-2018

Ultrafast and Nonlinear Spectroscopy of Nanomaterials

Rami Anthony Khoury
Louisiana State University and Agricultural and Mechanical College, rkhour1@lsu.edu

ULTRAFAST AND NONLINEAR SPECTROSCOPY OF NANOMATERIALS

A Dissertation

Submitted to the Graduate Faculty of the
Louisiana State University and
Agricultural and Mechanical College
in partial fulfillment of the
requirements for the degree of
Doctor of Philosophy

in

The Department of Chemistry

by
Rami Anthony Khoury
B.S. Louisiana State University, 2012
December 2018

This PhD Dissertation is
Dedicated to
My Mother and Father
Hend and Fouad Khoury

Acknowledgements

I am extremely gracious to Professor Louis Haber for giving me this amazing opportunity and for his valuable guidance and support on research and life. The work in this Ph.D., and furthermore after this Ph.D., would not be possible without Dr. Haber. Thank you for continually inspiring me to work hard.

I am also thankful for my committee members Professor Jayne Garno, Professor Bin Chen, and Professor Phillip Sprunger for their time and insight into my research. Additionally, I would like to thank Professor Ward Plummer, Dr. Mohammad Saghayzhian, Dr. Kun Zhao, and Joel Taylor for their valuable expertise in our collaboration. I am in deep gratitude for Professor Kresimir Rupnik for continually being available for laser help and critical discussions. I am very thankful for Ying Xiao for her help with electron microscopy. I would especially like to thank Dr. Zhenyu Zhang whose guidance helped me grow as an ultrafast scientist. This research would not have been possible without current and former members of the Haber group: Dr. Tony Karam, Dr. Raju Kumal, Dr. Holden Smith, Jeewan Ranasinghe, Asela Dikkumbura, Prakash Hamal, and Min Chen as it has been awesome working with you all.

It's not possible to do your Ph.D. alone and without the help of others. I have to again thank my mother and father Hend and Fouad Khoury as I find motivation through their love and support. Friends and family have been an anchor that I have relied on so I would like to thank my brothers Samir and Shadi Khoury for being the best older siblings I could have asked for. I am grateful for the support of my very close friends Paul Bailey, Dustin Lyons, Riley Vannoy and Brodie Mumphrey. I would also like to thank my former Berkeley housemates Anthony Lopez, Nick Prassas, Veronica Balue,

Bryan Flaherty, Chris Genualdi, and Michela Catena for teaching me more about friendship than I could have ever taught myself. Finally I complete this dissertation as a milestone to share with my family from Nazareth, Israel and Damascus, Syria who provided me with love and support throughout my life.

Table of Contents

List of Figures

Abstract

Ultrafast and nonlinear spectroscopies are implemented in the investigation of excited-state dynamics and structural properties of materials and nanomaterials. In the first study, the excited-state dynamics of size-dependent colloidal TiO_2-Au nanocomposites are investigated using ultrafast transient absorption spectroscopy. The dynamics corresponding to the plasmon depletion band are characterized by electron-phonon and phonon-phonon coupling lifetimes that are observed to be independent of the gold nanocluster shell thickness. The excited-state dynamics corresponding to the interband transition of gold is also spectrally overlapped with the interfacial electron transfer lifetime, which is shown to decrease as the nanocluster shell thickness increases. In the second study, *in-situ* second harmonic generation (SHG), a nonlinear spectroscopic technique, is coupled with extinction spectroscopy to monitor the growth of colloidal gold nanoparticles in real time. The *in-situ* SHG results capture an early stage of the growth process where a large enhancement in the SHG is observed due to the formation of plasmonic hot spots attributed to a rough and uneven nanoparticle surface. In a third project, the ultrafast carrier dynamics of self-assembled $La_{1-x}Sr_xTiO_{3-\delta}$ (LMSO) is studied using ultrafast reflectivity experiments. The measured long-lived phonon-phonon coupling lifetime for the oxygen deficient LSMO thin film indicates that the phonons are the major energy carrier in the system. Residual oscillations of two distinct phonon frequencies are also observed and are superimposed on a biexponential decay. Both oscillatory signals are fit with an exponentially damping sine function in which both frequency and damping times are obtained. In a fourth project, our ultrafast reflectivity setup is modified with an added microscopy component for our

work with the Consortium for Innovation in Manufacturing and Materials (CIMM) to investigate heating and melting dynamics of metals, semiconductors, and metal alloys. Finally, in the last portion of this dissertation, electronic sum-frequency generation spectroscopy is utilized to study the azimuthal angular dependence in α-quartz (0001). This dissertation describes the versatility of these ultrafast and nonlinear spectroscopic techniques through fundamental research on different types of materials and nanomaterials in colloidal suspension and at surfaces.

Chapter 1. Introduction to Spectroscopy

1.1 Ultrafast Spectroscopy

Over the past century, scientists have made major strides creating faster measuring tools on the timescales of atomic and molecular motions in order to study the excited-state relaxation dynamics of molecules and materials.[1] The invention of the laser has allowed us to observe these optically-induced reactions on ultrafast timescales. The fundamental principles that led to the conception of the laser, or light amplified by the stimulated emission of radiation, dates back over a century to Einstein's theoretical description of stimulated emission.[2,3]

The past sixty years have seen remarkable progress in laser technologies. The first q-switched ruby laser, developed in the 1960's, was able to produce pulses in the nanosecond (10^{-9} s) to picosecond (10^{-12} s) timescales.[4] Laser pulses on these timescales, in contrast to continuous wave (CW) laser light, can be achieved through q-switching where an optical element, such as a Pockels cell or an optoacoustic modulator, controls the light building up in the lasing cavity under an electronic trigger to produce a short burst of light. The timing of this trigger determines the power and time duration of the laser pulses.[2] In the 1980's, the dye laser was introduced which was able to produce ultrafast laser pulses on the femtosecond (10^{-15} s) timescale.[5] Since the 1990's, scientists have relied mostly titanium:sapphire (Ti:sapph) lasers for producing ultrafast femtosecond (fs) laser pulses due to their high stability and high damage threshold, utilizing the technique of Kerr-lens mode-locking.[6,7] Kerr-lens mode-locking is achieved when the intense center of a Gaussian beam alters the refractive index of a Kerr medium resulting in a self-focusing beam in the laser cavity, which under correct

alignment, can result in constructive interference of the different cavity modes to produce a pulsetrain of ultrafast femtosecond pulses.[8]

The introduction of Ti:sapph lasers propelled the field of femtochemistry. The average speed of atomic motion is about 1 km/s, or over the distance of an atom, equivalent to approximately one Angstrom per 100 fs.[1] By using sub 100 fs pulses, scientists can take a snapshot of a system at critical transition states to understand the excited-state reaction dynamics of molecules and materials. An important caveat in studying these dynamics is inducing a coherence in the molecule or material sample. When a femtosecond pulse interacts with an atom, molecule, or material, it induces a time-dependent polarization due to the coherent superposition between the ground and excited states.[9] The coherent superposition of ground and excited states is given by

$$\Psi_{coherent}(r,t) = a(t)\varphi_a(r) + b(t)\varphi_b(r) \quad (1.1)$$

where $a(t)$ and $b(t)$ represent quantum mechanical phase factors $e^{(-i\omega_a t)}$ and $e^{(-i\omega_b t)}$, respectively, of the ground and excited states.[1] As time progresses, this induced coherent state dephases through incoherent atomic motions and molecular interactions with the surroundings. This coherence produces critical interference between the light and sample being studied. Without this coherence, an induced polarization is not observed. In ultrafast spectroscopy, femtosecond laser pulses are split into pump and probe pulses where a resonant pump pulse creates a superposition between the ground and excited states within a molecule or material, which is monitored by a weak probe pulse as a function of pump-probe time-delay.[10] Typically, the pump-probe time delay is controlled using a retroreflector or a computer-controlled delay stage, where the time delay is equal to the optical path length difference divided by the speed of light.

1.2 Nonlinear Spectroscopy

Additionally, the field of nonlinear spectroscopy developed from the science of producing intense, ultrafast laser pulses. The interaction of light and matter can be described by a series of linear and nonlinear optical processes. When a time-dependent optical electric field $\tilde{E}(t)$ interacts with an atom, molecule, or material sample, it induces a polarization $\tilde{P}(t)$, or dipole moment per unit of volume, that can be represented by

$$\tilde{P}(t) = \epsilon_0[\chi^{(1)}\tilde{E}(t) + \chi^{(2)}\tilde{E}^2(t) + \chi^{(3)}\tilde{E}^3(t) + \cdots] \quad (1.2)$$

where $\chi^{(1)}$ is the linear susceptibility and where $\chi^{(2)}$ and $\chi^{(3)}$ are the second-order and third-order nonlinear susceptibilities, respectively.[11] In the weak-field regime, the induced polarization scales linearly with the incident electric field, as shown by the first term in Eq. 1.2, and the sample absorbs or scatters the incident electric field linearly as a function of intensity, according to Beer's Law or Rayleigh Scattering. In this case, the higher-order susceptibilities can be neglected. However, with high intensity optical electric-field contributions, higher-order nonlinearities are non-negligible resulting in optical fields that can add together in frequency. Femtosecond laser pulses have sufficient intensity for producing these higher-order nonlinear optical processes.

Second-order nonlinear processes can occur according to two general cases. The first case is sum-frequency generation (SFG) where two incident photons of frequency ω_1 and ω_2 coherently add to produce a third photon with a frequency equal to $\omega_3 = \omega_1 + \omega_2$.[11] The second case is a special condition of sum-frequency generation called second harmonic generation (SHG) where two incident photons of the same frequency ($\omega_1 = \omega_2 = \omega$) produce a third photon at twice the fundamental frequency (2ω), as shown in Figure 1.[12,13]

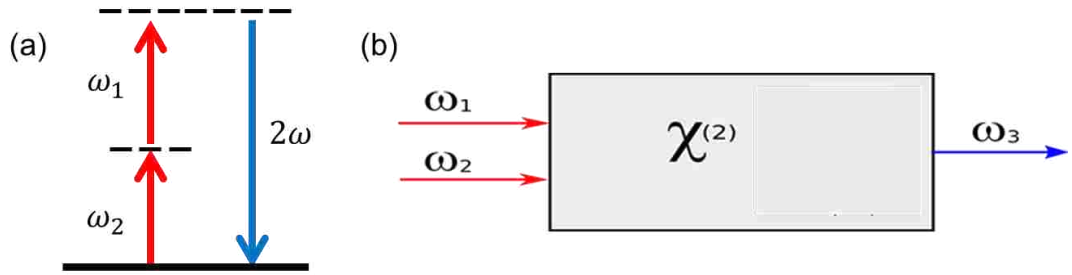

Figure 1.1. (a) Energy-level diagram of SHG. (b) SFG or SHG generated from the second-order nonlinear susceptibility of an atom, molecule, or material.

The second-order polarization $\tilde{P}^{(2)}(t)$ induced from an electric-field $\tilde{E}(t)$ can be written as

$$\tilde{P}^{(2)}(t) = 2\epsilon_0 \chi^{(2)} \tilde{E}^2(t) \tag{1.3}$$

where ϵ_0 is the permittivity in free space and $\tilde{E}(t)$ is an oscillating incident electric field. If we express $\tilde{E}(t)$ as $E_o e^{i\omega t}$ where E_o is the amplitude and ω is the optical frequency, then the second-order polarization here will oscillate at 2ω since it is proportional to $\tilde{E}^2(t)$, resulting in the generation of light at twice the incident frequency, or half the incident wavelength. SHG is typically forbidden in bulk media with a center of inversion symmetry due to resulting cancellations of the optical field.[11] However, this symmetry for centrosymmetric or isotropic systems is broken at an interface making SHG a powerful technique for investigating surfaces, surface chemistry, and nanoparticle interfaces (Figure 1.2).[14] Previous work has used SHG to investigate dye adsorption on gold nanoparticles,[15] the surface charge density of gold nanoparticles,[16] charge-transfer in TiO_2 microparticles,[17] ion transport in liposomes,[18] and metal nanoparticles made of gold, silver, and gold-silver alloys.[19-23]

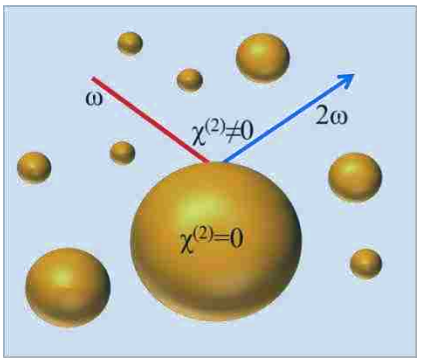

Figure 1.2. SHG generated on a nanoparticle surface.

1.3 Reflectivity of Metals

When metals are optically excited by a short femtosecond pulse, a non-Fermi distribution of conduction electrons is created.[24] These highly-thermalized nonequilibrium electrons can then diffuse their energy through ballistic electron transport, electron-electron collisions, electron-phonon scattering, and phonon-phonon scattering.[25,26] Within approximately 100 fs, ballistic electrons travel deeper into the bulk of the sample on the order of the optical penetration depth. Additionally, in this timescale the excited electrons can participate in collisions with other Fermi electrons creating electron thermalization.[27] The resulting electron gas can also transfer energy to the lattice through electron-phonon collisions which happen on the order of picoseconds. This exchange of energy can be described by the two-temperature model where the hot electron bath and cold lattice reach a local thermal equilibrium described by

$$C_e(T_e)\frac{\partial T_e}{\partial t} = \frac{\partial}{\partial z}\left(K_e\frac{\partial T_e}{\partial t}\right) - g(T_e - T_l) + P(z,t), \tag{1.4}$$

and

$$C_l\frac{\partial T_l}{\partial t} = g(T_e - T_l) \tag{1.5}$$

where C_e is the electron gas heat capacity, K_e is the electron thermal conductivity, g is the electron-phonon coupling constant, $(T_e - T_l)$ is the difference in electron and lattice temperatures, and $P(z,t)$ is a source term describing the intensity dependence of electron heating from the laser pulse at a depth of z .[24] In Eq. 1.5 the heat capacity of the lattice, C_l, only depends on the electron-phonon coupling constant and the temperature gradient of the electron bath and lattice. The last process describes the coupling of the lattice to itself through vibrational motion via phonon-phonon scattering, which happens on the timescale of hundreds of picoseconds to nanoseconds.[24] These concepts are of critical importance in describing laser-induced heating of metals.

1.4 Scope of Dissertation

This dissertation describes the use of ultrafast spectroscopy and nonlinear spectroscopy to investigate the excited-state dynamics and nonlinear optical properties of various nanomaterials. Chapter 2 describes research which uses transient absorption spectroscopy to study the excited-state dynamics of size-dependent colloidal TiO_2-Au nanocomposites. In this investigation, an enhanced size-dependent electron-transfer lifetime is observed for nanocomposites containing different molar ratios of TiO_2 to gold in the colloidal nanomaterials. In Chapter 3, the time-dependent nonlinear optical technique of *in-situ* SHG is used to monitor the seed-mediated growth of colloidal citrate-stabilized gold nanoparticles in water. The real-time monitoring of the growth dynamics show size-dependent nonlinear enhancements at early growth times which are attributed to plasmonic hot spots. In Chapter 4, the optical technique of ultrafast reflectivity is used to investigate excited-state carrier dynamics of the perovskite thin film $La_{0.67}Sr_{0.33}MnO_3/SrTiO_3$ prepared under oxygen deficient conditions. Here, the excited-

state dynamics are described by two relaxation lifetimes and two separate oscillatory phonon frequencies, which are used to characterize the perovskite thin film. Chapter 5 involves our work with the Consortium for Innovation in Manufacturing and Materials (CIMM) at LSU where we modify our ultrafast reflectivity setup to study heating and melting dynamics in different metals and metal alloys. Finally, Chapter 6 describes research using the electronic sum-frequency generation (ESFG) technique to study the azimuthal angular dependence in α-quartz (0001). Throughout my research I've used ultrafast and nonlinear spectroscopy to study both colloidal nanomaterials and metallic surfaces. Each individual experiment involves either modifications or new constructions of our experimental setups for the purpose of investigating the chemistry and materials science of interest under the specialized optical configurations to ascertain critical new insight of different nanomaterial interfaces.

1.5 References

(1) Zewail, A. H. Femtochemistry: Atomic-Scale Dynamics of the Chemical Bond Using Ultrafast Lasers (Nobel Lecture). *Angew. Chem. Int. Ed.* **2000**, *39*, 2586–2631.

(2) Michael Hollas, J. *Modern Spectroscopy*; John Wiley & Sons, 2004.

(3) Einstein, A. Zur Quantentheorie Der Strahlung. *Phys. Z.* **1917**, *18*, 121–128.

(4) Kafalas, P.; Masters, J. I.; Murray, E. M. E. Photosensitive Liquid Used as a Nondestructive Passive Q-Switch in a Ruby Laser. *J. Appl. Phys.* **1964**, *35*, 2349–2350.

(5) Shank, C. V.; Ippen, E. P. Subpicosecond Kilowatt Pulses from a Mode-locked Cw Dye Laser. *Appl. Phys. Lett.* **1974**, *24*, 373–375.

(6) Fork, R. L.; Brito Cruz, C. H.; Becker, P. C.; Shank, C. V. Compression of Optical Pulses to Six Femtoseconds by Using Cubic Phase Compensation. *Opt. Lett., OL* **1987**, *12*, 483–485.

(7) Zhou, J.; Taft, G.; Huang, C.-P.; Murnane, M. M.; Kapteyn, H. C.; Christov, I. P. Pulse Evolution in a Broad-Bandwidth Ti:sapphire Laser. *Opt. Lett., OL* **1994**, *19*, 1149–1151.

(8) Brabec, T.; Spielmann, C.; Curley, P. F.; Krausz, F. Kerr Lens Mode Locking. *Opt. Lett., OL* **1992**, *17*, 1292–1294.

(9) Zewail, A. H. Femtochemistry: Atomic-Scale Dynamics of the Chemical Bond. *J. Phys. Chem. A* **2000**, *104*, 5660–5694

(10) Dantus, M.; Gross, P. Ultrafast spectroscopy. *Encyclopedia of Applied Physics* **1998**, *22*, 431-456.

(11) Boyd, R. W. *Nonlinear Optics*; Elsevier, 2003.

(12) Haber, L. H.; Kwok, S. J. J.; Semeraro, M.; Eisenthal, K. B. Probing the Colloidal Gold Nanoparticle/aqueous Interface with Second Harmonic Generation. *Chem. Phys. Lett.* **2011**, *507*, 11–14.

(13) Wang, H.; Yan, E. C. Y.; Borguet, E.; Eisenthal, K. B. Second Harmonic Generation from the Surface of Centrosymmetric Particles in Bulk Solution. *Chem. Phys. Lett.* **1996**, *259*, 15–20.

(14) Eisenthal, K. Second Harmonic Spectroscopy of Aqueous Nano- and Microparticle Interfaces. *Chem. Rev.* **2006**, *106*, 1462−1477.

(15) Karam, T. E.; Haber, L. H. Molecular Adsorption and Resonance Coupling at the Colloidal Gold Nanoparticle Interface. *J. Phys. Chem. C* **2014**, *118*, 642–649.

(16) Kumal, R. R.; Karam, T. E.; Haber, L. H. Determination of the Surface Charge Density of Colloidal Gold Nanoparticles Using Second Harmonic Generation. *J. Phys. Chem. C* **2015**, *119*, 16200–16207.

(17) Liu, Y.; Dadap, J.; Zimdars, D.; Eisenthal, K. B. Study of Interfacial Charge-Transfer Complex on TiO2 Particles in Aqueous Suspension by Second-Harmonic Generation. J. Phys. Chem. B **1999**, 103, 2480−2486.

(18) Liu, J.; Subir, M.; Nguyen, K.; Eisenthal, K. B. Second Harmonic Studies of Ions Crossing Liposome Membranes in Real Time. J. Phys. Chem. B **2008**, 112, 15263−15266.

(19) Vance, F. W.; Lemon, B. J.; Hupp, J. T. Enormous HyperRayleigh Scattering from Nanocrystalline Gold Particle Suspensions. J. Phys. Chem. B **1998**, 102, 10091−10093.

(20) Haber, L. H.; Kwok, S. J. J.; Semeraro, M.; Eisenthal, K. B. Probing the Colloidal Gold Nanoparticle/Aqueous Interface with Second Harmonic Generation. Chem. Phys. Lett. **2011**, 507,11–14.

(21) Hao, E. C.; Schatz, G. C.; Johnson, R. C.; Hupp, J. T. HyperRayleigh scattering from silver nanoparticles. J. Chem. Phys. **2002**, 117, 5963−5966.

(22) Russier-Antoine, I.; Benichou, E.; Bachelier, G.; Jonin, C.; Brever, P. F. Multipolar Contributions of the Second Harmonic Generation from Silver and Gold Nanoparticles. J. Phys. Chem. C **2007**, 111, 9044−9048.

(23) Jin, R.; Jureller, J.; Kim, H.; Scherer, N. Correlating Second Harmonic Optical Responses of Single Ag Nanoparticles with Morphology. J. Am. Chem. Soc. **2005**, 127, 12482−12483.

(24) Bennemann, K. H. *Non-Linear Optics in Metals*; Clarendon Press, **1998**.

(25) Fann, W. S.; Storz, R.; Tom, H. W.; Bokor, J. Electron Thermalization in Gold. *Phys. Rev. B Condens. Matter* **1992**, *46*, 13592–13595.

(26) Farm, W. S.; Storz, R.; Tom, H. W. K.; Bokor, J. Direct Measurement of Nonequilibrium Electron-Energy Distributions in Sub-Picosecond Laser-Heated Gold Films. *Surf. Sci.* **1993**, *283*, 221–225.

(27) Sun, C.; Vallée, F.; Acioli, L. H.; Ippen, E. P.; Fujimoto, J. G. Femtosecond-Tunable Measurement of Electron Thermalization in Gold. *Phys. Rev. B Condens. Matter* **1994**, *50* (20), 15337–15348.

Chapter 2. Excited-State Dynamics of Size-Dependent Colloidal TiO_2-Au Nanocomposites

2.1 Introduction

Gold nanoparticles have been widely studied due to their various potential applications in sensing, photovoltaics, catalysis, imaging, and photothermal therapy.[1–10] The size- and shape-dependent localized surface plasmon resonances from coherent oscillations of free electrons[11–13] can lead to large optical field enhancements. Ultrafast pump-probe spectroscopy has been used to investigate the excited-state relaxation dynamics of gold nanoparticles, which can be characterized by different spectral regions that correspond to different relaxation processes.[14–17] A higher-energy, excited-state absorption spectral region near 480 nm is attributed to the interband excitation of electrons from the gold *d* band to the sp band above the Fermi level, with excited-state dynamics specified by the electronic interband transition lifetime. A lower-energy depletion spectrum near 550 nm corresponds to the plasmon resonance region with relaxation dynamics described by electron-phonon and phonon-phonon scattering lifetimes. The electron-phonon scattering lifetime is observed to increase as the pump pulse intensity is increased due to heating of the electron gas.[11,16–19] At even lower spectral energies, excited-state absorption centered near 600 nm is attributed to plasmon-induced hot carriers.[20–23] In general, the excited-state dynamics from the interband transition and electron-phonon scattering are independent of the size and shape of the gold nanoparticles for sizes ranging from approximately 10 nm to 60 nm.[17–19] The phonon-phonon scattering lifetimes, in contrast,

Reprinted from Karam, T. E.; Khoury, R. A.; Haber, L. H., *J. Chem. Phys.* 144 (12), 124704, 2016, with the permission of AIP Publishing and coauthors.

are shown to depend on the surface-to-volume ratio of the nanoparticle due to energy transfer to the surroundings.[19,24]

Semiconductor-metal nanocomposites are of great interest for plasmon-induced photocatalytic applications such as the production of hydrogen,[25–27] the reduction of thiocyanate,[28] and the oxidation of carbon monoxide.[29] The oxidation of CO to CO_2 at the surface of semiconductor-supported gold nanoclusters depends on the nanocluster size as well as the size and material of the semiconductor.[30,31] Several studies have reported ultrafast electron transfer into the conduction band of TiO_2 nanocrystals after an excitation on resonance with the plasmon band.[32–34] Excitation above the Fermi level permits excited electrons to cross the Schottky barrier leading to electron transfer from gold to TiO_2.[35] Excitation above the TiO_2 band gap in colloidal suspensions of gold nanoclusters adsorbed to TiO_2 nanoparticles in ethanol-toluene causes electron transfer from TiO_2 to gold for photocatalytic reduction reactions and size-dependent Fermi level shifts with larger shifts for smaller nanocluster sizes.[36,37] An opposite size-dependent trend is observed for gold-TiO_2 nanocomposites in water, where a more negative Fermi energy shift occurs for larger gold nanocluster sizes.[38] Understanding the relationship between the semiconductor-metal nanocomposite size and morphology with the resulting excited-state dynamics is critical for the development, control, and optimization of the nanomaterial catalytic properties.[39]

In this paper, we report investigations on the ultrafast excited-state dynamics of TiO_2-Au nanocomposites composed of size-dependent gold nanocluster shells surrounding a TiO_2 core in colloidal suspension in water. The electron-phonon and

phonon-phonon scattering lifetimes are found to be constant for the different nanocluster shell sizes. The decay of the induced excitation band centered at 480 nm is characterized by two lifetimes corresponding to excited-state electrons from the gold interband transition and size-dependent electron transfer between the gold nanocluster shell and the TiO_2 core. In addition, size-dependent periodic oscillations are observed at the plasmon depletion band and are attributed to coherent acoustic phonons of the gold nanocluster shell.

2.2. Synthesis of TiO_2-Au Nanocomposites

The TiO_2-Au nanocomposites are prepared by hydrolysis of titanium (IV) tetraisopropoxide ($Ti[OCH(CH_3)_2]_4$) (TTIP) followed by the reduction of gold chloride ($HAuCl_4$) at the TiO_2 nanoparticle surface.[39] All chemicals are purchased from Sigma-Aldrich and are used without further purification in ultrapure water. Briefly, the TiO_2 colloidal suspension is produced by acidifying 200 ml of water with perchloric acid ($HClO_4$) to a final pH of 1.5 under vigorous stirring followed by the dropwise addition of 3.0 ml of 0.35M TTIP in ethanol (EtOH). The reaction flask is then covered with parafilm and stirred vigorously for 20 min. Three different suspensions of gold-capped TiO_2 nanocomposites are prepared by adding 4 ml of the TiO_2 colloid suspension to 0.7 ml, 1.4 ml, and 2.0 ml, respectively, of 30 mM gold chloride solution, with the total volume of the solution subsequently adjusted to 100 ml by adding ultrapure water. The relative concentrations of $HAuCl_4$ are varied in these solutions to achieve molar concentration ratios of $[TiO_2]$:[Au] of 1:1, 1:2, and 1:3, respectively. Finally, 5 ml of a 1 mM solution of the reducing agent, sodium borohydride ($NaBH_4$) in water, is added

dropwise under vigorous stirring over approximately 20 min to each solution until a deep red color change is observed.

2.3 TiO_2-Au Characterization

Transmission electron microscopy (TEM) images and the corresponding extinction spectra of the different TiO_2-Au nanocomposite samples are shown in Figure 2.1. The size distributions of the nanoparticles are obtained after surveying more than 100 nanoparticles for each sample. Additional TEM images of the nanoparticles are shown in Appendix A.[55] All nanoparticles and nanocomposites are observed to be very spherical in shape. The average diameter of the TiO_2 nanoparticles is measured to be 9.9 ± 0.4 nm. The average diameters of the 1:1, 1:2, and 1:3 [TiO_2]:[Au] nanocomposites are measured to be 19.1 ± 0.4 nm, 21.9 ± 0.3 nm, and 24.3 ± 0.4 nm, respectively. Although the spatial resolution of the electron microscopy used in this study is insufficient to clearly resolve the size distribution and morphology of individual gold nanoclusters on the TiO_2 nanoparticle surface, the average gold nanocluster shell thickness can be estimated from the increases of the nanoparticle sizes by the TEM measurements, following previous comparative investigations.[39] Using this approach, the thickness of the gold nanocluster shell is estimated to be 4.6 ± 0.3 nm, 6.0 ± 0.3 nm, and 7.2 ± 0.3 nm for the 1:1, 1:2, and 1:3 [Au]:[TiO_2] nanocomposite samples, respectively.

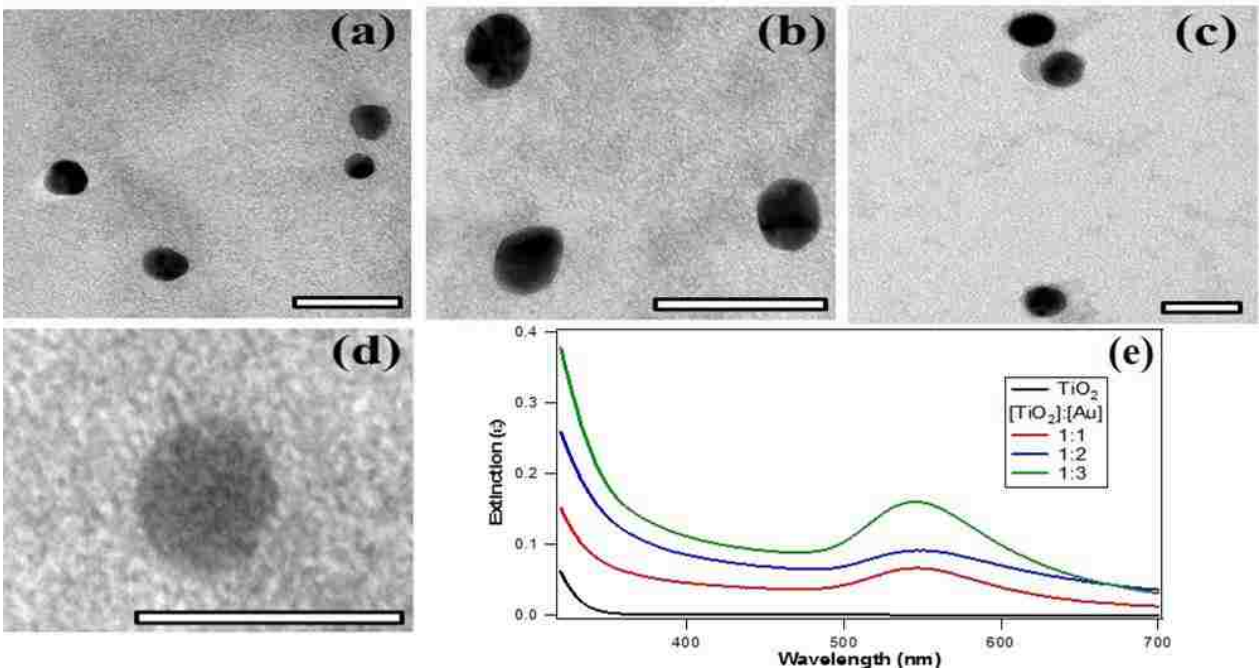

Figure 2.1. Transmission electron microscopy of (a) 1:1, (b) 1:2, (c) 1:3 TiO_2-Au nanocomposites and (d) precursor TiO_2 nanoparticles. The scale bars correspond to 40 nm. (e) Extinction spectra of colloidal TiO_2 nanoparticles (black) and TiO_2-Au nanocomposites with 1:1 (red), 1:2 (blue), and 1:3 (green) [TiO_2]:[Au] ratios, respectively.

2.4 Transient Absorption Setup

The transient absorption setup consists of an amplified titanium:sapphire laser system, an optical parametric amplifier (OPA), an optical setup, and a fiber optic spectrometer with a charge-coupled device detector (Figure 2.2).[18,40] The laser produces 0.7 mJ, 75 fs pulses centered at 800 nm with a repetition rate of 10 kHz. A 90/10 beam splitter is used to separate the pump and probe beams. The pump beam is passed through an OPA to generate 400 nm, 5 μJ pump pulses. The probe beam is focused into a fused quartz flow cell containing water to generate the femtosecond white light probe pulses that are refocused to a spatial overlap with the pump pulse at the sample, which is contained in a 3 mm fused quartz cell under constant stirring. The pump-probe temporal delay is controlled using a retroreflector on a computer-controlled

translation stage. A computer-controlled beam block opens and shuts on the pump pulse in synchronization with an automated file saving program, and 60 spectra at 1 s acquisitions are taken for each time step. Several time-resolved transient absorption spectral scans are taken for each sample for statistical analysis.

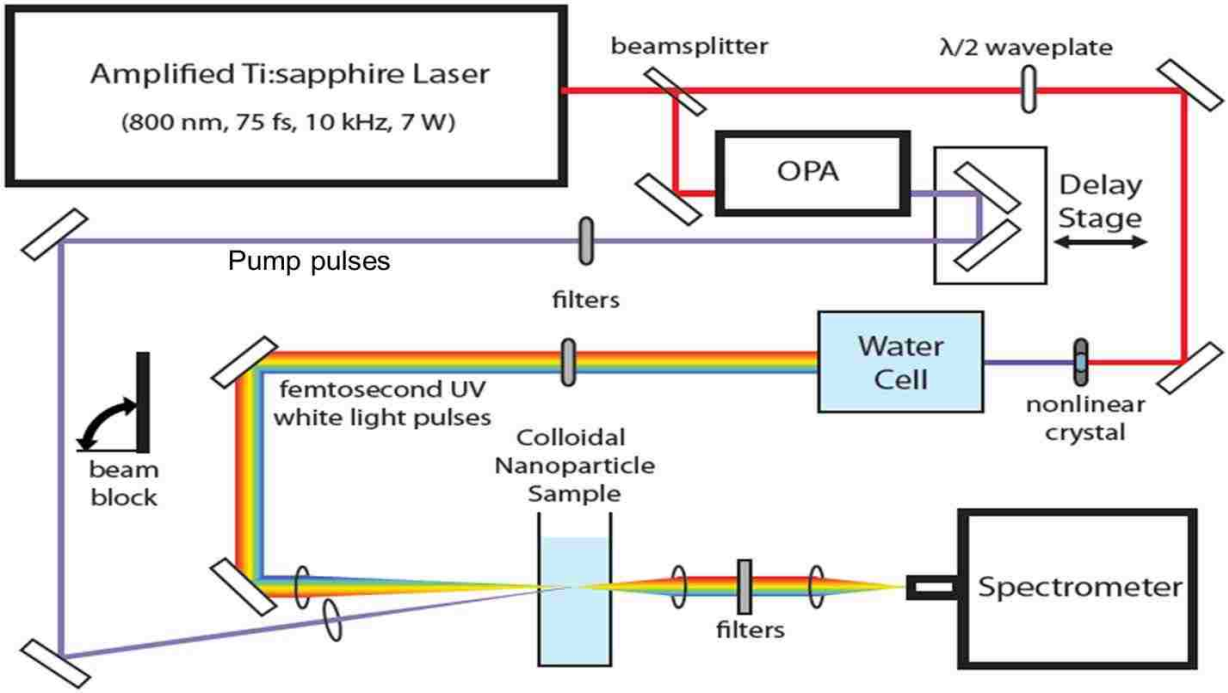

Figure 2.2. Transient absorption optical setup.

2.5 Results and Discussion

Pump-probe transient absorption spectroscopy is used to investigate the excited-state dynamics of the colloidal TiO_2-Au nanocomposites. Figure 2.3 shows the transient absorption spectra of the colloidal samples at different pump-probe time delays using 400 nm excitation pulses for the (a) 1:1, (b) 1:2, and (c) 1:3 [TiO_2]:[Au] ratios, respectively. As in the case of free colloidal gold nanoparticles, the transient absorption spectra are described by a positive excited-state absorption band centered near 480 nm followed by a negative depletion band centered near 550 nm.[14,15] The positive band centered near 480 nm is consistent with the well-established

interband transition region in the gold nanoclusters. The negative depletion band centered near 550 nm is consistent with the depletion of plasmon electrons.[14,15] By careful analysis of the transient absorption data, information on the optical and electronic interactions between the gold nanoclusters and the TiO_2 nanoparticle surface can be obtained.

Figure 2.4 shows the time-dependent transient absorption profiles of the colloidalTiO_2-Au nanocomposites with (a) 1:1, (b) 1:2, and (c) 1:3 [TiO_2]:[Au] ratios, respectively, at probe wavelengths of 480 nm (blue data points) and 550 nm (red data points). The time-dependent transient absorption profiles measured at 550 nm are fit with a biexponential function to determine the excited-state lifetimes due to electron-phonon scattering and phonon-phonon scattering.[14,15]

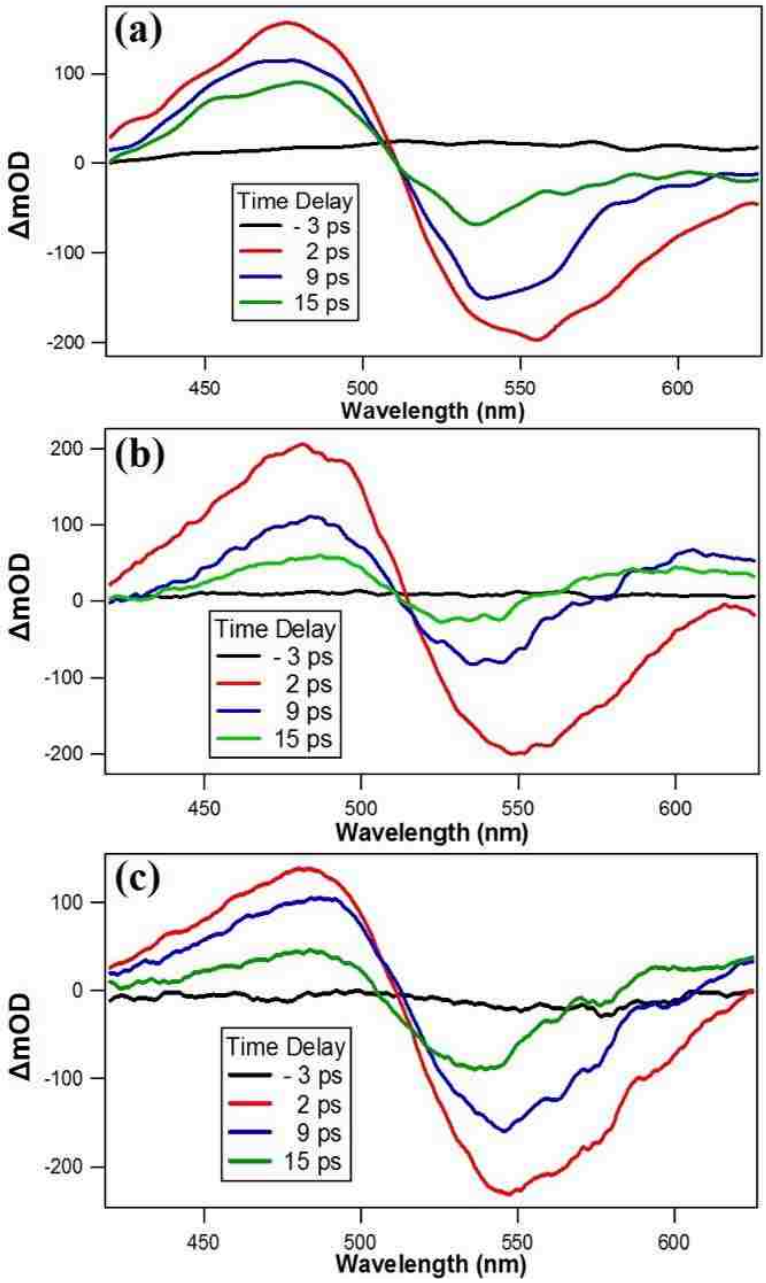

Figure 2.3. Transient absorption spectra of colloidal TiO_2-Au nanocomposites at different time delays after 400 nm excitation pulses with (a) 1:1, (b) 1:2, and (c) 1:3 [TiO_2]:[Au] ratios, respectively.

The electron-phonon scattering lifetimes are 3.0 ± 0.3 ps, 3.3 ± 0.5 ps, and 3.2 ± 0.2 ps for the 1:1, 1:2, and 1:3 [TiO_2]:[Au] ratios, respectively. The phonon-phonon scattering lifetimes are 49 ± 6 ps, 53 ± 8 ps, and 55 ± 8 ps for the 1:1, 1:2, and 1:3 [TiO_2]:[Au] ratios, respectively. Our previous studies of colloidal 54 nm gold

nanospheres using the same experimental setup obtained electron-phonon and phonon-phonon scattering lifetimes of approximately 3 ps and 100 ps, respectively.[18] The electron-phonon scattering lifetimes from the TiO_2-Au nanocomposites correspond with previous measurements of colloidal gold nanoparticles. Additionally, the electron-phonon scattering lifetimes are similar for the three samples to within experimental uncertainty. These results agree with previous work that showed the electron-phonon scattering lifetime is generally independent of the size and shape for gold nanoparticles of sizes larger than about 10 nm,[17,19,41,42] which suggests that the gold nanocluster shells in the TiO_2-Au nanocomposites are large enough so that confinement effects can be neglected.[19,43,44] However, the phonon-phonon scattering lifetimes from the TiO_2-Au nanocomposites are considerably faster than the corresponding lifetime in gold nanoparticles, and these lifetimes remain the same to within the experimental uncertainty for the three colloidal TiO_2-Au nanocomposite samples. The phonon-phonon scattering lifetime is known to depend on the surrounding medium of the gold nanoclusters caused by differences in the rate of energy transfer.[45,24] The faster phonon-phonon scattering lifetimes of TiO_2-Au nanocomposites compared to gold nanoparticles can be explained due to the much higher thermal conductivity of TiO_2 compared to water, leading to faster heat transfer. However, the complicated structure of the porous, inhomogeneous gold nanocluster shell surrounding the TiO_2 core requires additional characterizations in order to determine the total gold surface area in contact with water and TiO_2 for a better understanding of the effect of energy transfer on the phonon-

phonon scattering lifetimes. The size-dependent superimposed oscillations are due to acoustic phonons and will be discussed later.

The transient absorption time profiles measured at 480 nm are fit with biexponential functions with corresponding lifetimes attributed to the excited-state decay of electrons in the gold interband transition with an additional lifetime attributed to electron transfer between the gold nanoclusters and the TiO_2 conduction band. The lifetimes associated with the interband transition in gold are measured to be 7.9 ± 0.3 ps, 8.2 ± 0.2 ps, and 8.5 ± 0.3 ps for the 1:1, 1:2, and 1:3 [TiO_2]:[Au] ratios, respectively. These lifetimes are the same to within the experimental uncertainty.

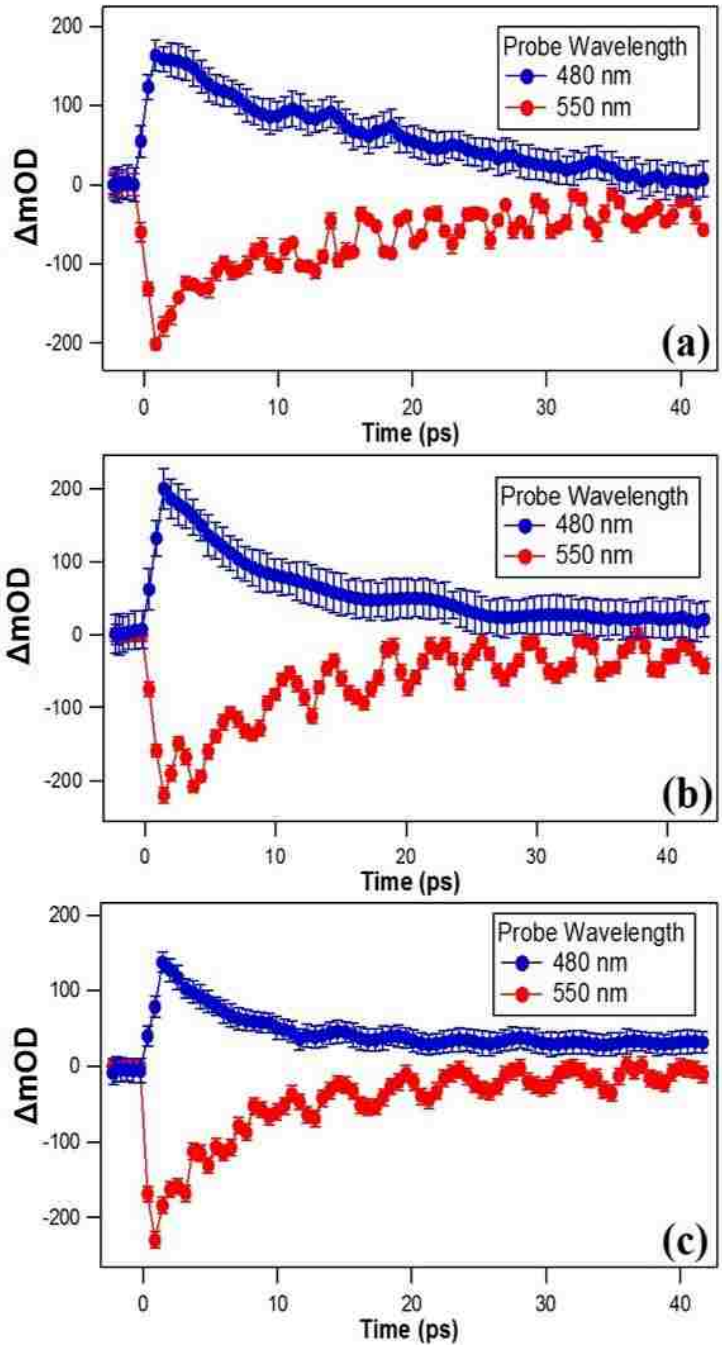

Figure 2.4. Transient absorption time profiles of colloidal TiO_2-Au nanocomposites at 480 nm and 550 nm with (a) 1:1, (b) 1:2, and (c) 1:3 [TiO_2]:[Au] ratios, respectively.

The lifetimes associated with the electron transfer between the gold and TiO_2 nanomaterials are determined to be 33.1 ± 0.4 ps, 7.5 ± 0.1 ps, and 4.2 ± 0.1 ps for the 1:1, 1:2, and 1:3 [TiO_2]:[Au] ratios, respectively. These lifetimes become faster as the gold nanocluster shell size increases. The net electron transfer from the gold to the

TiO_2 conduction band at the metal-semiconductor junction occurs upon photoexcitation at time zero on the time scale of the electron-electron scattering, which occurs faster than the current experimental temporal resolution. As the pump-probe time increases, back electron transfer from the TiO_2 to the gold nanocluster shell occurs, corresponding to an eventual relaxation back to the global ground state. Larger gold nanoclusters have a larger density of states near the Fermi level leading to a faster electron-hole recombination rate and a shorter electron transferlifetime.[46]

Figure 2.5 shows the decay spectra obtained using the global analysis technique[47,48] for a more detailed analysis of the transient absorption spectroscopy of the colloidal (a) 1:1, (b) 1:2, and (c) 1:3 [TiO_2]:[Au] nanocomposites, respectively. The transient absorption time-profiles are fit using four exponential functions and an offset, given by:

$$I(t) = y_0 + A_{ib}e^{\frac{-t}{\tau_{ib}}} + A_{et}e^{\frac{-t}{\tau_{et}}} + A_{ep}e^{\frac{-t}{\tau_{ep}}} + A_{pp}e^{\frac{-t}{\tau_{pp}}} \quad (2.1)$$

where $I(t)$ is the time-dependent transient absorption intensity at a given wavelength, y_0 is a constant offset, and A_{ib}, A_{et}, A_{ep}, and A_{pp} are the wavelength-dependent amplitudes of the excited-state decays of the interband transition, the electron-transfer, the electron-phonon scattering, and phonon-phonon scattering, respectively, with the corresponding lifetimes,τ_{ib}, τ_{et}, τ_{ep}, and τ_{pp} that describe these dynamics. The decay spectra in Figure 2.5 show the wavelength-dependent amplitudes of the four dynamic processes for the different nanocomposite samples. The electron-phonon scattering lifetimes obtained from the global analysis fits for the 1:1, 1:2, and 1:3 [TiO_2]:[Au] nanocomposites are 3.0 ± 0.3 ps, 3.3 ± 0.5 ps, and 3.2 ± 0.2 ps, respectively. Additionally, the obtained phonon-phonon scattering lifetimes are 49 ± 6 ps, 53 ± 8 ps,

and 55 ± 8 ps, for the 1:1, 1:2, and 1:3 [TiO_2]:[Au] nanocomposites, respectively. The obtained interband transition lifetimes are 7.9 ± 0.3 ps, 8.2 ± 0.2 ps, and 8.5 ± 0.3 ps, for the 1:1, 1:2, and 1:3 [TiO_2]:[Au] nanocomposites, respectively. The obtained electron transfer lifetimes are 33.1 ± 0.4 ps, 7.5 ± 0.1 ps, and 4.2 ± 0.1 ps, for the 1:1, 1:2, and 1:3 [TiO_2]:[Au] nanocomposites, respectively. These values are all in agreement with the results from the transient absorption time profiles.

The global analysis decay spectra associated with each dynamic process provide important spectral characterizations of the TiO_2-Au nanomaterial. The interband transition decay spectrum is centered near 480 nm, followed by the electron transfer decay spectrum centered near 485 nm. These decay spectra approach zero amplitude, to within the experimental uncertainty, for wavelengths greater than 520 nm. The electron-phonon scattering and phonon-phonon scattering decay spectra are both centered near 550 nm. The amplitudes of these electron-phonon and phonon-phonon decay spectra approach zero to within experimental uncertainty at wavelengths below 500 nm. This separation in the decay spectra allows the 480 nm and 550 nm time profiles to be accurately treated using separate biexponential fits with different lifetimes.

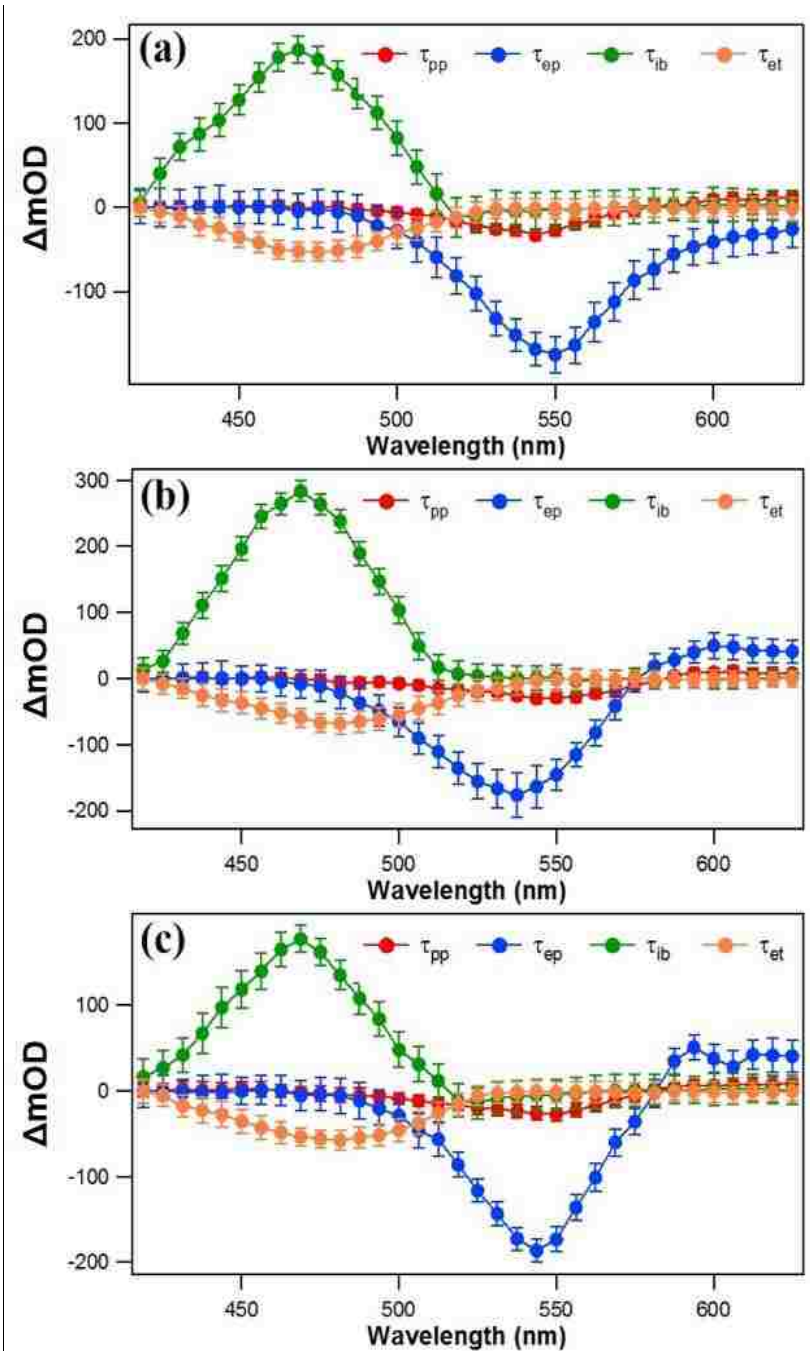

Figure 2.5. Decay spectra obtained using a sum of exponential fits for global analysis of the transient absorption results from (a) 1:1, (b) 1:2, and (c) 1:3 [TiO_2]:[Au] nanocomposites, respectively.

The interband transition decay spectra obtained from global analysis are positive in amplitude while the electron transfer decay spectra are negative. This indicates that the electron transfer causes a net depletion from the electronic population of

the *sp* band associated with the interband transition. A positive excited-state absorption band at wavelengths longer than 600 nm, attributed to thermally excited plasmon electron distributions, is observed for the 1:2 and 1:3 samples. However, this positive band is not observed for the 1:1 sample. This agrees with previous measurements that observe more prominent hot electron excited-state absorption in this spectral region for larger nanoparticle sizes.[15]

Figure 2.6 shows the time-dependent differences between the experimental results and the biexponential best fits for the TiO_2-Au nanocomposites with (a) 1:1, (b) 1:2, and (c) 1:3 [TiO_2]:[Au] ratios measured at 550 nm. The resulting oscillations are attributed to acoustic phonons of the plasmonic gold nanocluster shell surrounding the TiO_2 core due to the characteristic spectroscopy, frequencies, and damping times.[49–52] The residual oscillations of the phonons are fit using a sine function given by:

$$I(t) = y_0 + Ae^{\frac{-t}{\tau_d}}\sin(2\pi ft + \varphi) \tag{2.2}$$

where $f, \varphi,$ and τ_d are the frequency, phase shift, and phonon damping time, respectively. The phonon frequencies obtained from the fits are 0.35 ± 0.02 ps^{-1}, 0.26 ± 0.02 ps^{-1}, and 0.22 ± 0.01 ps^{-1} for the 1:1, 1:2, and 1:3 samples, respectively. The corresponding phonon damping times are 108 ± 7 ps, 106 ± 8 ps, and 110 ± 7 ps for the 1:1, 1:2, and 1:3 samples, respectively. The size-dependent acoustic phonon frequencies are consistent with an inhomogeneous, porous gold shell composed of aggregated nanoclusters.[53] Figure 2.7 shows the trend in experimental size-dependent phonon frequencies. Additional discussion on the phonon frequencies compared to different nanocomposite architectures is discussed in Appendix A.[55] More

work is still needed to accurately characterize the gold nanocluster shell surrounding the TiO_2 core, including size distribution measurements of the nanoclusters and pores.

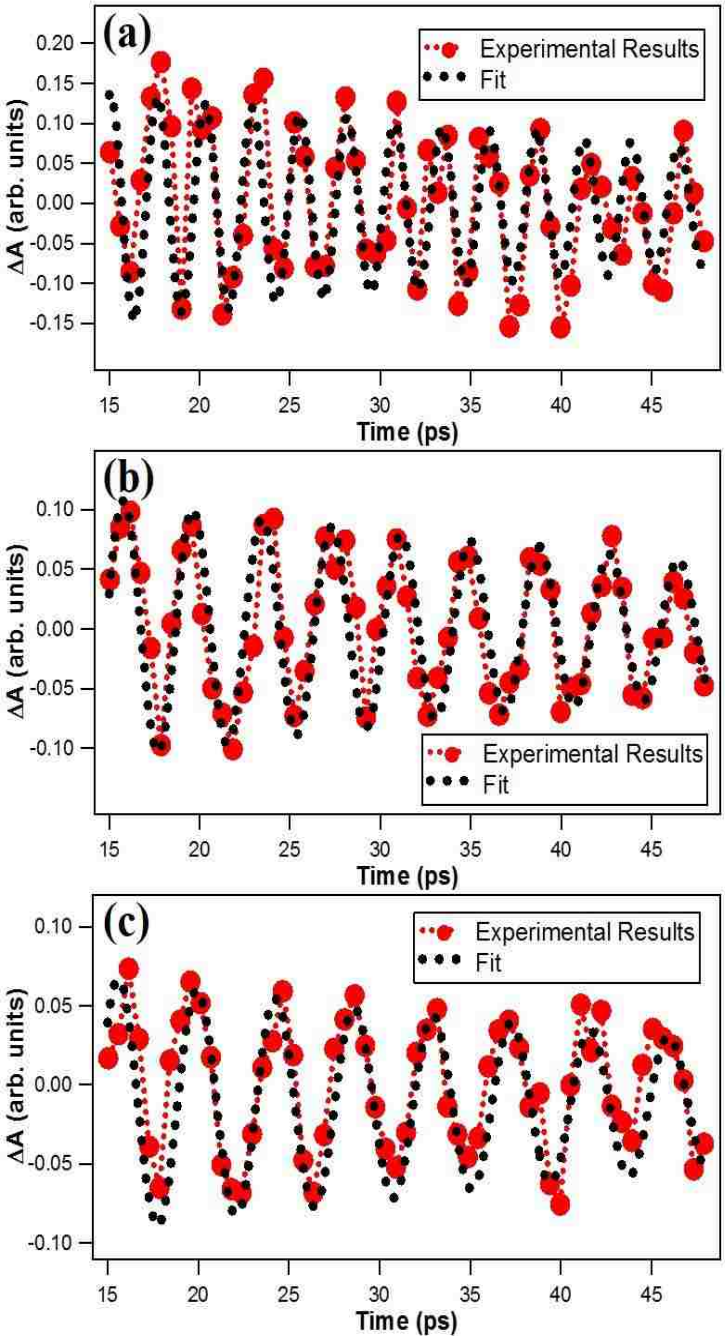

Figure 2.6. Residual signals from the transient absorption time profiles integrated at 550 nm after subtracting the biexponential best fits, showing the phonon oscillations for the different TiO_2-Au nanocomposites samples with (a) 1:1, (b) 1:2, and (c) 1:3 [TiO_2]:[Au] ratio, respectively, along with the corresponding fits.

The acoustic phonon damping times are known to depend on factors such as energy transfer to the surrounding environment, acoustic phonon coupling to other phonon modes in the nanoparticle, and dephasing of the phonon frequencies due to polydispersity of the sample.[50] When the damping is dominated by either polydispersity dephasing or energy transfer to a homogeneous surrounding medium, the damping time τ_d is expected to be proportional to the nanoparticle radius.[50,54] However, these descriptions apply to isolated nanoparticles and do not account for the porous nanocluster shell architecture in the TiO_2-Au nanocomposites studied here. The phonon damping times of the gold nanocluster shells surrounding the TiO_2 nanoparticles are measured to be constant for the different nanocomposite sizes, to within experimental uncertainty. Since the gold nanoclusters have surface contact with both TiO_2 and water, and form aggregated contact with neighboring nanoclusters in an extended porous shell architecture, the effect of a heterogeneous surrounding will likely result in deviations from an ideal model. Transient absorption spectroscopy provides key information on the complicated spectroscopic and dynamic processes, including plasmon depletion, interband transitions, electron transfer, and acoustic phonon oscillations, occurring in these colloidal TiO_2-Au nanocomposites.

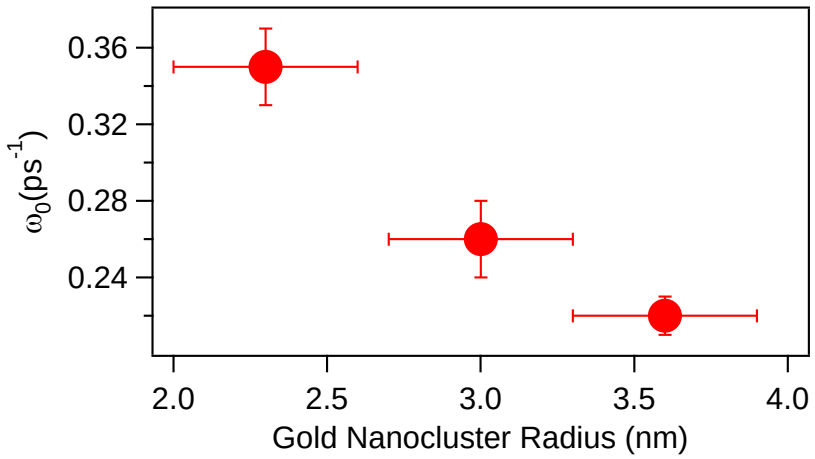

Figure 2.7. Size-dependent frequencies of the phonon oscillations of gold nanoclusters at the surface of colloidal TiO_2 nanoparticles.

2.6 Conclusion

The ultrafast excited-state dynamics of colloidal size-dependent TiO_2-Au nanocomposites in water are investigated using transient absorption spectroscopy. The average sizes of the gold nanocluster shells are determined using transmission electron microscopy for different molar concentration ratios of TiO_2 to Au. The transient absorption time profiles measured at the peak of the plasmon depletion band are fit to biexponential functions to obtain the lifetimes of the electron-phonon and phonon-phonon scattering processes, where the plasmon depletion dynamics are shown to be independent of the size of the gold nanocluster shells surrounding the TiO_2 nanoparticle core. The relaxation dynamics of the excited-state absorption band centered at 480 nm are fit with different biexponential functions to determine the lifetimes associated with the electronic interband transition in gold and the electron transfer between the gold and TiO_2 nanomaterials. While the interband transition lifetime is observed to remain constant under changing nanocluster shell sizes, the electron transfer lifetimes were shown to decrease significantly as the gold nanocluster shell size increases due to increased density of states near the

Fermi level. Additionally, size-dependent oscillations in the plasmon depletion transient absorption time profiles were observed and are attributed to acoustic phonon breathing modes of the gold nanocluster shells with frequencies that decrease and damping times that remain constant as the nanocluster shell sizes increase. These findings provide important information that can be useful for improving catalytic efficiencies in plasmonic TiO_2-Au nanocomposites.

2.7 References

(1) El-Sayed, I. H.; Huang, X.; El-Sayed, M. A. Surface Plasmon Resonance Scattering and Absorption of Anti-EGFR Antibody Conjugated Gold Nanoparticles in Cancer Diagnostics: Applications in Oral Cancer. *Nano Lett.* **2005**, *5*, 829–834.

(2) El-Sayed, I. H.; Huang, X.; El-Sayed, M. A. Selective Laser Photo-Thermal Therapy of Epithelial Carcinoma Using Anti-EGFR Antibody Conjugated Gold Nanoparticles. *Cancer Lett.* **2006**, *239*,129–135.

(3) Kamat, P. V. Photophysical, Photochemical and Photocatalytic Aspects of Metal Nanoparticles. *J.Phys. Chem. B* **2002**, *106*, 7729–7744.

(4) Narayanan r.; El-Sayed, M. A. Catalysis with Transition Metal Nanoparticles in Colloidal Solution: Nanoparticle Shape Dependence and Stability. *J. Phys. Chem. B* **2005**, *109*, 12663–12676.

(5) Haes, A. J.; Van Duyne, R. P. A. A Nanoscale Optical Biosensor: Sensitivity and Selectivity of an Approach Based on the Localized Surface Plasmon Resonance Spectroscopy of Triangular Silver Nanoparticles. *J. Am. Chem. Soc.* **2002**, *124*, 10596–10604.

(6) Sperling, R. A.; Gil, P. R.; Zhang, F.; Zanella, M.; Parak, W. J. Biological Applications of Gold Nanoparticles. *Chem. Soc. Rev.* **2008**, *37*, 1896–1908.

(7) Karam, T. E.; Haber, L. H. Molecular Adsorption and Resonance Coupling at the Colloidal Gold Nanoparticle Interface. *J. Phys. Chem. C* **2014**, *118*, 642–649.

(8) Prigodich, A. E.; Lee, O. –S.; Daniel, W. L.; Seferos, D. S.; G. C. Schatz, G. C.; Mirkin, C. A. Tailoring DNA Structure To Increase Target Hybridization Kinetics on Surfaces. *J. Am. Chem. Soc.* **2010**, *132*, 10638–10641.

(9) Kamat, P. V. Meeting the Clean Energy Demand: Nanostructure Architectures for Solar Energy Conversion. *J. Phys. Chem. C* **2007**, *111*, 2834–2860.

(10) Kholmicheva, N.; Moroz, P.; Rijal, U.; Bastola, E.; Uprety, P.; Liyanage, G.; Razgoniaev, A.; Ostrowski, A. D.; Zamkov, M. Plasmonic Nanocrystal Solar Cells Utilizing Strongly Confined Radiation. *ACS Nano* **2014**, *8*, 12549–12559.

(11) Link, S.; El-Sayed, M. A. Shape and Size Dependence of Radiative, Non-Radiative and Photothermal Properties of Gold Nanocrystals. *Int. Rev. Phys. Chem.* **2000**, *19*, 409–453. 88.

(12) Daniel, M. –C.; Astruc, D. Gold Nanoparticles: Assembly, Supramolecular Chemistry, Quantum-Size-Related Properties, and Applications toward Biology, Catalysis, and Nanotechnology. *Chem. Rev.* **2004**, *104*, 293–346.

(13) Chandra, M.; Dowgiallo, A. M.; Knappenberger, K. L. Controlled Plasmon Resonance Properties of Hollow Gold Nanosphere Aggregates. *J. Am. Chem. Soc.* **2010**, *132*, 15782–15789.

(14) Ahmadi, T.S.; Logunov, S.L.; El-Sayed, M.A.; Picosecond Dynamics of Colloidal Gold Nanoparticles. *J. Phys. Chem.* **1996**, *100*, 8053–8056.

(15) Logunov, S. L.; Ahmadi, T. S.; El-Sayed, M. A.; Khoury, J. T.; Whetten, R. L.; Electron Dynamics of Passivated Gold Nanocrystals Probed by Subpicosecond Transient Absorption Spectroscopy. *J. Phys. Chem. B* **1997**, *101*, 3713–3719.

(16) Hodak, J. H.; Martini, I.; Hartland, G. V. Spectroscopy and Dynamics of Nanometer-Sized Noble Metal Particles. *J. Phys. Chem. B* **1998**, *102*, 6958–6967.

(17) Link, S.; Burda, C.; Mohamed, M. B.; Nikoobakht, B.; El-Sayed, M.A. Femtosecond Transient-Absorption Dynamics of Colloidal Gold Nanorods: Shape Independence of the Electron-Phonon Relaxation Time. *Phys. Rev. B* **2000**, *61*, 6086.

(18) Karam, T. E.; Smith, H. T.; Haber, L. H. Enhanced Photothermal Effects and Excited-State Dynamics of Plasmonic Size-Controlled Gold–Silver–Gold Core–Shell–Shell Nanoparticles. *J. Phys. Chem. C* **2015**, *119*, 18573–18580.

(19) Hartland, G. V. Optical Studies of Dynamics in Noble Metal Nanostructures. *Chem. Rev.* **2011**, *111*, 3858–3887.

(20) Dulkeith, E.; Niedereichholz, T.; Klar, T. A.; Feldmann, J.; Von Plessen, G.; Gittins, D. I.; Mayya, K. S.; Caruso, F. Plasmon Emission in Photoexcited Gold Nanoparticles. *Phys. Rev. B* **2004**, *70*, 205424.

(21) Zhang, H.; Govorov, A. O. Optical Generation of Hot Plasmonic Carriers in Metal Nanocrystals: The Effects of Shape and Field Enhancement. *J. Phys. Chem. C* **2014**, *118*, 7606–7614.

(22) Govorov, A. O.; Zhang, H.; Gun'ko, Y. K. Theory of Photoinjection of Hot Plasmonic Carriers from Metal Nanostructures into Semiconductors and Surface Molecules. *J. Phys. Chem. C* **2013**, *117*, 16616–16631.

(23) Manjavacas, A.; Liu, J. G.; Kulkarni, V.; Nordlander, P. Plasmon-Induced Hot Carriers in Metallic Nanoparticles. *ACS Nano***2014**, *8*, 7630–7638.

(24) Dowgiallo, A. M.; Knappenberger, K. L. Influence of Confined Fluids on Nanoparticle-to-Surroundings Energy Transfer. *J. Am. Chem. Soc.* **2011**, *134*, 19393–19400.

(25) Murdoch, M.; Waterhouse, G. I. N.; Nadeem, M. A.; Metson, J. B.; Keane, M. A.; Howe, R. F.; Llorca, J.; Idriss, H. The Effect of Gold Loading and Particle Size on Photocatalytic Hydrogen Production from Ethanol over Au/TiO2 Nanoparticles. *Nat. Chem.* **2011**, *3*, 489–492.

(26) Maeda, K.; Domen, K. Photocatalytic Water Splitting: Recent Progress and Future Challenges. *J. Phys. Chem. Lett.* **2010**, *1*, 2655–2661.

(27) Joshi, U. A.; Palasyuk, A.; Arney, D.; Maggard, P. A. Semiconducting Oxides to Facilitate the Conversion of Solar Energy to Chemical Fuels. *J. Phys. Chem. Lett.* **2010**, *1*, 2719–2726.

(28) Kamat, P. V.; Flumiani, M.; Dawson, A. Metal–Metal and Metal–Semiconductor Composite Nanoclusters. *Colloids Surf. A Physicochem. Eng. Asp.* **2002**, *202*, 269–279.

(29) Chen, M.; Goodman, D. W. Catalytically Active Gold on Ordered Titania Supports. *Chem. Soc. Rev.* **2008**, *37*, 1860–1870.

(30) Meier, D. C.; Goodman, D. W. The Influence of Metal Cluster Size on Adsorption Energies: CO Adsorbed on Au Clusters Supported on TiO2. *J. Am. Chem. Soc.* **2004**, *126*, 1892–1899.

(31) Comotti, M.; Li, W. C.; Spliethoff, B.; Schüth, F. Support Effect in High Activity Gold Catalysts for CO Oxidation. *J. Am. Chem. Soc.* **2006**, *128*, 917–924. 89.

(32) Furube, A.; Du, L.; Hara, K.; Katoh, R.; Tachiya, M. Ultrafast Plasmon-Induced Electron Transfer from Gold Nanodots into TiO2 Nanoparticles. *J. Am. Chem. Soc.* **2007**, *129*, 14852–14853.

(33) Tian, Y.; Tatsuma, T. Mechanisms and Applications of Plasmon-Induced Charge Separation at TiO2 Films Loaded with Gold Nanoparticles. *J. Am. Chem. Soc.* **2005**, *127*, 7632–7637.

(34) Du, L.; Furube, A.; Yamamoto, K.; Hara, K.; Katoh, R.; Tachiya, M. Plasmon-Induced Charge Separation and Recombination Dynamics in Gold− TiO2 Nanoparticle Systems: Dependence on TiO_2 Particle Size. *J. Phys. Chem. C* **2009**, *113*, 6454–6462.

(35) McFarland, E. W.; Tang, J. A Photovoltaic Device Structure Based on Internal Electron Emission. *Nat.* **2003**, *421*, 616–618.

(36) Jakob, M.; Levanon, H.; Kamat, P. V. Charge Distribution between UV-Irradiated TiO2 and Gold Nanoparticles: Determination of Shift in the Fermi Level. *Nano Lett.* **2003**, *3*, 353–358.

(37) Subramanian, V.; Wolf, E. E.; Kamat, P. V. Catalysis with TiO2/Gold Nanocomposites. Effect of Metal Particle Size on the Fermi Level Equilibration. *J. Am. Chem. Soc.* **2004**, *126*, 4943–4950.

(38) Kiyonaga, T.; Fujii, M.; Akita, T.; Kobayashi, H.; Tada, H. Size-Dependence of Fermi Energy of Gold Nanoparticles Loaded on Titanium (IV) Dioxide at Photostationary State. *Phys. Chem. Chem. Phys.* **2008**, *10*, 6553–6561.

(39) Dawson, A.; and Kamat, P. V. Semiconductor-Metal Nanocomposites. Photoinduced Fusion and Photocatalysis of Gold-Capped TiO2 (TiO2/gold) Nanoparticles. *J. Phys. Chem. 2001* **B**, *105*, 960–966.

(40) Karam, T. E.; Siraj, N.; Warner, I. M.; Haber, L. H. Anomalous Size-Dependent Excited-State Relaxation Dynamics of NanoGUMBOS. *J. Phys. Chem. C* **2015**, *119*, 28206–28213.

(41) Hodak, J.; Martini, I.; Hartland, G. V. Ultrafast Study of Electron–Phonon Coupling in Colloidal Gold Particles. *Chem. Phys. Lett.* **1998**, *284*, 135–141.

(42) Link, S.; Burda, C.; Wang, Z. L.; El-Sayed, M. A. Electron Dynamics in Gold and Gold–Silver Alloy Nanoparticles: The Influence of a Nonequilibrium Electron Distribution and the Size Dependence of the Electron–Phonon Relaxation. *J. Chem. Phys.* **1999**, *111*, 1255–1264.

(43) Arbouet, A.; Voisin, C.; Christofilos, D.; Langot, P.; Fatti, N. D.; Vallée, F.; Lermé, J.; Celep, G.; Cottancin, E.; Gaudry, M.; et al. Electron-Phonon Scattering in Metal Clusters. *Phys. Rev. Lett.* **2003**, *90* (17), 177401.

(44) Knappenberger, K. L., Jr; Schwartzberg, A. M.; Dowgiallo, A.-M.; Lowman, C. A. Electronic Relaxation Dynamics in Isolated and Aggregated Hollow Gold Nanospheres. *J. Am. Chem. Soc.* **2009**, *131*, 13892–13893.

(45) Mohamed, M. B.; Ahmadi, T. S.; Link, S.; Braun, M.; El-Sayed, M.A. Hot Electron and Phonon Dynamics of Gold Nanoparticles Embedded in a Gel Matrix. *Chem. Phys. Lett.* **2001**, *343*, 55–63.

(46) Anger, P.; Bharadwaj, P.; Novotny, L. Enhancement and Quenching of Single-Molecule Fluorescence. *Phys. Rev. Lett.* **2006**, *96*, 113002.

(47) Banerji, N.; Cowan, S.; Leclerc, M.; Vauthey, E.; Heeger, A. J. Exciton Formation, Relaxation, and Decay in PCDTBT. *J. Am. Chem. Soc.* **2010**, *132*, 17459–17470.

(48) Duvanel, G.; Grilj, J.; Vauthey, E. Ultrafast Long-Distance Excitation Energy Transport in Donor–Bridge–Acceptor Systems. *J. Phys. Chem. A* **2013**, *117*, 918–928.

(49) Pelton, M.; Sader, J. E.; Burgin, J.; Liu, M.; Guyot-Sionnest, P.; Gosztola, D. Damping of Acoustic Vibrations in Gold Nanoparticles. *Nat. Nanotech.* **2009**, *4*, 492–495. 90.

(50) Hodak, J. H.; Henglein, A.; Hartland, G. V. Size Dependent Properties of Au Particles: Coherent Excitation and Dephasing of Acoustic Vibrational Modes. *J. Chem. Phys.* **1999**, *111*, 8613–8621.

(51) Yu, S.; Zhang, J.; Tang, Y.; Ouyang, M. Engineering Acoustic Phonons and Electron–Phonon Coupling by the Nanoscale Interface. *Nano Lett.* **2015**, *15* (9), 6282–6288.

(63) Dowgiallo, A.-M.; Schwartzberg, A. M.; Knappenberger, K. L. Structure-Dependent Coherent Acoustic Vibrations of Hollow Gold Nanospheres. *Nano Lett.* **2011**, *11*, 3258–3262.

(53) Guillon, C.; Langot, P.; Del Fatti, N.; Vallée, F.; Kirakosyan, A. S.; Shahbazyan, T. V.; Cardinal, T.; Treguer, M. Coherent Acoustic Vibration of Metal Nanoshells. *Nano Lett.* **2007**, *7*, 138–142.

(54) Del Fatti, N.; Voisin, C.; Chevy, F.; Vallée, F.; Flytzanis, C. Coherent Acoustic Mode Oscillation and Damping in Silver Nanoparticles. *J. Chem. Phys.* **1999**, *110*, 11484–11487.

Chapter 3. Monitoring the Seed-Mediated Growth of Gold Nanoparticles using *In-Situ* Second Harmonic Generation

3.1 Introduction

Colloidal gold nanoparticles have received considerable attention due to their potential applications in molecular sensing, photovoltaics, catalysis, imaging, nanomedicine, and photothermal therapy.[1-14] These applications rely heavily on the localized surface plasmon resonance (LSPR) from coherent oscillations of free electrons that lead to optical field enhancements at the nanoparticle surface.[15] The optical properties of gold nanoparticles can be tuned depending on the desired application by changing the nanoparticle size, shape, and surrounding medium.[16,17] Varying the nanoparticle size causes only minor changes in the extinction spectra for gold nanospheres of diameters ranging from approximately 12 to 200 nm.[13] However, varying the gold nanosphere shape by elongating it into a nanorod[18] or by creating a bumpy "urchin-like" surface[19] leads to pronounced changes in the associated optical properties. Therefore, developing synthetic protocols for greater control and tunability over the associated surface chemistry is critical for developing gold nanoparticle-based applications.[13,16]

Citrate-stabilized gold nanoparticles prepared by the reduction of a gold chloride salt ($HAuCl_4$) with sodium citrate ($Na_3C_6H_5O_7$) in water remains one of the most common synthetic methods for producing spherical gold nanoparticles.[20] By varying reaction conditions, such as the citrate to gold salt ratio and the aqueous pH, it is possible to obtain gold nanoparticles ranging from 5 to 150 nm in diameter.[21] However, the gold nanoparticle sample polydispersity is often very large with nonuniform surfaces when using this method to prepare nanoparticles larger than 30 nm in diameter.[22,23] In

order to gain better control over the nanoparticle size and shape distributions, an additional seed-mediated growth step can be used where additional gold salt is selectively reduced on the surface of the colloidal citrate-stabilized gold seeds using hydroquinone. This seed-mediated nanoparticle growth procedure results in spherical gold nanoparticles with sizes ranging from 50 to 200 nm while minimizing unwanted secondary nucleation for improved monodispersity and uniform surface morphologies.[24]

Characterization techniques such as transmission electron microscopy (TEM), scanning electron microscopy (SEM), and atomic force microscopy (AFM) are excellent for studying nanoparticle size and shape distributions *ex-situ* and post-synthesis. However, monitoring nanoparticle surface formation *in-situ* can provide important additional insight into the growth dynamics for better control over surface and optical properties. The growth of gold nanoparticles by citrate reduction in water has been studied using *in-situ* small-angle X-ray scattering (SAXS) where the results indicate that the gold nanoparticles formation occurs in a four step mechanism.[25] Additionally, gold nanoshells grown on silica microparticles have been studied using *in-situ* nonlinear second-harmonic scattering (SHS) where the large SHS signal during the growth process is attributed to electric-field enhancements in gaps of incomplete or uneven nanoshells.[26] Here, large nonlinear optical field enhancements are dependent on the metal nanoparticle shape as well as the surface roughness. For example, fundamental studies have investigated the SHG electric field enhancements from rough metal surfaces and sharp metal tips, both experimentally and theoretically, where the localized plasmon resonance contributes to the electrostatic “lightning-rod effect.”[27,28]

Second-harmonic generation (SHG) is a noninvasive nonlinear spectroscopic technique in which two incident photons of frequency ω coherently add to produce a third photon of frequency 2ω.[29-33] This process is forbidden in bulk media with a center of inversion symmetry. However, SHG is allowed at interfaces, making SHG a powerful tool for studying colloidal nanoparticle surfaces. Previous work has used SHG to investigate TiO_2 microparticles,[34] liposomes,[35,36] and metal nanoparticles made of gold, silver, and gold-silver alloys.[3,4,37-43] *In-situ* SHG coupled with extinction spectroscopy provides important information that can be used to characterize the nanoparticle growth dynamics for potential advances in colloidal nanoparticle engineering and associated applications. Here we demonstrate the versatility of SHG by monitoring the seed-mediated growth process of gold nanoparticles using *in-situ* SHG and extinction spectroscopy. Time-dependent changes in the SHG signal as a function of the reaction time are fit to exponential functions to obtain the associated growth lifetimes under different initial gold seed concentrations. The final nanoparticle sizes are determined using extinction spectroscopy and TEM measurements. The measured growth lifetimes depend on the final nanoparticle diameter where larger nanoparticles have corresponding longer growth lifetimes. By comparing the *in-situ* SHG results with extinction spectroscopy, an intermediate growth stage attributed to a rough, nonuniform nanoparticle surface is observed through inhomogeneous spectral broadening followed by a narrowing and blue-shifting of the plasmon spectrum. This correlates with the *in-situ* SHG results where a size-dependent maximum in the SHG signal is measured due to the rough, bumpy surface during the initial nanoparticle growth process. The versatility of *in-situ* SHG measurements combined with *in-situ* extinction spectroscopy

enables a wide range of investigations for studying nanoparticle growth and functionalization in real time for developing new nanomaterials and associated applications.

3.2 Gold Nanoparticle Synthesis

The colloidal gold nanoparticle samples are prepared by a seeded-growth technique using hydroquinone (HQ) as the reducing agent.[23, 24] The gold seeds are prepared by adding 900 µL of 34 mM sodium citrate ($Na_3C_6H_5O_7$) to 30 mL of 290 µM gold tetrachloride ($HAuCl_4$) in water under boiling and vigorous stirring conditions. Five gold nanoparticle samples of different sizes are synthesized by adding 25 µL, 30 µL, 35 µL, 40 µL, and 50 µL of the prepared gold seeds, respectively, to 25 µL of 29 mM $HAuCl_4$ which are all diluted to a final volume of 2.5 mL with ultrapure water. The addition of the reducing agents using 25 µL of 0.03 M HQ and 5 µL of 34 mM sodium citrate initiates the growth process. For each sample, the final solution is left to stir at room temperature for 60 minutes.

3.3 *In-Situ* Second Harmonic Generation and Extinction Spectroscopy

The SHG setup uses an ultrafast oscillator laser, an optical setup, and a high sensitivity charge-coupled device (CCD) detector connected to a monochromator/spectrograph, modified from our previous work.[3,4] A titanium:sapphire oscillator laser produces 75 fs pulses centered at 800 nm with a repetition rate of 80 MHz and an average power of 2.7 W. The laser beam is attenuated to 600 mW and is focused into a 1 cm quartz cuvette containing the gold seeds, $HAuCl_4$, HQ, and sodium citrate in the various gold nanoparticle reaction conditions. An optical filter is placed in front of the cuvette to remove any residual SHG prior to the sample. Another filter is

placed after the sample to remove the fundamental light while transmitting the SHG, which is collected in the forward direction and refocused into the monochromator. This optical setup allows for the detection of the SHG signal as a function of time in order to capture nanoparticle reaction dynamics. At the same time, the *in-situ* extinction spectroscopy is measured using a broadband tungsten filament lamp which is collimated using a pair of lenses and focused orthogonal to the SHG beam and into the quartz cuvette with the resulting spectra detected using a fiber optic spectrometer detector. For each trial, the precursor gold seeds and $HAuCl_4$ are added in ultrapure water for a baseline SHG measurement. At time zero (t=0), HQ and sodium citrate are added simultaneously to initiate the nanoparticle growth process.

3.4 Results

After the nanoparticle synthesis is completed, TEM images are acquired surveying approximately 200 nanoparticles for each nanoparticle sample. The nanoparticle sizes are measured and fit using a log-normal distribution to obtain the average nanoparticle diameter, as shown in the Supporting Information, for each sample. Figure 3.1 shows TEM images that are representative of each gold nanoparticle sample with sizes of 92.2 $\pm$ 4.0 nm, 86.1 $\pm$ 4.3 nm, 72.6 $\pm$ 5.3 nm, 71.3 $\pm$ 4.8 nm, and 65.6 $\pm$ 5.0 nm synthesized from 25, 30, 35, 40, and 50 μL of precursor gold seeds, respectively. The average nanoparticle size is also confirmed by fitting each final extinction spectrum using Mie theory with corresponding sizes of 94, 89, 76, 72, and 66 nm, respectively, which are within the standard deviations of the sizes measured from TEM.

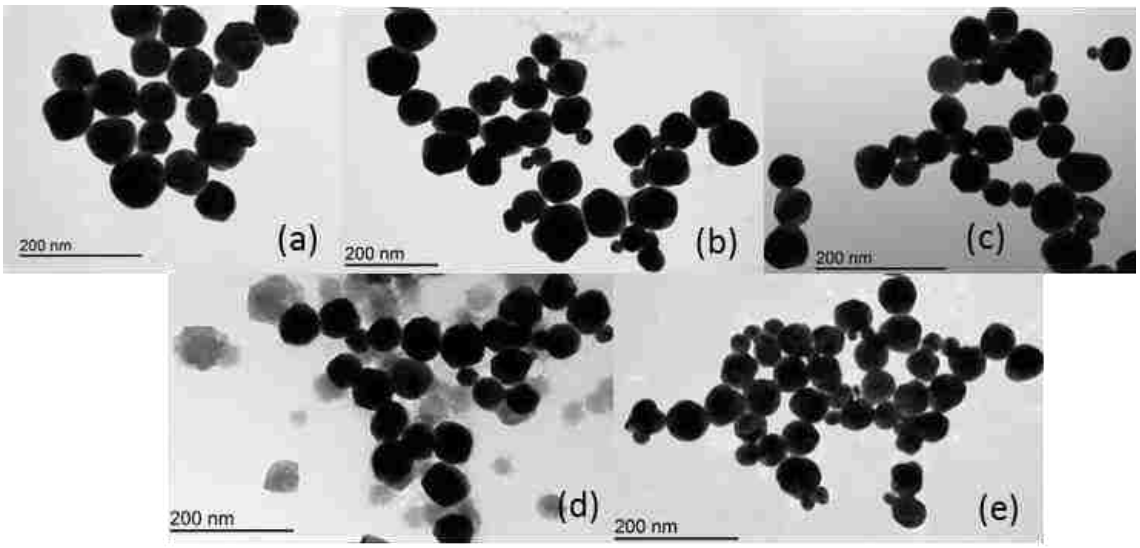

Figure 3.1. Representative TEM images of gold nanoparticles with average sizes of (a) 92.2 ± 4.0 nm, (b) 86.1 ± 4.3 nm, (c) 72.6 ± 5.3 nm, (d) 71.3 ± 4.8 nm, and (e) 65.6 ± 5.0 nm prepared using 25, 30, 35, 40, and 50 µL of precursor gold seeds, respectively.

The final extinction spectrum using 25 µL of precursor gold seeds is shown in Figure 3.2, compared with the Mie theory fit. The results from the other nanoparticle samples are shown in Appendix B.

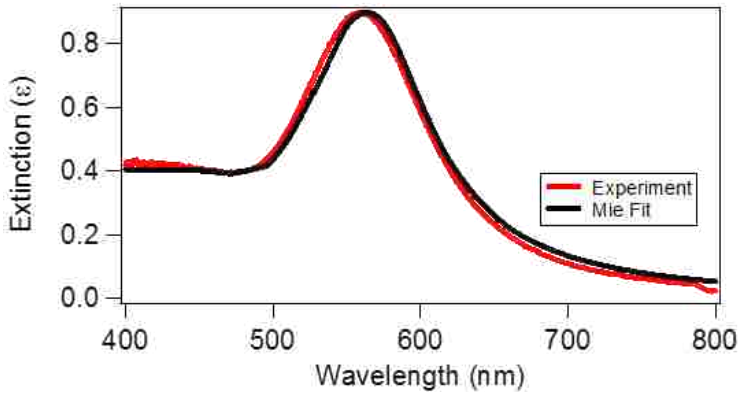

Figure 3.2. Final extinction spectrum (red line) of gold nanoparticles prepared using 25 µL of precursor gold seeds compared to corresponding fit (black line) from Mie theory.

The temporal evolution of the SHG electric field for each nanoparticle sample is shown in Figure 3.3.

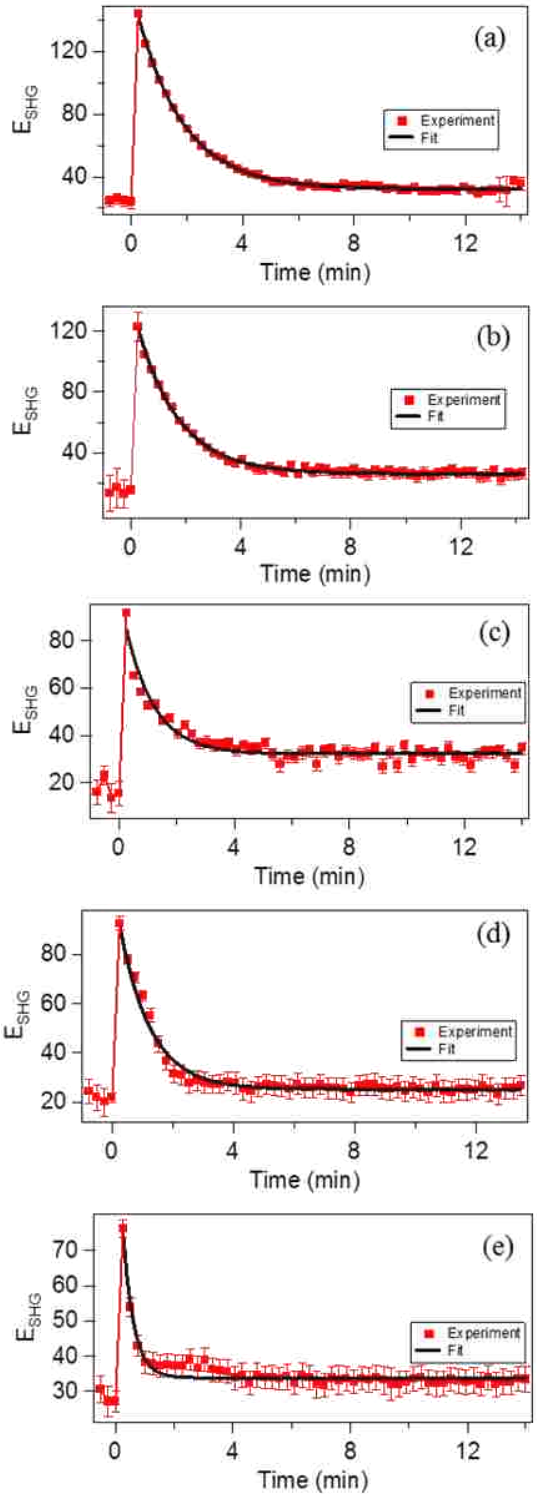

Figure 3.3. SHG electric field (red squares) as a function of reaction time of gold nanoparticles using (a) 25 µL, (b) 30 µL, (c) 35 µL, (d) 40 µL, and (e) 50 µL of precursor gold seeds, respectively, compared to the fits (black lines).

The SHG electric field is taken as the square root of the integrated SHG signal. Before the growth process is initiated at time zero, a baseline SHG intensity is measured for all samples, which contains contributions of SHG from the precursor seeds as well as hyper-Rayleigh scattering[44] from the aqueous solvent. After adding the reducing agents HQ and sodium citrate, a sharp increase in the SHG electric field is observed followed by a size-dependent exponential decay for all samples. Representative *in-situ* SHG spectra of the 25 µL precursor gold sample at selected reaction times are shown in Figure 3.4. Additional *in-situ* SHG spectra from other samples are displayed in the Supporting Information. The *in-situ* SHG spectra are fit with a Gaussian function to obtain a central wavelength of 400 nm and a full width at half-maximum of 4.8 nm, which are constant values throughout the growth process for each nanoparticle sample.

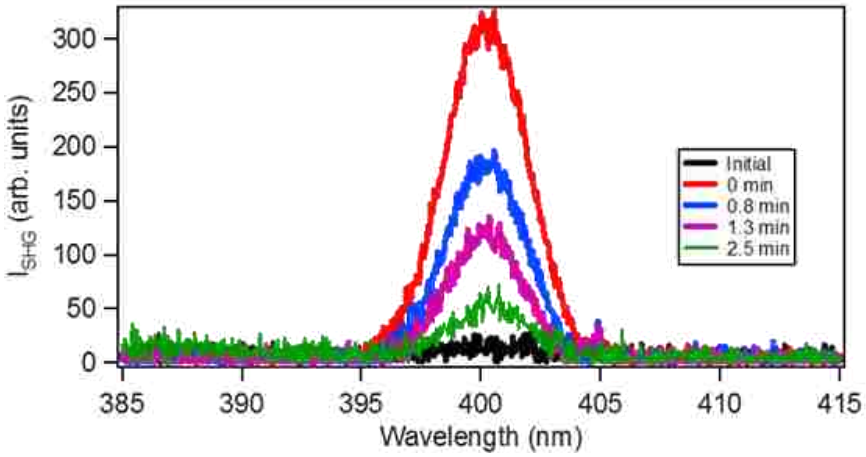

Figure 3.4. SHG spectra for gold nanoparticles prepared using 25 µL of precursor gold seeds at different times during the reaction.

The SHG electric field time profile for each nanoparticle sample provides surface-sensitive information on the seed-mediated growth process. A maximum in the SHG electric field is observed in the initial stage of growth, shortly after time zero. The peak SHG for the 25 µL precursor gold seed sample shows approximately an order of magnitude increase in SHG intensity, which can be attributed to the initial stage in the

reaction, characterized by inhomogeneous growth of the nanoparticles with rough surfaces giving rise to plasmonic hot-spots. As the reaction proceeds, the sharp SHG feature exponentially decays where the characteristic growth lifetime is observed to be longer for larger nanoparticles. This indicates that the second stage in the reaction is described by the nanoparticle surface becoming more smooth and uniform over time, leading to a decrease plasmonic hot spots and a lower SHG intensity. Finally, the nanoparticles reach their final morphology characterized by a relatively smooth surface where the reaction is complete and the SHG signal remains constant over time.

The *in-situ* extinction spectra from gold nanoparticle growth provides additional and complementary insight on the seed-mediated nanoparticle reaction. Representative extinction spectra at various times during the reaction for the 25 µL precursor gold seed sample are shown in Figure 3.5. Additional *in-situ* extinction spectra are shown in Appendix B.

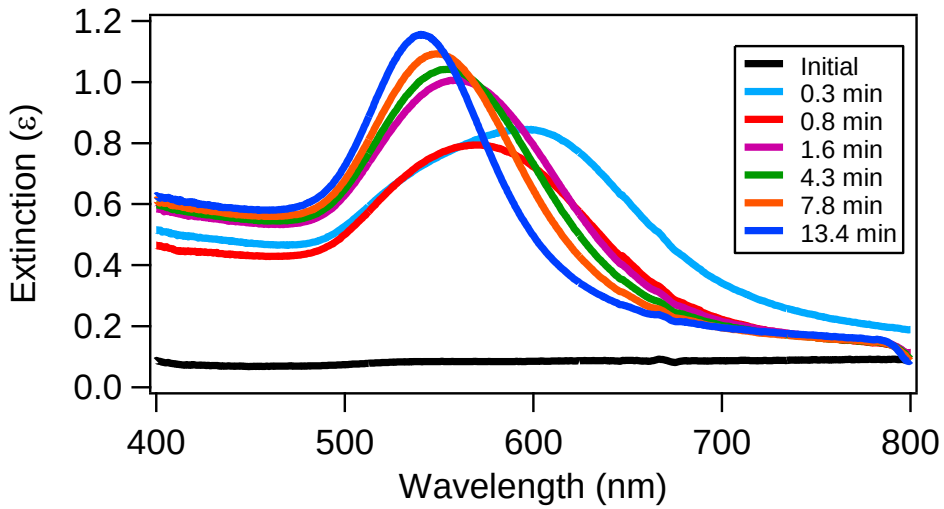

Figure 3.5. *In-situ* extinction of gold nanoparticles prepared using 25 µL of precursor gold seeds at different times during the reaction.

Prior to the start of the nanoparticle growth reaction, a baseline extinction spectrum is taken showing the absorption and scattering profile of the 15 nm gold precursor seeds

along with the added gold chloride solution. Immediately after the addition of the reducing agents, a broad plasmon peak centered near 600 nm is observed, which is attributed to a polydisperse distribution and an uneven, rough nanoparticle surface.[22] As the nanoparticle growth reaction proceeds, this broad plasmon peak narrows to a wavelength centered near 575 nm indicating a more uniform surface and reduction in polydispersity. During the final stage of the reaction the plasmon peak continues to narrow and blue shifts as the nanoparticle surface reaches its final, smooth morphology with a final spectrum that is very stable over time and agrees with the corresponding Mie theory fit. Previous studies have investigated the formation of a “blackberry-like” intermediate stage that smoothens out over the course of the reaction, which is consistent with our *in-situ* SHG results.[45]

The size-dependent growth dynamics of the gold nanoparticles are analyzed in more detail to obtain the corresponding growth lifetimes. The SHG electric field time trace for each nanoparticle sample is fit using an exponential function given by $E_{SHG}(t) = y_0 + Ae^{-\frac{t}{\tau}}$, where t is the reaction time after the addition of the reducing agents, τ is the growth lifetime, A is the amplitude, and y_0 is the offset. The fits for each nanoparticle sample are shown in Figure 3.4 and the best fit parameters are tabulated in the Supporting Information. The resulting growth lifetimes are plotted as a function of the final nanoparticle diameter Figure 3.6 (a). These growth lifetimes decrease as the final nanoparticle diameter decreases with values of 1.66 $\pm$ 0.01 min, 1.50 $\pm$ 0.01 min, 1.06 $\pm$ 0.08 min, 0.98 $\pm$ 0.03 min, and 0.37 $\pm$ 0.23 min for the 94 nm, 90 nm, 75 nm, 72 nm, and 66 nm nanoparticles, respectively. The general trend in these lifetimes is in

agreement with previous studies observing that the growth rate is proportional to the amount of precursor seeds.[46]

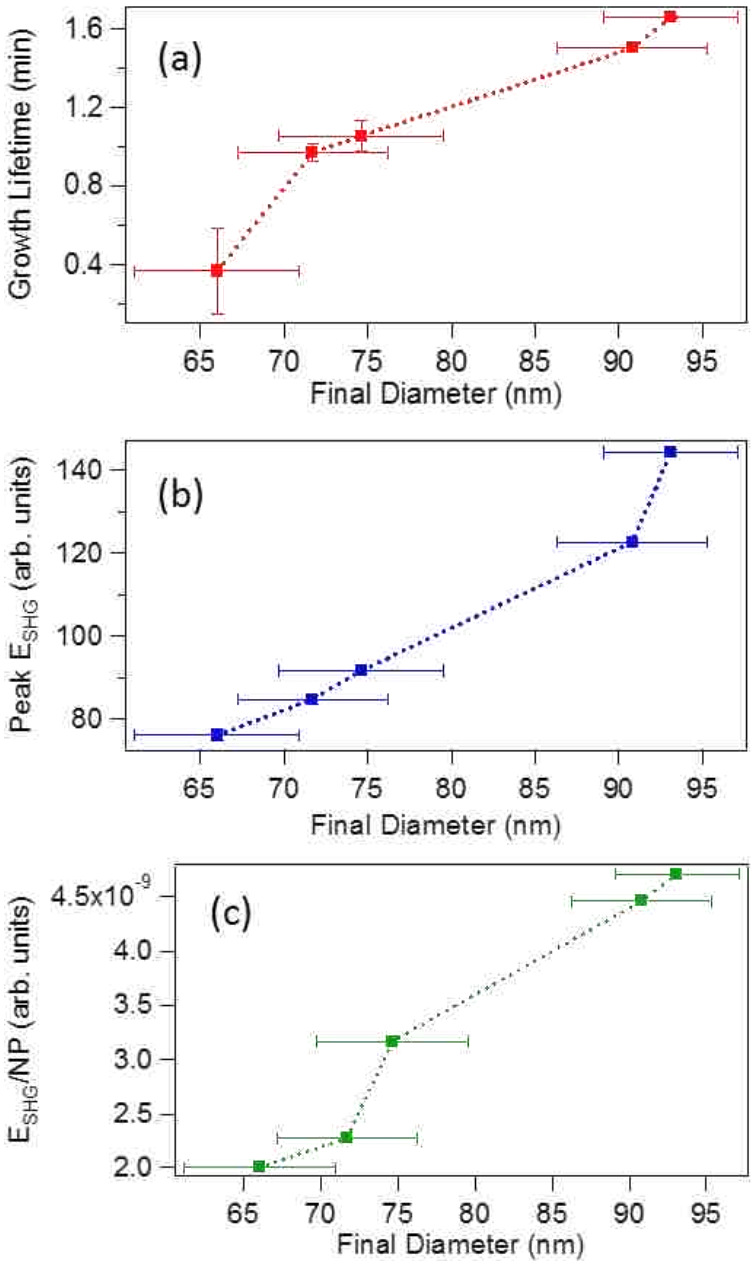

Figure 3.6. (a) Analysis of growth lifetime, τ, as a function of final nanoparticle diameter. (b) Peak SHG electric field as a function of final nanoparticle diameter. (c) Final SHG electric field per nanoparticle.

The *in-situ* SHG time profiles and corresponding extinction spectra of the seed-mediated gold nanoparticle growth dynamics are consistent with a two-step process.

The first step is characterized by a rapid growth resulting in an uneven, bumpy surface and a high surface concentration of plasmonic hot spots. The second step is characterized by the nanoparticle surface becoming more smooth over time resulting in increased monodispersity, narrowing plasmonic spectra, and lower, more stable SHG signals as the nanoparticle surface reaches thermodynamic equilibrium under a characteristic size-dependent exponential growth lifetime. The peak SHG electric field, shown in Figure 3.6 (b), is observed to increase as the final nanoparticle diameter increases. The addition of sodium citrate reduces Au^{III} to Au^{I} followed by the selective reduction by HQ of Au^{I} adsorbed on the seed surface.[19,24,45] Lower seed concentrations here correspond to higher concentrations of Au^{0} adsorbed to each nanoparticle surface to produce larger gold nanoparticles. A higher Au^{0} to seed ratio has been observed to promote the formation of urchin-like gold nanoparticles with high surface energy facets.[19] These higher surface energy facets produce plasmonic hotspots corresponding to the large SHG signals observed here shortly after time zero. These uneven surface energy facets that form under high concentrations of Au^{0} in the presence of HQ become less bumpy in morphology over time,[19] reaching a thermodynamic equilibrium corresponding to a relatively smooth gold nanoparticle surface according to a size-dependent exponential time profile. Additionally, using the baseline SHG for each nanoparticle sample after the reaction is complete, the contribution to the SHG electric field per nanoparticle is determined, as plotted in Figure 3.6 (c). These results demonstrate that the larger gold nanoparticles have a higher SHG signal, in agreement with previous theoretical work on the enhancement of the second-harmonic field from different spherical nanoparticles.[48,49] Overall, the *in-situ* SHG and extinction

measurements provide crucial insight for monitoring the colloidal seed-mediated gold nanoparticle growth reaction under varying synthesis conditions.

3.5 Conclusion

In summary, we have demonstrated the versatility of *in-situ* SHG in the investigation of size-dependent seed-mediated gold nanoparticle growth dynamics in water. The *in-situ* SHG and extinction spectroscopy results are consistent with a two-step growth process. During the first step of the nanoparticle growth reaction, rough and uneven surfaces are formed rapidly giving rise to plasmonic hot spots that dramatically enhance the SHG electric field and have corresponding broad, red-shifted plasmonic spectra. In the second step, the nanoparticle surface becomes smoother, reaching a thermodynamic equilibrium over a corresponding size-dependent exponential growth lifetime that results in a final nanoparticle sample with a lower, more stable SHG signal and corresponding narrower, blue-shifted plasmonic spectra that agrees with Mie theory. The seed-mediated nanoparticle growth lifetimes measured using *in-situ* SHG are faster for smaller final gold nanoparticle sizes, varying from 0.37 min to 1.7 min for final nanoparticle sizes of 66 nm and 93 nm, respectively. These *in-situ* SHG and extinction spectroscopy techniques provide complimentary information that can be used to monitor colloidal nanoparticle growth dynamics for improving nanomaterial synthesis and characterization.

3.6 References

(1) El-Sayed, I. H.; Huang, X.; El-Sayed, M. A. Surface plasmon resonance scattering and absorption of anti-EGFR antibody conjugated gold nanoparticles in cancer diagnostics: applications in oral cancer. Nano Lett. **2005**, 5, 829−834.

(2) Haes, A. J.; van Duyne, R. P. A nanoscale optical biosensor: sensitivity and selectivity of an approach based on the localized surface plasmon resonance

spectroscopy of triangular silver nanoparticles. J. Am. Chem. Soc. **2002**, 124, 10596−10604.

(3) Karam, T. E.; Haber, L. H. Molecular adsorption and resonance coupling at the colloidal gold nanoparticle interface. J. Phys. Chem. C **2013**, 118, 642−649.

(4) Kumal, R. R.; Karam, T. E.; Haber, L. H. Determination of the Surface Charge Density of Colloidal Gold Nanoparticles Using Second Harmonic Generation. *J. Phys. Chem. C* **2015**, *119*, 16200–16207.

(5) Kamat, P. V. Meeting the clean energy demand: nanostructure architectures for solar energy conversion. J. Phys. Chem. C **2007**, 111, 2834−2860.

(6) Kholmicheva, N.; Moroz, P.; Rijal, U.; Bastola, E.; Uprety, P.; Liyanange, G.; Razgoniaev, A.; Ostrowski, A. D.; Zamkov, M. Plasmonic Nanocrystal Solar Cells Utilizing Strongly Confined Radiation. ACS Nano **2014**, 8, 12549-12559.

(7) Narayanan, R.; El-Sayed, M. A. Catalysis with transition metal nanoparticles in colloidal solution: nanoparticle shape dependence and stability. J. Phys. Chem. B **2005**, 109, 12663−12676.

(8) Kamat, P. V. Photophysical, photochemical and photocatalytic aspects of metal nanoparticles. J. Phys. Chem. B **2002**, 106, 7729−7744.

(9) Sperling, R. A.; Gil, P. R.; Zhang, F.; Zanella, M.; Parak, W. J. Biological applications of gold nanoparticles. Chem. Soc. Rev. **2008**, 37, 1896−1908.

(10) Kumal, R. R.; Landry, C. R.; Abu-Laban, M.; Hayes, D. J.; Haber, L.H. Monitoring the photocleaing Dynamics of Colloidal MicroRNA-Functionalized Gold Nanoparticles Using Second Harmonic Generation. Langmuir **2015**, 31, 9983-9990.

(11) Prigodich, A. E.; Lee, O.-S.; Daniel, W. L.; Seferos, D. S.; Schatz, G. C.; Mirkin, C. A. Tailoring DNA Structure to Increase Target Hybridization Kinetics on Surfaces. J. Am. Chem. Soc. **2010**, 132, 10638−10641.

(12) Huang, X.; El-Sayed, I. H.; Qian, W.; El-Sayed, M. A. Cancer cell imaging and photothermal therapy in the near-infrared region by using gold nanorods. J. Am. Chem. Soc. **2006**, 128, 2115−2120.

(13) Link, S.; El-Sayed, M. A. Shape and size dependence of radiative, non-radiative and photothermal properties of gold nanocrystals. Int. Rev. Phys. Chem. **2000**, 19, 409−453.

(14) Karam, T. E.; Smith, H. T.; Haber, L. H. Enhanced Photothermal Effects and Excited-State Dynamics of Plasmonic Size-Controlled Gold-Silver-Gold Core-Shell-Shell Nanoparticles. J. Phys. Chem. C **2015**, 119, 18573-18580.

(15) Chandra, M.; Dowgiallo, A.-M.; Knappenberger, K. L., Jr Controlled plasmon resonance properties of hollow gold nanosphere aggregates. J. Am. Chem. Soc. **2010**, 132, 15782−15789.

(16) Daniel, M.-C.; Astruc, D. Gold Nanoparticles: Assembly, Supramolecular Chemistry, Quantum-Size-Related Properties, and Applications toward Biology, Catalysis, and Nanotechnology. Chem. Rev. **2004**, 104, 293−346.

(17) Hu, M.; Novo, C.; Funston, A.; Wang, H.; Staleva, H.; Zou, S.; Mulvaney, P.; Xia, Y.; Hartland, G. V. Dark-Field Microscopy Studies of Single Metal Nanoparticles: Understanding the Factors That Influence the Linewidth of the Localized Surface Plasmon Resonance. *J. Mater. Chem.* **2008**, *18*, 1949–1960.

(18) Nikoobakht, B.; El-Sayed, M. A. Preparation and Growth Mechanism of Gold Nanorods (NRs) Using Seed-Mediated Growth Method. Chem. Mater. **2003**, 15, 1957-1962.

(19) Li, J.; Wu, J.; Zhang, X.; Liu, Y.; Zhou, D.; Sun, H.; Zhang, H.; Yang, B. Controllable Synthesis of Stable Urchin-like Gold Nanoparticles Using Hydroquinone to Tune the Reactivity of Gold Chloride. *J. Phys. Chem. C* **2011**, *115*, 3630–3637.

(20) Frens, G. Controlled Nucleation for the Regulation of the Particle Size in Monodisperse Gold Suspensions. Nature, Phys. Sci. **1973**, 241, 20–22.

(21) Turkevitch, J.; Stevenson, P. C.; Hillier, J. Nucleation and Growth Process in the Synthesis of Colloidal Gold. Discuss. Faraday Soc. **1951**, 11, 55-75.

(22) Kimling, J.; Maier, M.; Okenve, B.; Kotaidis, V.; Ballot, H.; Plech, A. Turkevich Method for Gold Nanoparticle Synthesis Revisited. J. Phys. Chem. B. **2006**, 110, 15700-15707.

(23) Brown, K. R.; Walter, D. G.; Natan, M. J. Seeding of Colloidal Au Nanoparticle Solutions. 2. Improved Control of Particle Size and Shape. Chem. Mater. **2000**, 12, 306-313.

(24) Perrault, S. D.; Chan, W. C. Synthesis and Surface Modification of Highly Monodispersed, Spherical Gold Nanoparticles of 50-200 nm. J. Am. Chem. Soc. **2009**, 131, 17042-17043.

(25) Polte, J.; Ahner, T. T.; Delissen, F.; Sokolov, S.; Emmerling, F.; Thunemann, F.; Kraehnert, R. Mechanism of Gold Nanoparticle Formation in the Classical Citrate

Synthesis Method Derived from Coupled In Situ XANES and SAXS Evaluation. J. Am. Che. Soc. **2010**, 132, 1296-1301.

(26) Sauerbeck C.; Haderlein, M.; Schurer, B.; Braunschweig, B.; Peukert, W.; Klupp Taylor, R. N. Shedding Light on the Growth of Gold Nanoshells. ACS Nano **2014**, 8, 3088-3096.

(27) Boyd, G. T.; Rasing, T.; Leite, J. R. R.; Shen, Y. R. Local-Field Enhancement on Rough Surfaces of Metals, Semimetals, and Semiconductors with the Use of Optical Second-Harmonic Generation. *Phys. Rev. B Condens. Matter* **1984**, *30*, 519–526.

(28) Bouhelier, A.; Beversluis, M.; Hartschuh, A.; Novotny, L. Near-Field Second-Harmonic Generation Induced by Local Field Enhancement. *Phys. Rev. Lett.* **2003**, *90*, 013903.

(29) Eisenthal, K. Second Harmonic Spectroscopy of Aqueous Nanoand Microparticle Interfaces. Chem. Rev. **2006**, 106, 1462−1477.

(30) Yan, E. C. Y.; Liu, Y.; Eisenthal, K. B. New Method for Determination of Surface Potential of Microscopic Particles by Second Harmonic Generation. *J. Phys. Chem. B* **1998**, *102*, 6331–6336.

(31) Jen, S.-H.; Gonella, G.; Dai, H.-L. The Effect of Particle Size in Second Harmonic Generation from the Surface of Spherical Colloidal Particles. I: Experimental Observations. *J. Phys. Chem. A* **2009**, *113*, 4758–4762.

(32) Shen, Y. R. Surface Properties Probed by Second-Harmonic and Sum-Frequency Generation. *Nature* **1989**, *337*, 519.

(33) Hayes, P. L.; Malin, J. N.; Jordan, D. S.; Geiger, F. M. Get Charged up: Nonlinear Optical Voltammetry for Quantifying the Thermodynamics and Electrostatics of Metal Cations at Aqueous/oxide Interfaces. *Chem. Phys. Lett.* **2010**, *499*, 183–192.

(34) Liu, Y.; Dadap, J.; Zimdars, D.; Eisenthal, K. B. Study of Interfacial Charge-Transfer Complex on TiO2 Particles in Aqueous Suspension by Second-Harmonic Generation. J. Phys. Chem. B **1999**, 103, 2480−2486.

(35) Liu, J.; Subir, M.; Nguyen, K.; Eisenthal, K. B. Second Harmonic Studies of Ions Crossing Liposome Membranes in Real Time. J. Phys. Chem. B **2008**, 112, 15263−15266.

(36) Kumal, R. R.; Nguyenhuu, H.; Winter, J. E.; McCarley, R. L.; Haber, L. H. Impacts of Salt, Buffer, and Lipid Nature on Molecular Adsorption and Transport in

Liposomes As Observed by Second Harmonic Generation. *J. Phys. Chem. C* **2017**, *121*, 15851–15860.

(37) Vance, F. W.; Lemon, B. J.; Hupp, J. T. Enormous HyperRayleigh Scattering from Nanocrystalline Gold Particle Suspensions. J. Phys. Chem. B **1998**, 102, 10091−10093.

(38) Gan, W.; Gonella, G.; Zhang, M.; Dai, H.-L. Communication: Reactions and Adsorption at the Surface of Silver Nanoparticles Probed by Second Harmonic Generation. *J. Chem. Phys.* **2011**, *134*, 041104.

(39) Haber, L. H.; Kwok, S. J. J.; Semeraro, M.; Eisenthal, K. B. Probing the Colloidal Gold Nanoparticle/Aqueous Interface with Second Harmonic Generation. Chem. Phys. Lett. **2011**, 507,11–14.

(40) Hao, E. C.; Schatz, G. C.; Johnson, R. C.; Hupp, J. T. HyperRayleigh scattering from silver nanoparticles. J. Chem. Phys. **2002**, 117, 5963−5966.

(41) Russier-Antoine, I.; Benichou, E.; Bachelier, G.; Jonin, C.; Brever, P. F. Multipolar Contributions of the Second Harmonic Generation from Silver and Gold Nanoparticles. J. Phys. Chem. C **2007**, 111, 9044−9048.

(42) Jin, R.; Jureller, J.; Kim, H.; Scherer, N. Correlating Second Harmonic Optical Responses of Single Ag Nanoparticles with Morphology. J. Am. Chem. Soc. **2005**, 127, 12482−12483.

(43) Bachelier, G.; Butet, J.; Russier-Antoine, I.; Jonin, C.; Benichou, E.; Brevet, P.-F. Origin of Optical Second-Harmonic Generation in Spherical Gold Nanoparticles: Local Surface and Nonlocal Bulk Contributions. *Phys. Rev. B Condens. Matter.* **2010**, *82*, 235403.

(44) Gomopoulos, N.; Lütgebaucks, C.; Sun, Q.; Macias-Romero, C.; Roke, S. Label-Free Second Harmonic and Hyper Rayleigh Scattering with High Efficiency. *Opt. Express* **2013**, 21, 815–821.

(45) Ziegler, C.; Eychmüller, A. Seeded Growth Synthesis of Uniform Gold Nanoparticles with Diameters of 15−300 Nm. *J. Phys. Chem. C* **2011**, 115, 4502–4506.

(46) Jana, N. R.; Gearheart, L.; Murphy, C. J. Evidence for Seed-Mediated Nucleation in the Chemical Reduction of Gold Salts to Gold Nanoparticles. *Chem. Mater.* **2001**, 13, 2313–2322.

(47) Kumar, S.; Gandhi, K. S.; Kumar, R. Modeling of Formation of Gold Nanoparticles by Citrate Method. *Ind. Eng. Chem. Res.***2007**, 46, 3128–3136.

(48) Dadap, J. I.; Shan, J.; Eisenthal, K. B.; Heinz, T. F. Second-Harmonic Rayleigh Scattering from a Sphere of Centrosymmetric Material. *Phys. Rev. Lett.* **1999**, 83, 4045–4048.

(49) de Beer, A. G. F.; Roke, S. Nonlinear Mie Theory for Second-Harmonic and Sum-Frequency Scattering. *Phys. Rev. B Condens. Matter* **2009**, 79, 155420.

Chapter 4. Ultrafast Carrier Dynamics in Self-Assembled $La_{1-x}Sr_xMnO_3/SrTiO_3$ Heterostructures

4.1 Introduction

Transition metal oxide (TMO) thin films and heterostructures have attracted the interest of the scientific community due to the manifestation of broken symmetry and dimensional confinement which create new forms of coupling between charge, orbit, spin, and lattice, leading to new functionalities.[1] For perovskite manganites, manipulating the film or heterostructure dimensions reveals interesting phenomena such as thickness-dependent metal-insulator transitions, reemergent magnetic order, and ferroelectric behavior.[2-4] These artificially structured materials are frequently investigated by very powerful methods capable of probing the ground state, but an important challenge is to probe excited states, especially those far from equilibrium. Ultrafast reflectivity measurements can be used to study these systems in highly non-equilibrium exited states and to observe subsequent dynamical behavior on the timescales of electronic and atomic motion, offering insight on the nature of both electron-phonon and phonon-phonon interactions.[5-7] We have grown self-assembled $La_{1-x}Sr_xMnO_3/SrTiO_3$ (LSMO/STO) (001) structures which result in structural and compositional modulation near the interface, profoundly changing the electronic and magnetic properties of these thin films.[8] In this chapter, using ultrafast reflectivity measurements we show novel excited-state relaxation dynamics and phonon oscillations in these LSMO/STO heterostructures.

4.2 Sample Preparation

The sample used for this experiment is $La_{1-x}Sr_xMnO_3$ grown on a STO (001) substrate, in collaboration with Dr. Plummer's research group at LSU, using pulsed

laser deposition under conditions described elsewhere.[8] Briefly, a stoichiometrically precise compact-powdered $La_{0.67}Sr_{0.33}MnO_3$ target is ablated using a high powered pulsed fiber laser. The ablated plasma condenses on the STO surface in a cell by cell deposition. Conventionally, this growth is done under 80 mTorr oxygen/ozone pressure while the samples used in this dissertation are grown in a 40 mTorr oxygen/ozone mixture creating relatively deficient oxygen conditions. Compared to conventionally grown LSMO thin films, these modified growth conditions create two distinct regions in the thin film as shown in Figure 4.1 where the 8-10 unit cell region (green) above the substrate contains a higher concentration of La ions relative to the bulk (blue).[8] The high La concentration region at this interface alters the magnetic properties of the material and can manifest as spontaneous magnetic reversal. These interactions can be used for room temperature magnetic switching where the net magnetic moment of the thin film can be flipped by applying a weak magnetic field.[8]

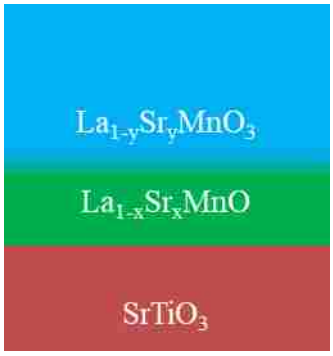

Figure 4.1. Thin-film of LSMO/STO showing the STO bulk (red), LSMO interface (green), and LSMO bulk (blue).

The bulk structure of LSMO is rhombohedral with space group $R\bar{3}c$ (No. 167).[9] The material class of perovskites (ABO_3) are unique in their octahedral tilt degrees of freedom which can be described shorthand using Glazer's notation.[10] For bulk LSMO

the Glazer notation is $a^-a^-a^-$, which denotes equal tilting in the x, y, and z axes.[11] STO possesses cubic structure where there is no tilt and rotation ($a^0a^0a^0$).

By simply tilting and/or rotating the oxygen cage, both structural and physical properties can be changed through doping. In the prepared $La_{0.67}Sr_{0.33}MnO_3$ film, doping with Sr (green region Figure 4.1) causes a strain creating an octahedral oxygen tilt up to 6° due to the large ionic radii. In perovskites, chemical doping provides an avenue of control over the B-O-B orbital overlap by inducing unit cell strain.[12] The $La_{0.67}Sr_{0.33}MnO_3/SrTiO_3$ (LSMO/STO) heterostructure is an interesting perovskite to study due to having the highest known Curie temperature (T_c) of perovskite manganites, which is a useful feature for device applications. The octahedral oxygen tilt dampens from its maximum value to 0° in 18 unit cells. Above that, the La concentration is reduced to its stoichiometric value, where the tilt and rotation vanishes. Conversely, for LSMO thin films not grown under oxygen deficient conditions, this octahedral oxygen tilt does not dampen and is prevalent throughout the bulk.

4.3 Ultrafast Reflectivity Setup

The ultrafast reflectivity setup is shown in Figure 4.2. The setup consists of a Titanium:sapphire amplifier laser that produces 75 fs pulses centered at 800 nm with a 1 kHz repetition rate at 3.6 mJ per pulse. A half-wave plate (λ/2) in combination with a polarizing beam splitter (PBS) is used to split the laser into pump and probe pulses of variable relative powers. The pump-probe time delay is controlled with a retroreflector on a computer-controlled delay stage. The pump pulse repetition rate is chopped at 500 Hz and focused on the sample surface. The probe pulse is spatially and temporally overlapped with the pump pulse on the sample surface and the reflected probe pulse is

collimated and detected with a photodiode (PD) coupled to a lock-in amplifier. A variable neutral density (ND) filter is used for the power-dependent studies.

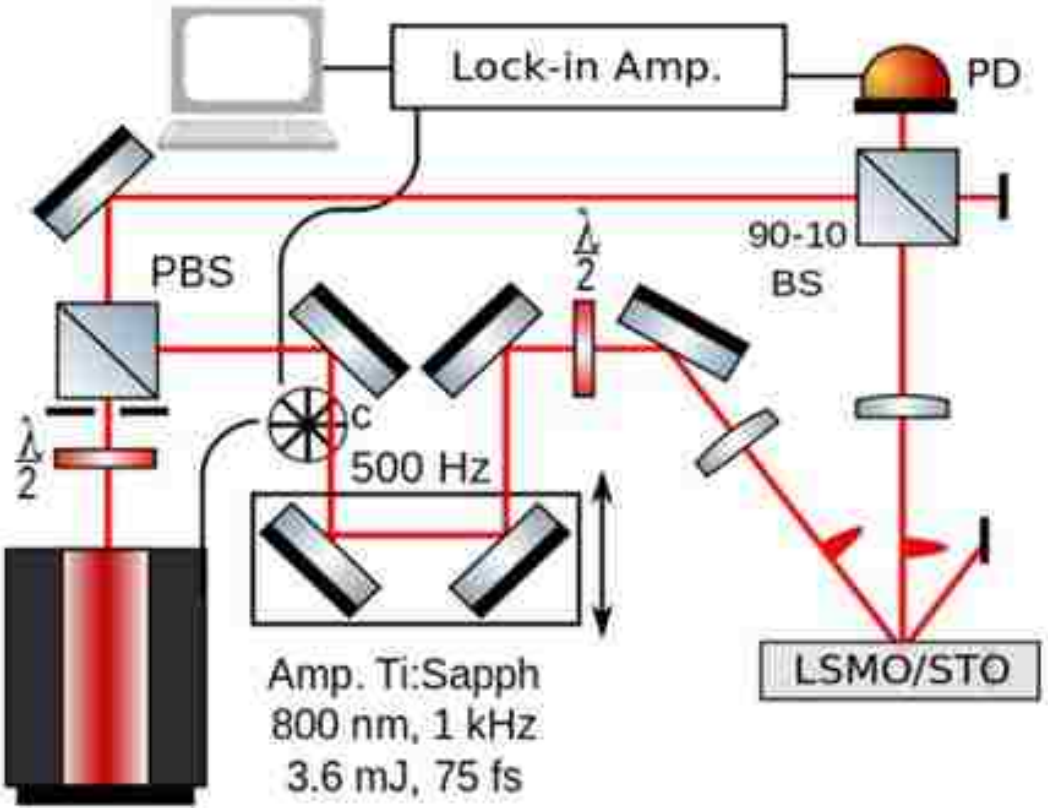

Figure 4.2. Ultrafast reflectivity setup.

4.4 Results and Discussion

The excited-state dynamics using 800 nm pump and probe pulses on a 70 unit cell LSMO/STO sample is investigated under varying pump powers. Previous studies report a broad absorption feature centered at 1.0 eV, which is interpreted as an intersite charge transfer of an electron from the lower energy Jahn-Teller e_g level of a Mn^{3+} ion to the e_g level of a neighboring Mn^{4+} ion as shown in Figure 4.3.[13,14] Additionally, band structure calculations reveal that the 1.55 eV pulse energy correlates with the excited transition of the Mn^{3+} e_g band.[15]

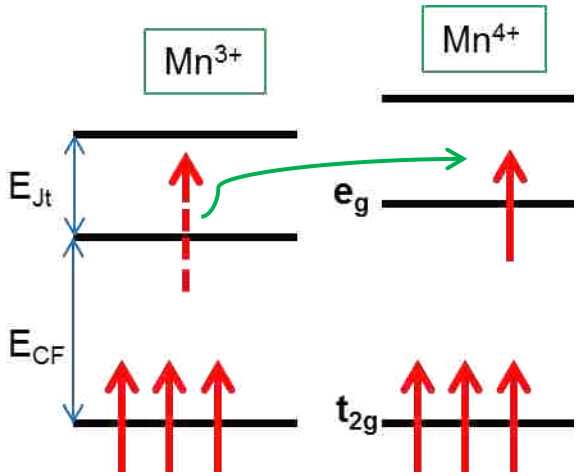

Figure 4.3. Optical transitions of Jahn-Teller e_g levels from Mn^{3+} to Mn^{4+} when using 1.0 eV excitation pulses.

Figure 4.4 (a) shows the time-resolved reflectivity using 40 mW pump and 5 mW probe pulses. Immediately after excitation with the intense pump laser pulse (t=0), the following excited-state relaxation is characterized by a 46.9 $\pm$ 8.2 ps fast lifetime corresponding to electron-phonon coupling and a slower independent phonon-phonon coupling lifetime of 1325 $\pm$ 10 ps, which are obtained by fitting the experimental time-resolved data to a biexponential function. Compared to LSMO studies found in literature, our lifetimes are an order of magnitude longer, indicating the significance of the oxygen-deficient growth conditions and the corresponding changes in the interfacial octahedral tilt on the resulting excited-state relaxation dynamics.[16] Ballistic electron motion and electron-electron decay are processes that occur on a faster timescale than our femtosecond resolution.[17] The measured long-lived phonon-phonon coupling lifetime (>1ns) for the LSMO/STO thin film implies that the phonons are the major energy carrier. This is due to the fact that the prepared LSMO/STO sample is a thin film with no bulk diffusive media to generate heat.[17]

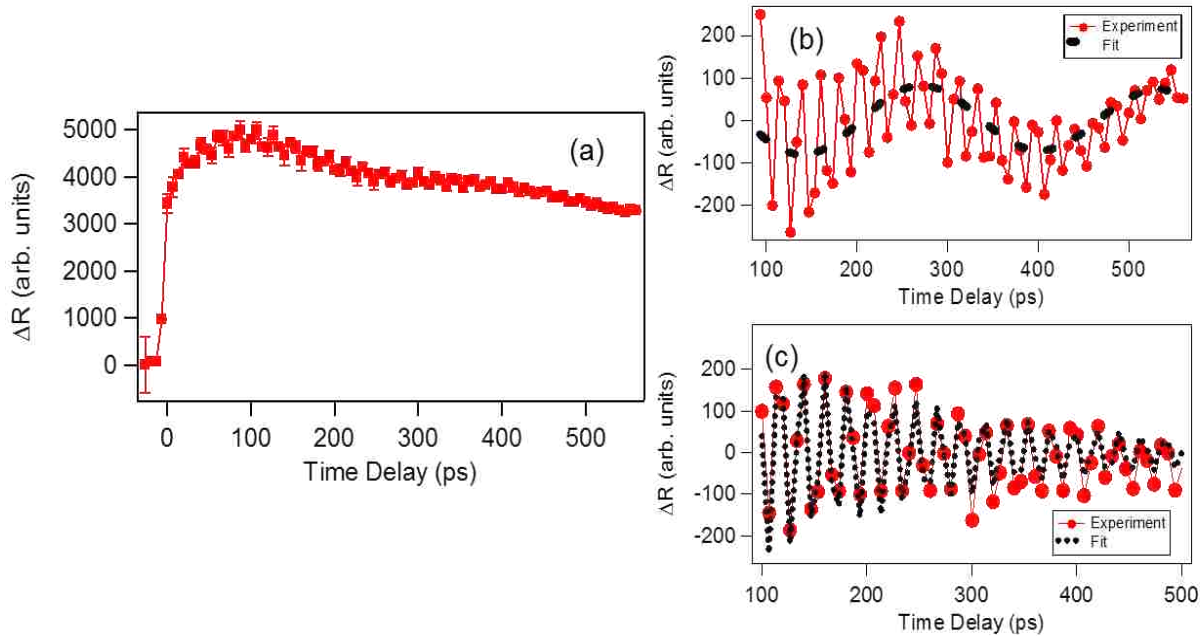

Figure 4.4. (a) Time-resolved reflectivity using 40 mW pump pulses with (b) first biexponential fit subtraction (low energy phonons) and (c) second biexponential fit subtraction (higher energy phonons).

By subtracting the biexponential fit from the obtained data, two residual phonon frequencies can be seen as a fast oscillatory frequency superimposed on a slower frequency as shown in Figures 4.4 (b) and (c). Both oscillatory signals are fit with an exponentially-damping sine function given by

$$R(t) = y_0 + Ae^{\left(-\frac{t}{\tau_d}\right)}\sin(2\pi ft + \varphi) \tag{4.1}$$

where A, τ_d, f, and φ are the oscillatory amplitude, damping time, frequency, and phase, respectively. The lower energy phonons have a period of 261.7 ps and dephase within 1784 $\pm$ 310 ps. The higher energy phonons have a period of 21.2 ps (2 cm^{-1}) and dephase within 285 $\pm$ 35 ps.

The ultrafast reflectivity measurements on the LSMO/STO thin film is repeated under varying pump powers for further characterization of the excited-state relaxation dynamics and associated material properties. Figure 4.5 (a) shows the time-resolved

reflectivity results using 15 mW pump and 5 mW probe pulses. At this lower pump power, the electron-phonon coupling lifetime is observed to be longer (228 $\pm$ 5 ps) while the phonon-phonon coupling lifetime is still on the order of 1 ns (1074 $\pm$ 10 ps). The biexponential subtractions again reveal two oscillatory components where the lower-energy period reduces to 561.8 ps and dephases in 1027 $\pm$ 322 ps while the higher-energy period remains approximately the same at 21.9 ps and dephases in 377 $\pm$ 60 ps.

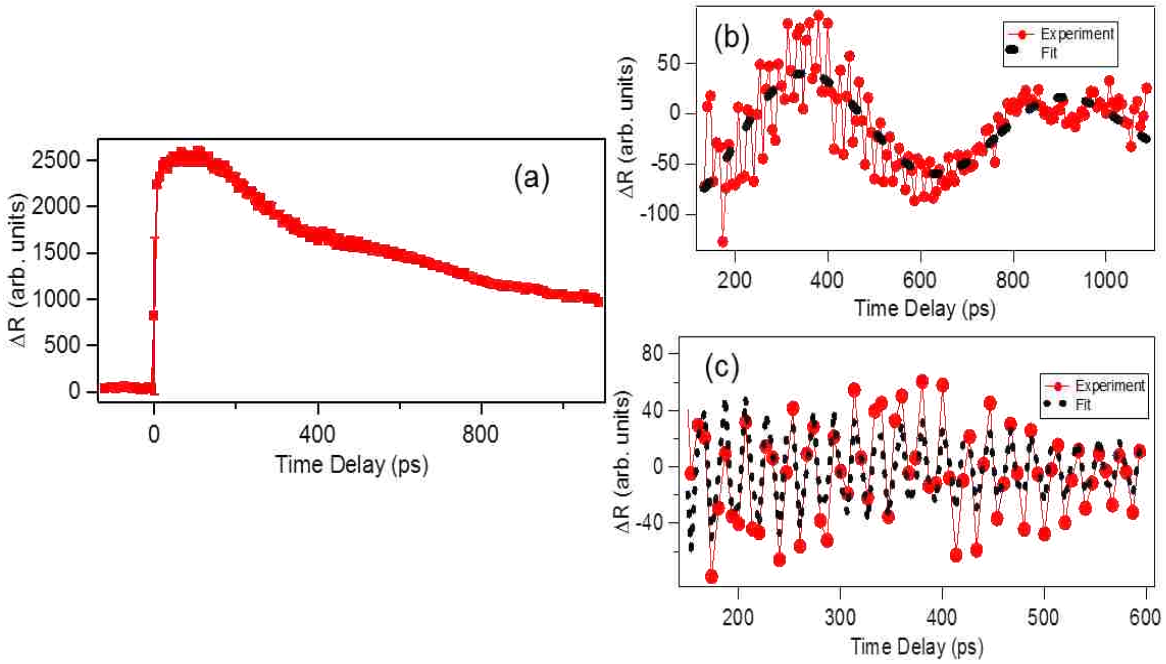

Figure 4.5. (a) Time-resolved reflectivity using 15 mW pump pulses with (b) first biexponential fit subtraction (low energy phonons) and (c) second biexponential fit subtraction (higher energy phonons).

Figure 4.6 shows the time-resolved reflectivity using 10 mW pump and 5 mW probe pulses at 800 nm. The electron-phonon coupling constant is again slightly longer at 314 $\pm$ 6 ps as the power continues to decrease while the phonon-phonon coupling remains on the order of a nanosecond (1300 $\pm$ 9 ps). Both oscillatory periods of high

and low energy phonons remain relatively unchanged at 21.8 ps and 552.5 ps, while the dephasing times of the fast and slow components change to 405 $\pm$ 71 ps

and 1526 $\pm$ 633 ps, respectively.

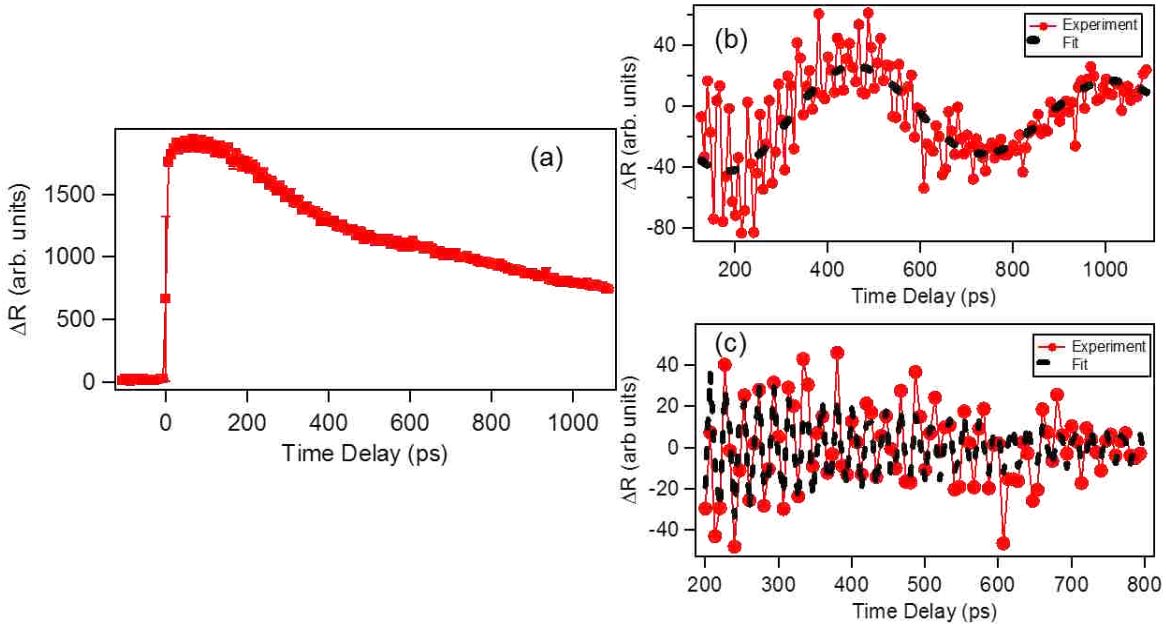

Figure 4.6. (a) Time-resolved reflectivity using 10 mW pump pulses with (b) first biexponential fit subtraction (low energy phonon) and (c) second biexponential fir subtraction (higher energy phonons).

Finally, as shown in Figure 4.7, when the pump power is reduced to 8 mW, the electron-phonon coupling increased to a lifetime of 468 $\pm$ 7 ps while the phonon-phonon coupling lifetime decreased to 972.8 $\pm$ 8.3 ps. In the powers used in these studies, the electron-phonon coupling lifetime is observed to decrease as the pump power increases, with values that vary from 511.6 ps to 46.9 ps as the pump power changed from 8 mW to 40 mW, respectively. Conversely, a lack of power dependent changes in the phonon-phonon coupling lifetime might be further supported by the highly symmetric LSMO crystal. Higher electron temperatures lead to faster electron-phonon coupling; however in this data, the constant phonon-phonon lifetimes indicate a relatively constant phonon or lattice temperatures. In order to fully understand this relationship, a precise

band structure calculation on this particular system is necessary along with additional theoretical and experimental work.

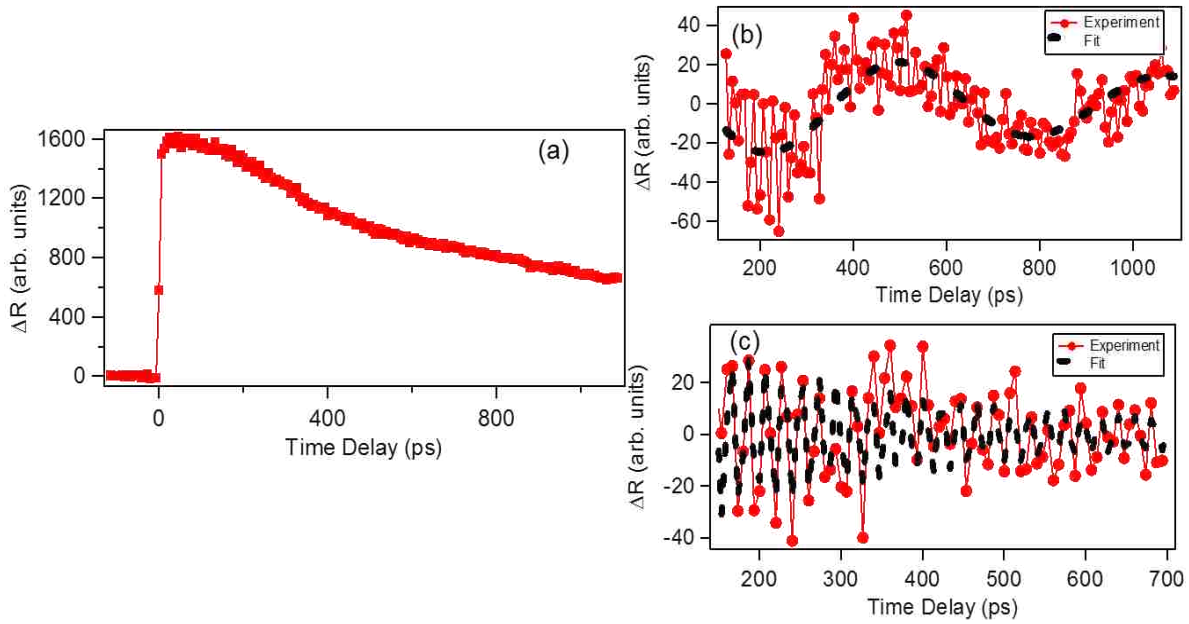

Figure 4.7. (a) Time-resolved reflectivity using 8 mW pump pulses with (b) first biexponential fit subtraction (low energy phonon) and (c) second biexponential fit subtraction (higher energy phonons).

The slow decaying low energy phonon, to the best of our knowledge, has not been observed in the literature for these perovskites. One possible explanation is that the long-range structural modulation of the probe pulse causes interference between the two distinct tilt regions in LSMO. This long-range interaction is consistent with the long-lived lifetimes, stated previously, as a result of the highly ordered LSMO structure. The fast oscillations reveal a frequency of about 46 GHz (0.046 ps^{-1}), likely relevant to other longitudinal acoustic phonon measurements in the literature.[10,12]

The power-dependent lifetimes are shown in Figure 4.8 where τ_{ep} represents the electron-phonon lifetime and $\tau_{d,fast}$ represents the dephasing lifetime of the fast oscillatory phonon. In the powers surveyed in this study, both lifetimes shown in Figure 4.8 decrease as the pump power is increased. These power-dependent lifetimes may

be caused by a two-temperature model where excited electrons have a much higher temperature than the lattice on ultrafast timescales. A table of all lifetimes can be found in Appendix C. Other lifetimes such as the phonon-phonon lifetime and the dephasing lifetime of the slower oscillatory phonon show much lower variation as a function of pump power, suggesting that the lattice temperature heating is not as significant as the electron temperature heating under the pump powers used in these studies, assuming a two-temperature model. Again, more experimental and theoretical work is needed on confirm this interpretation.

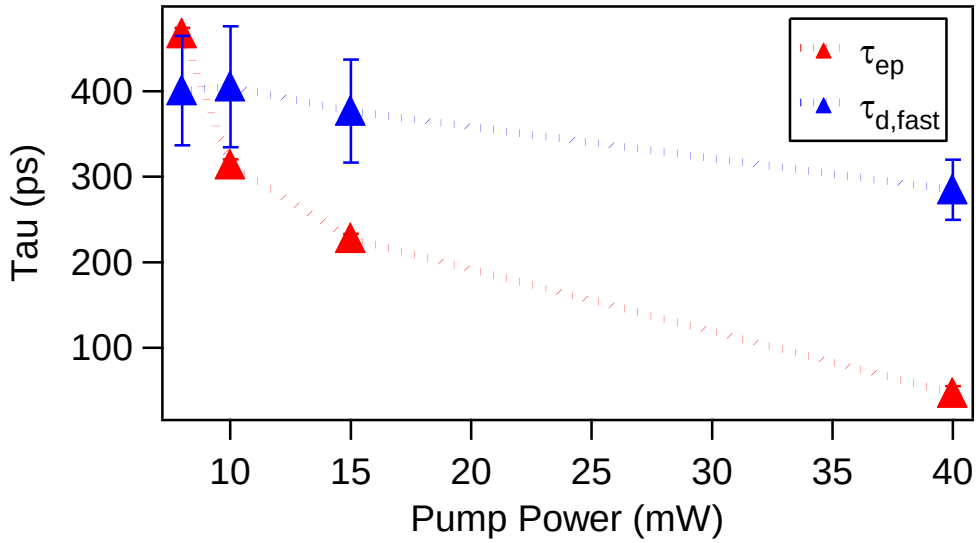

Figure 4.8. Power-dependent lifetimes where τ_1 is the electron-phonon lifetime and τ_d is the fast oscillation dephasing lifetime.

In the prepared LSMO thin film, tilt and non-tilt structures co-exist such that the interactions are different from samples commonly found in the literature. This would suggest the possibility of stronger anharmonic effects, greater structural variation, and more excited-state decay channels. To investigate the mechanisms for the altered ultrafast excited-state dynamics, our group is currently extending these studies in collaboration with Dr. Plummer's research group, to investigate additional experimental

parameters by varying the thin film thickness, doping concentration, and oxygen levels to control the structural disorder. By increasing sample thickness, the low energy phonons, which are attributed to long-range structural modulations, should become less apparent and may vary in frequency. A thickness dependence in the phonon frequency should also verify the acoustic versus optical phonon designation. Furthermore, the effect of A-site doping on the dephasing time will allow us to confirm the vibrational frequencies originating from the octahedra. For more disordered systems, a faster dephasing time is expected from the existence of additional decay channels.

4.5 Conclusion

In summary, we have investigated the ultrafast carrier dynamics of a self-assembled LSMO/STO heterostructure using pump-probe reflectivity. The excited-state dynamics are characterized with a fast electron-phonon coupling lifetime which is observed to decrease as the pump power increases and a slower phonon-phonon coupling lifetime that remains relatively constant near 1 ns under varying pump powers. Additionally, two oscillatory frequencies were observed to be superimposed on the biexponential relaxation and are assigned to a high energy acoustic phonon and a low energy phonon. The dephasing time of the high energy phonons, with a frequency of about 0.046 ps^{-1}, decreases as the pump power is increased. However, the dephasing time of the low energy phonon, with a frequency of about 0.0018 ps^{-1}, remains relatively constant on the order of 1 ns for the range pump powers investigated. In order to fully understand the relationship of the electron-phonon and phonon-phonon lifetimes, additional experiments at higher powers will be done. These results will also be compared a reference LSMO sample using conventional growth conditions, similar to

previous studies in the literature, where there is no octahedral tilt region in the bulk. The investigations of excited-state dynamics play a crucial role in identifying structural and electronic interactions in highly complex systems, providing important insight that can help in developing new potential applications in advanced materials.

4.6 References

(1) Mannhart, J.; Schlom, D. G. Oxide Interfaces—An Opportunity for Electronics. *Science* **2010**, *327*, 1607–1611.

(2) Sun, J. Z.; Abraham, D. W.; Rao, R. A.; Eom, C. B. Thickness-Dependent Magnetotransport in Ultrathin Manganite Films. *Appl. Phys. Lett.* **1999**, *74*, 3017–3019.

(3) Guo, H.; Wang, Z.; Dong, S.; Ghosh, S.; Saghayezhian, M.; Chen, L.; Weng, Y.; Herklotz, A.; Ward, T. Z.; Jin, R.; et al. Interface-Induced Multiferroism by Design in Complex Oxide Superlattices. *Proc. Natl. Acad. Sci. U. S. A.* **2017**, *114*, E5062–E5069.

(4) Yu, P.; Luo, W.; Yi, D.; Zhang, J. X.; Rossell, M. D.; Yang, C.-H.; You, L.; Singh-Bhalla, G.; Yang, S. Y.; He, Q.; et al. Interface Control of Bulk Ferroelectric Polarization. *Proceedings of the National Academy of Sciences* **2012**, *109*, 9710–9715.

(5) Gandolfi, M.; Celardo, G. L.; Borgonovi, F.; Ferrini, G.; Avella, A.; Banfi, F.; Giannetti, C. Emergent Ultrafast Phenomena in Correlated Oxides and Heterostructures. *Phys. Scr.* **2017**, *92*, 034004.

(6) Zhang, J.; Averitt, R. D. Dynamics and Control in Complex Transition Metal Oxides. *Annu. Rev. Mater. Res.* **2014**, *44*, 19–43.

(7) Mansart, B.; Boschetto, D.; Sambri, A.; Malaquias, R.; Miletto Granozio, F.; Scotti di Uccio, U.; Metcalf, P.; Marsi, M. Ultrafast Dynamical Response of Strongly Correlated Oxides: Role of Coherent Optical and Acoustic Oscillations. *J. Mod. Opt.* **2010**, *57*, 959–966.

(8) Saghayezhian, M. Manipulating Physical Properties of Complex Materials By Processing, Louisiana State University (2017).

(9) Vailionis, A.; Boschker, H.; Siemons, W.; Houwman, E. P.; Blank, D. H. A.; Rijnders, G.; Koster, G. Misfit Strain Accommodation in Epitaxial O_3 Perovskites: Lattice Rotations and Lattice Modulations. *Phys. Rev. B Condens. Matter* **2011**, *83*, 064101.

(10) Glazer, A. M. The Classification of Tilted Octahedra in Perovskites. *Acta Crystallogr. B* **1972**, *28*, 3384–3392.

(11) Woodward, P. M. Octahedral Tilting in Perovskites. I. Geometrical Considerations. *Acta Crystallogr. B* **1997**, *53*, 32–43.

(12) Adamo, C.; Ke, X.; Wang, H. Q.; Xin, H. L.; Heeg, T.; Hawley, M. E.; Zander, W.; Schubert, J.; Schiffer, P.; Muller, D. A.; et al. Effect of Biaxial Strain on the Electrical and Magnetic Properties of (001) La0.7Sr0.3MnO3 Thin Films. *Appl. Phys. Lett.* **2009**, *95*, 112504.

(13) Zhao, Y. G.; Li, J. J.; Shreekala, R.; Drew, H. D.; Chen, C. L.; Cao, W. L.; Lee, C. H.; Rajeswari, M.; Ogale, S. B.; Ramesh, R.; et al. Ultrafast Laser Induced Conductive and Resistive Transients in $La_{0.7}Ca_{0.3}MnO_3$: Charge Transfer and Relaxation Dynamics. *Phys. Rev. Lett.* **1998**, *81*, 1310–1313.

(14) Wu, K. H.; Hsu, T. Y.; Shih, H. C.; Chen, Y. J.; Luo, C. W.; Uen, T. M.; Lin, J.-Y.; Juang, J. Y.; Kobayashi, T. Ultrafast Optical Probes of Polaron Dynamics in La0.7Ca0.3MnO3 Thin Films. *J. Appl. Phys.* **2009**, *105*, 043901.

(15) Ma, C.; Yang, Z.; Picozzi, S. Ab Initio Electronic and Magnetic Structure in La0.66Sr0.33MnO3: Strain and Correlation Effects. *J. Phys. Condens. Matter* **2006**, *18*, 7717.

(16) Ren, Y. H.; Trigo, M.; Merlin, R.; Adyam, V.; Li, Q. Generation and Detection of Coherent Longitudinal Acoustic Phonons in the La 0.67 Sr 0.33 Mn O 3 Thin Films by Femtosecond Light Pulses. *Appl. Phys. Lett.* **2007**, *90*, 251918.

(17) Bennemann, K. H. *Non-Linear Optics in Metals*; Clarendon Press, 1998.

Chapter 5. Ultrafast Microscopy and Reflectivity of Laser Heating and Melting Dynamics

5.1 Introduction

Laser additive manufacturing is an efficient, robust, and cost-effective way of creating three-dimensional (3D) materials with high precision. Compared to other additive manufacturing methods, selective laser melting (SLM) is one of the most promising techniques for producing three-dimensional high quality metal and metal alloy objects.[1] In order to better understand and improve SLM for 3D printing of metal and metal alloy objects, the temporal dynamics of laser heating, melting,[2] ablation, and resolidification[3,4] processes need to be investigated on ultrafast timescales in the relevant bulk materials, thin films, powders, and nanomaterials. Studying these SLM processes on sub-picosecond timescales requires a femtosecond laser to produce the high energy densities to induce a phase transition[5] at the metal or metal alloy surface in a pump-probe optical configuration. Structural changes in metal melting processes can occur thermally after laser electronic excitation through lattice vibrational modes,[6] or nonthermally where the lattice destabilizes due to a large population of photoexcited electrons from bonding orbitals.[7] Experimental techniques such as ultrafast pump-probe reflectivity, x-ray diffraction, and x-ray near-edge absorption spectroscopy have shown laser-induced solid-to-liquid phase transitions in metals like aluminum and gold.[8-10] In this chapter, our progress on measuring ultrafast heating and melting dynamics at the surface of different metal, metal alloy, and semiconductor materials is described

We have constructed an ultrafast microscopy setup that utilizes single pump-probe pulse imaging as well as an ultrafast reflectivity optical setup, with preliminary results reported here. The laser melting dynamics in different samples such as metals,

semiconductors, and alloys were investigated with both ultrafast microscopy imaging and reflectivity setups under varying powers and wavelengths. We show preliminary results on germanium excited-state dynamics measured using ultrafast pump-probe reflectivity. We also demonstrate a series of power-dependent ultrafast reflectivity measurements on aluminum thin film samples that are explained in terms of the two-temperature model. This research is continued on single crystal silicon samples, which show that the two-temperature model in laser heating and melting dynamics is generally universal across many different metal and semiconductor materials. Additional studies utilize optical microscopy to investigate ultrafast laser melting of an aluminum alloy substrate using pulse train and single-pulse configurations. Future work will focus on combining the ultrafast reflectivity and microscopy configurations to take pump-probe imaging of laser melting dynamics on ultrafast timescales. Additional conditions such as laser wavelength, pulse width, pulse repetition rate, and different metal alloy nanomaterial samples will be altered and studied for investigating SLM ultrafast processes. Using this combined ultrafast microscopy and reflectivity setup, fundamental physical and material properties can be studied such as photoexcitation, non-equilibrium heating,[2,7] electron-phonon coupling, lattice thermalization,[11] heat flow, melting, and resolidification.[4]

5.2 Ultrafast Reflectivity and Microscopy Setup

The ultrafast setup for microscopy and reflectivity measurements, shown in Figure 5.1, uses a Titanium:sapphire amplifier laser that produces 75 fs pulses centered at 800 nm with either a 1 kHz or 10 kHz repetition rate. A series of optical choppers, synchronized with the amplifier, can be used to reduce the laser repetition rate for

single-pulse selection. The laser is split into pump and probe pulses using a half-wave (λ/2) plate in combination with a polarizing beam splitter. The pump-probe delay time is controlled with a retroreflector on a computer-controlled delay stage. The probe pulse can be kept at 800 nm or frequency-doubled to 400 nm using a nonlinear BBO crystal. The probe pulse is focused and overlapped with the pump pulse, both spatially and temporally, on the sample surface. The probe pulse is reflected from the sample surface, collimated by the plano-convex lens, and split by a beam splitter so that a portion of the reflected beam is detected with a photodiode (PD) and lock-in amplifier for reflectivity measurements while the remaining portion is imaged using a high-sensitivity CCD camera. For single-pulse microscopy measurements, an optomechanical shutter (S) picks a single pulse from a 5 Hz pulse train set by the choppers. A portion of the single pulse is reflected by a beam sampler and detected with a photodiode which serves as a trigger for the CCD. Future work will focus on measuring ultrafast time-resolved laser melting images using pairs of single pump and probe pulses exposed to a fresh sample position controlled by the sample stage. Additionally, by incorporating an optical parametric amplifier (OPA), the pump pulse wavelength can be varied from the infrared to the visible energy range (from 365 to 1300 nm) for investigating wavelength-dependent ultrafast dynamics of SLM processes in metals, metal alloys, and nanomaterials.

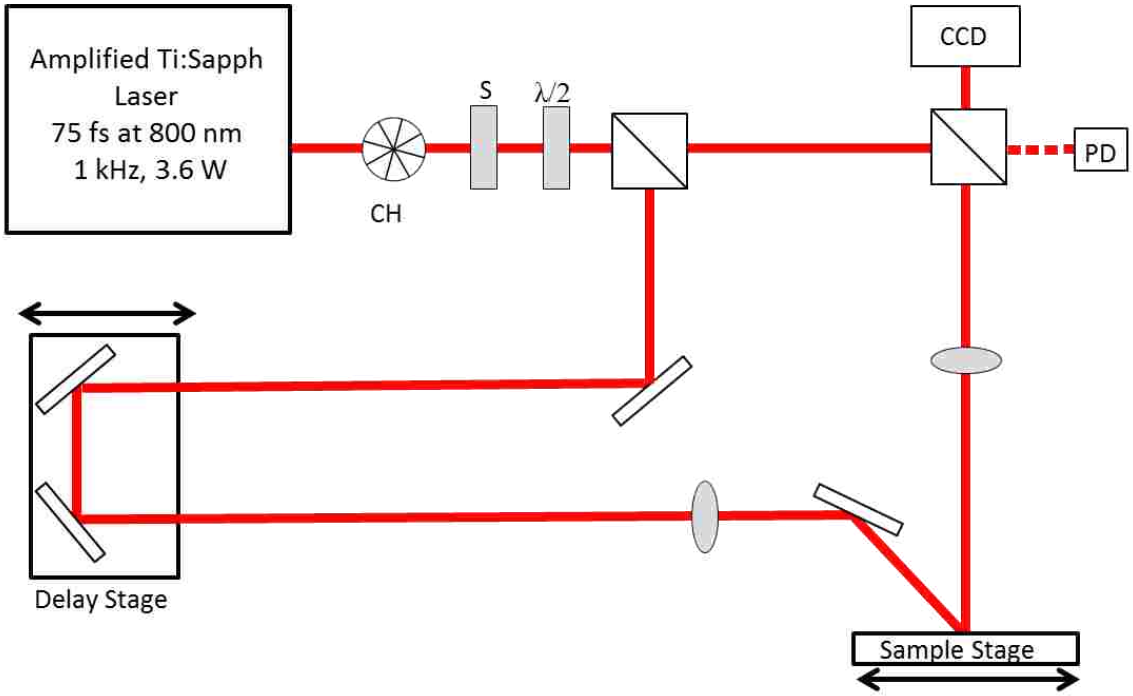

Figure 5.1. Experimental setup for ultrafast reflectivity and microscopy measurements.

5.3 Results

Preliminary pump-probe reflectivity data has been obtained for germanium, aluminum, and silicon surfaces using an intense 800 nm pump pulse and a weak 800 nm or 400 nm probe pulse. Figure 5.2 (a) shows the time-resolved excited-state dynamics of Ge (100) using 14 μJ pump and 4 μJ probe pulses, both at 800 nm. At negative time delays, no change in reflectivity is observed. However, immediately after excitation a sharp decrease in reflectivity is measured. The time-dependent change in reflectivity occurs due to relaxation dynamics of photoexcited carriers from the creation and recombination of electron-hole pairs.[12] The relaxation in Figure 5.2 (a) can be fit with a biexponential function with lifetimes of 11.2 ps and 81.6 ps, corresponding to electron-phonon and phonon-phonon scattering processes.

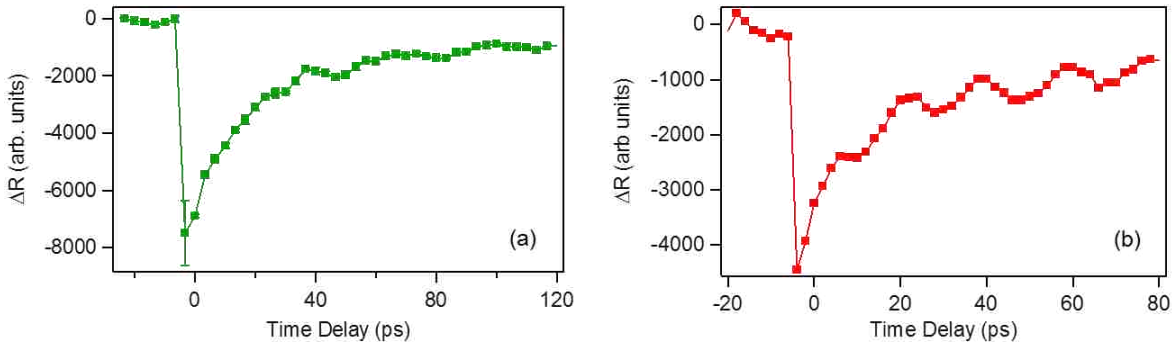

Figure 5.2. Time-resolved reflectivity from Ge with (a) 14 μJ and (b) 7.8 μJ pump pulse powers at 800 nm.

At a lower 800 nm pump power of 7.8 μJ, residual periodic oscillations are observed during the relaxation processes which are attributed to acoustic phonons, as shown in Figure 5.2 (b). Figure 5.3 (a) shows the fit of this biexponential ultrafast relaxation, with lifetimes of 11.2 ps and 106 ps. After subtracting the biexponential fit from the data in Figure 5.3 (a), the resulting oscillations are shown in Figure 5.3 (b). These acoustic phonon oscillations can be fit by an oscillating exponential function with a damping time of 164.6 ps and a frequency of 0.0526 ps^{-1}, also shown in Figure 5.3 (b).

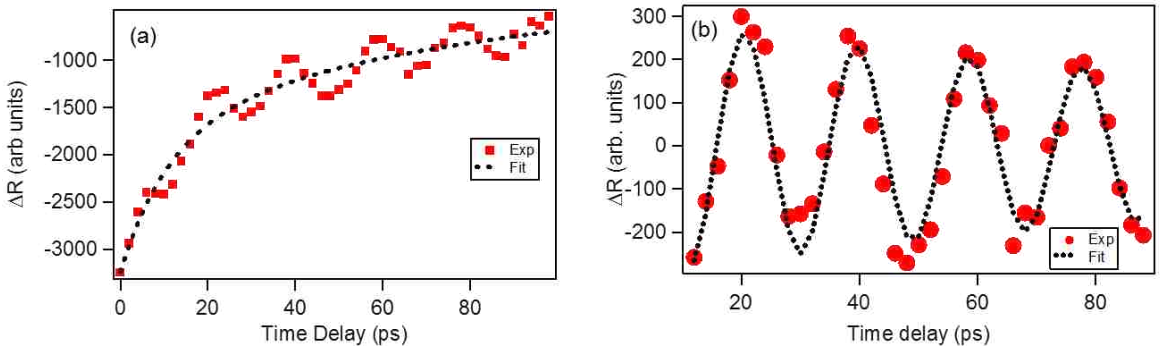

Figure 5.3. (a) Ultrafast relaxation dynamics of Ge (red squares) with 7.8 μJ pump at 800 nm with a biexponential fit (black dotted line). (b) Acoustic phonon oscillations obtained after subtracting biexponential fit (red circles) and fitting with an exponentially decaying sine function (black dotted lines).

When the reflectivity probe wavelength is 400 nm, the Ge excited-state dynamics measured show a much different time profile described by a fast decrease and rise

followed by a slower rise, providing complementary information on the carrier relaxation dynamics. These results are shown in Figure 5.4 where the 800 nm pump power is 11.4 μJ and the 400 nm probe power is 4 μJ per pulse. The fast decrease observed after excitation occurs within 133 fs, which is attributed to electron-electron scattering during carrier thermalization, manifesting as a reduction in reflectance. The exponential rise can be fit to obtain a rise lifetime of 351 fs which is comparable to electron thermalization times in similar materials reported in literature.[13] The detection of this ultrafast process at 400 nm may be due to the material's complex dielectric being more sensitive to 400 nm light as opposed to 800 nm; however, a thorough analysis of the wavelength dependence and power dependence of these lifetimes must be done to verify these results.

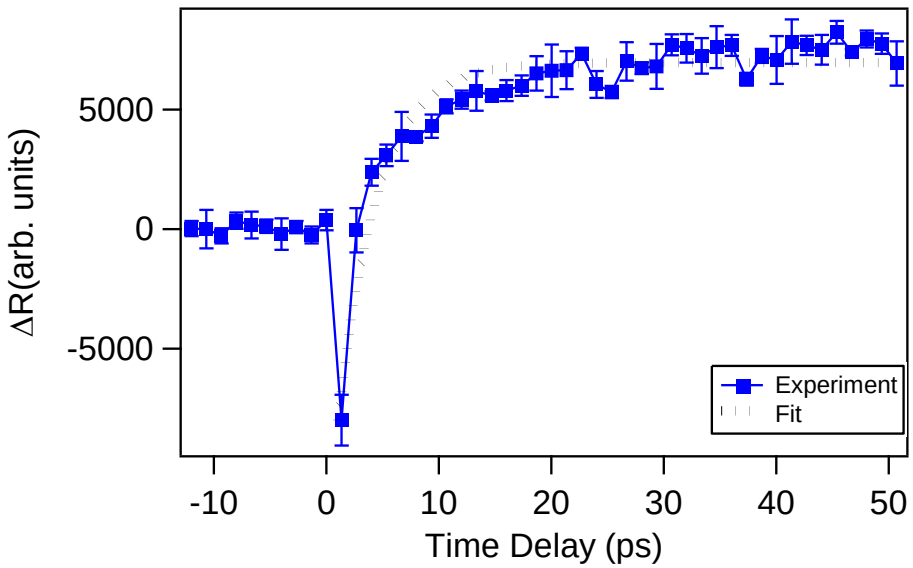

Figure 5.4. Time-resolved reflectivity on Ge using 800 nm pump and 400 nm probe.

More recently, we have investigated the melting dynamics of a 270 nm thick aluminum thin film deposited on a SiO_2 substrate using ultrafast reflectivity. Figure 5.5 shows the power-dependent changes in the ultrafast reflectivity time traces of the aluminum thin film using 800 nm pump and probe pulses. At low powers (<2.0 μJ per

pulse) the temporal change in reflectivity is observed to be a linear step function. This linear behavoir can be explained using the two-temperature model where the electron and lattice temparatures are two distinguishable coupled systems on ultrafast timescales. At low laser fluences the electron temperature is not sufficient to cause significant electron diffusion or coupling to the lattice, and where the linear response is indicitave of straight-forward electronic excitation and heating.[13] The data in Figure 5.5 are fit with a single exponential fucntion given by $\Delta R = A + Be^{(-\frac{t}{\tau})}$, where B is set equal to zero for Figure 5.5 (a) through (d) to resemble the linear step-function response. At higher pump powers of 2.5 and 3.0 μJ, a clear exponential decay is observed, requiring nonzero B values for fittting, which is conistent with the two-temperature model. At these higher laser pump powers, the thermalized electron bath now diffuses and couples to the aluminum crystal lattice via electron-phonon coupling, converting significant heat to the metal lattice, as shown in Figures 5.5 (e) and (f). The electron-phonon coupling lifetime τ increases from 34 ps to 251 ps, and the corresponding amplitude of electron-phonon coupling B also increases in magnitude from 860 to 1505 as the pump power increases from 2.5 to 3.0 μJ, respectively. Finally, at even higher powers (>3.0 μJ), the reflectance drops to a much lower value, indicating an irreversible change in the dielectric constant of the aluminum due to melting.[14] However, even after melting has occurred, as shown in Figures 5.5 (g) and (h), an exponential decay behavoir is still seen, suggesting a reoccurance of heating and melting processes from electron-phonon coupling is ongoing, but to a lesser degree due to sample damage. Under these higher powers above the melting thresold, the electron-phonon coupling lifetime τ decreases from 120 ps to 50 ps, and the electron-phonon coupling amplitude

B decreases compared to pre-melting conditions going to 586 and 609 for pump powers of 3.5 and 4.0 μJ, respectively. The fitting parameters with corresponding errors are tabluated in Appendix D.

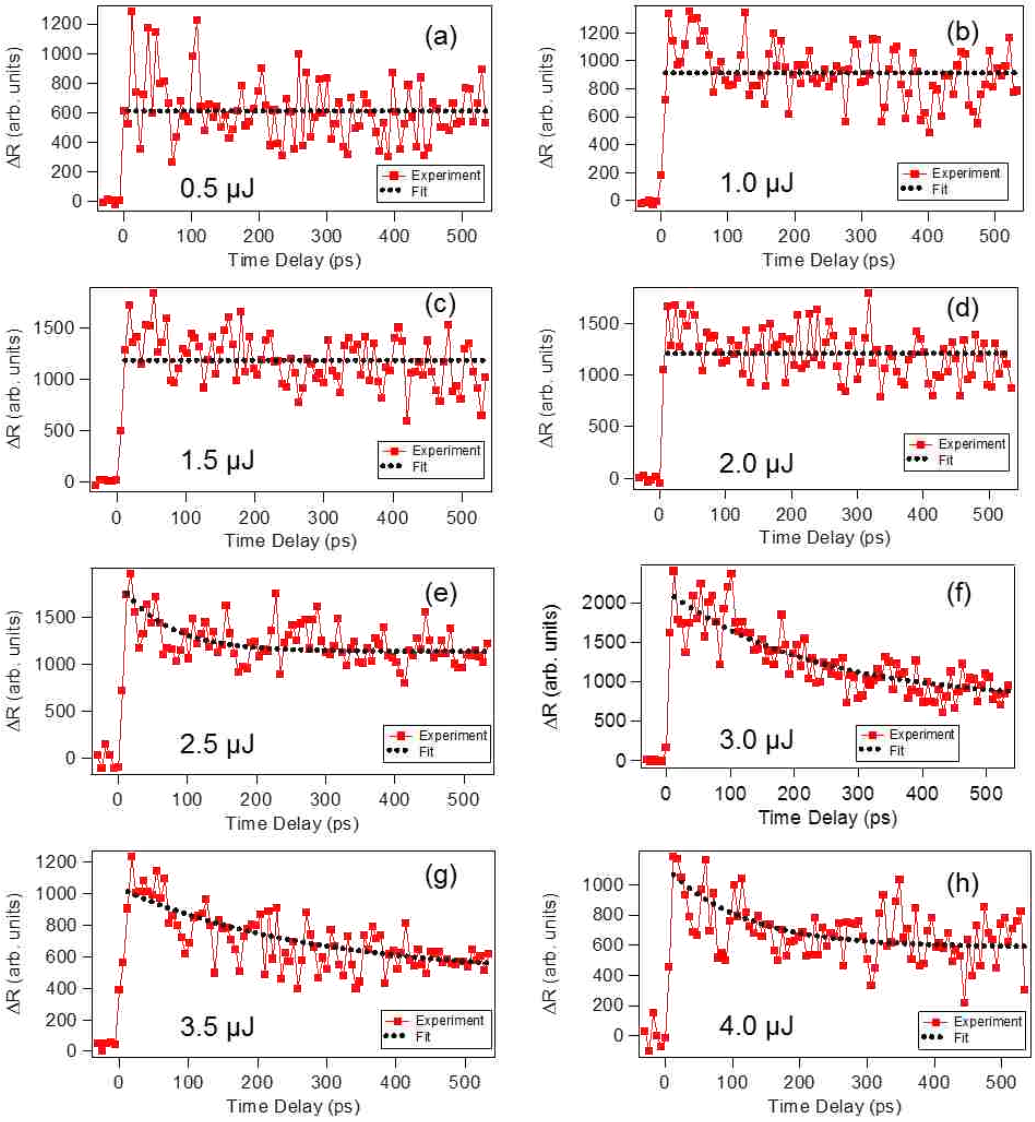

Figure 5.5. Ultrafast reflectivity time traces for Al thin film with 800 nm at (a) 0.5, (b) 1.0, (c) 1.5, (d) 2.0, (e) 2.5, (f) 3.0, (g) 3.5, and (h) 4.0 μJ pump pulse powers, respectively, where melting is observed near 3.5 μJ.

Figure 5.6 shows the reflectivity constants of A and $A + B$ over the powers surveyed in the ultrafast reflectivity measurements on the Al thin film sample. Here, three distinct regions are observed. The first region is the low-power region, which is

described by a linear step function corresponding to electron excitation and heating. The second region corresponds to the onset of significant electron-phonon coupling described by the two-temperature model, where the dynamics are described by an exponential function. Finally, the third region occurs after the observation of melting, where the reflectivity constants decrease dramatically and irreversibly, and the time traces are still described by exponential functions. In the first region, the reflectivity offset magnitude A varies linearly with power, as expected due to a linear increase in electron population density leading to a linear change in the excited-state complex dielectric function of the material. Interestingly, the sum of the reflectivity constants $A + B$ in the second region continues to vary linearly with power on the same approximate slope as in the first region, indicating that the electron density population transfer at time zero continues to follow a linear trajectory as a function of pump power. However, at these higher powers, the increased excited-state electron density undergoes ultrafast high-temperature thermalization according to the two-temperature model where the electrons initially have a much higher temperature than the surrounding lattice, leading to significant electron-phonon coupling and the subsequent heating of the lattice. Finally, after the melting threshold is observed, the original linear slope no longer accurately describes the sum of the reflectivity constants.

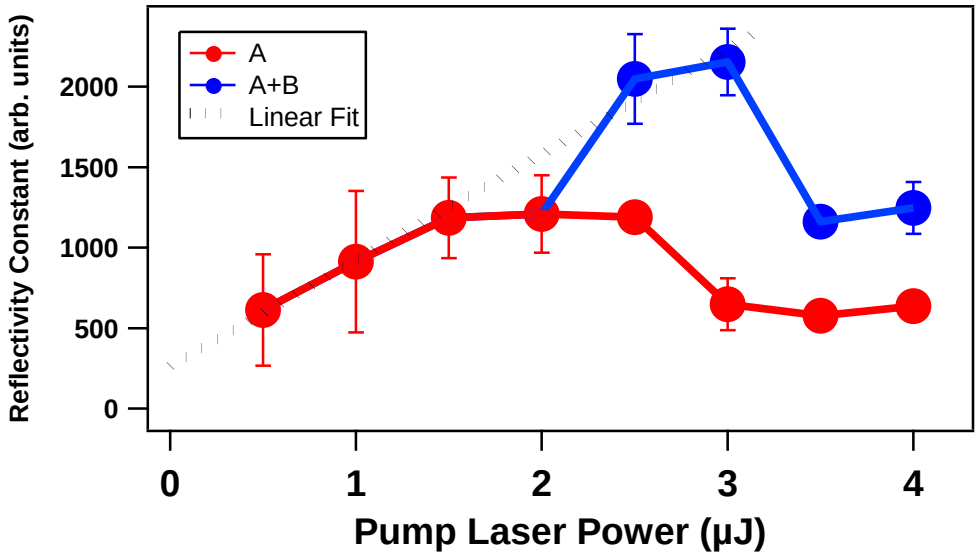

Figure 5.6. Reflectivity constant values as a function of pump power on aluminum where the linear region (dotted line) is shown with fits only including A (red) and with $A + B$ (blue).

This research has also been extended to investigate the heating and melting dynamics of a Si (001) single crystal sample. Figure 5.7 shows the ultrafast changes in reflectivity of silicon under varying of pump powers. In contrast to the aluminum thin film studies, the silicon sample shows a negative change in reflectivity upon 800 nm excitation due to the differences in the excited state versus ground state complex dielectric constants. Similar to the aluminum thin film, at low powers (<4.0 μJ) a linear step-function behavior in the reflectivity is observed and the results are fit using $\Delta R = A + Be^{(-\frac{t}{\tau})}$, where B is set equal zero. As the pump power increases to 4.0 μJ, the thermalized electron bath begins to couple strongly with the colder crystal lattice through electron-phonon coupling and heat transfer, as observed by the exponential decay in Figure 5.7 (c). Finally, at a power of 5.0 μJ, the time-resolved changes in reflectivity decrease due to the irreversible melting of the sample. These results show that the two-temperature model can be applied universally to describe the ultrafast heating and melting dynamics in both metals and semiconductors.

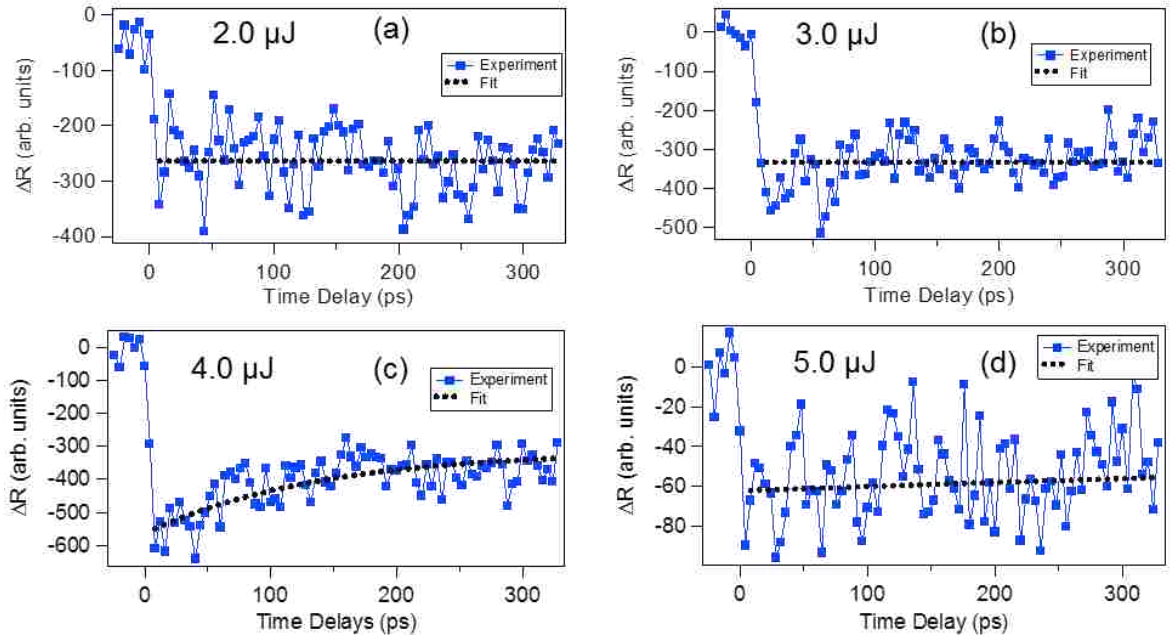

Figure 5.7. Ultrafast reflectivity time traces for Si sample with 800 nm at (a) 2.0, (b) 3.0, (c) 4.0, and (d) 5.0 μJ pump pulse powers, respectively, where melting is observed near 5.0 μJ.

Figure 5.8 shows the power-dependent changes in the reflectivity constants from the ultrafast time-trace fits for the pump powers surveyed for Si (001). These results also describe the onset of electron-phonon coupling and heat transfer at higher pulse pulse powers, followed by the observation of decreased change in reflectivity after irreversible melting occurs. The tabulated values for these fits can be found in Appendix D. More power-dependent data points are needed to determine if the reflectivity constants vary linearly as a function of power up to the onset of irreversible melting. Additionally, it isuseful to point out that the ultrafast dynamics in Al and Si are quite different compared to the Ge and LSMO samples studied previously in this chapter and in Chapter 4. In those samples, the pump pulse is more on resonance with a bandgap excitation causing higher changes in reflectivity and corresponding phonon oscillations. In Si, the bandgap is near 1.1 eV, so the 800 nm (1.55 eV) pump pulse is significantly higher in energy, making the excited electrons behave similarly to metallic electrons,

like in Al which has no bandgap, resulting in thermalization of the lattice phonon modes that is not expected to be coherent in time, so oscillatory reflectivity time traces are not observed to within experimental uncertainty.

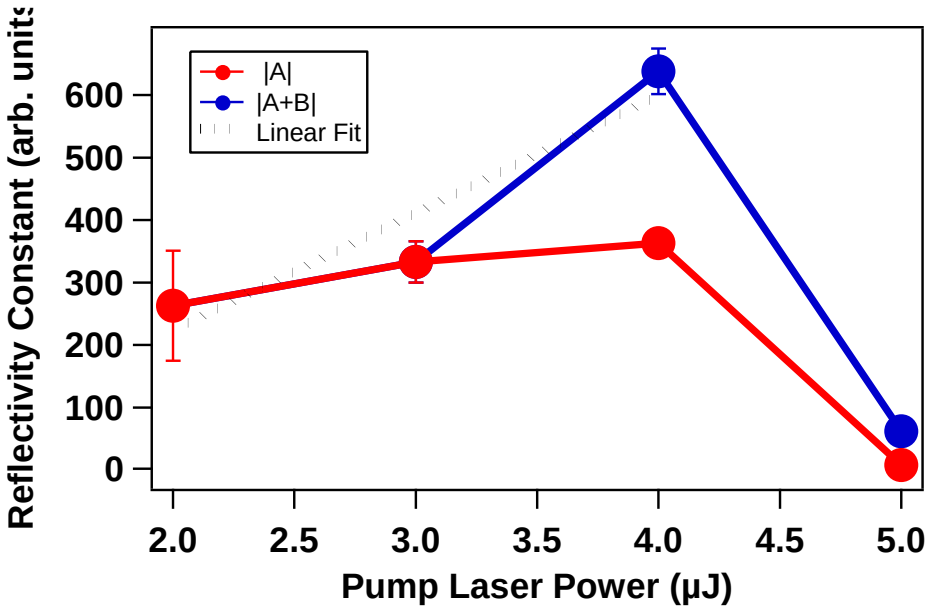

Figure 5.8: Reflectivity constant values as a function of pump power on Si (001) where the linear region (dotted line) is shown with fits only including $|A|$ (red) and with $|A+B|$ (blue).

In order the investigate the spatial morphology of laser-induced melting in metal and metal alloy material, optical microscopy was used in the same setup as in the ultrafast reflectivity experiments. Optical microscopy images of an aluminum alloy substrate after ultrafast laser melting using different powers and pulse properties are shown in Figures 5.9 and 5.10. First, the aluminum sample is exposed to a pulse train of 800 nm femtosecond pulses at a repetition rate of 1 kHz for 200 ms with average laser powers of 0.3 W, 0.5 W, 0.8 W, and 1.4 W, in Figures 5.9 (a)-(d), respectively. These images show clear melting patterns at the laser focus. Next, the laser melting is repeated using single pulses that are created using the optical chopper assembly, with single pulse powers of 0.3 mJ, 0.5 mJ, 0.8 mJ, and 1.4 mJ, shown in Figures 5.10 (a)-

(d), respectively. The single-pulse powers here would correspond to the same average powers shown in Figures 5.9 (a)-(d), respectively. These results demonstrate that single pulse powers are easily sufficient for the metal alloy melting. By combining these results with the conclusions from ultrafast reflectivity measurements, a two-temperature model is predicted to describe these ultrafast heating and melting processes even in a single laser pulse. Future work will incorporate microscopy in an ultrafast pump-probe configuration, using a computer-controlled x-y sample stage to expose fresh sample spots for the laser for each pulse, combined with repeatable time scans for statistical analysis. This will enable fundamental investigations of the ultrafast imaging of selective laser melting of metal and metal alloy materials.

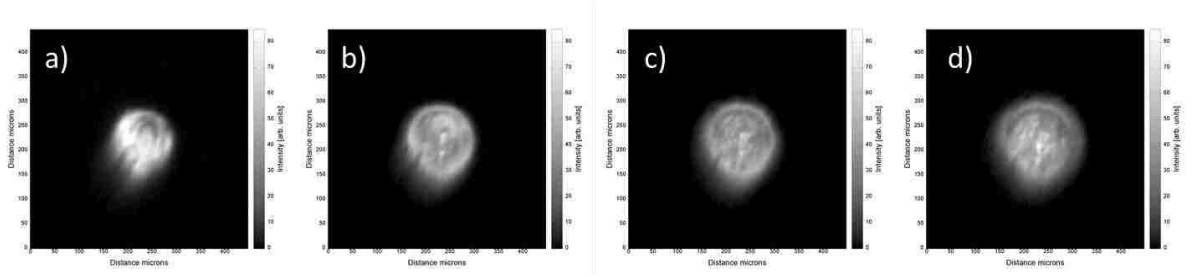

Figure 5.9. Microscopy images of aluminum alloy laser melting using 75 fs 800 nm pulses with a continuous pulse train with average powers of (a) 0.3 W, (b) 0.5 W, (c) 0.8 W, and (d) 1.4 W.

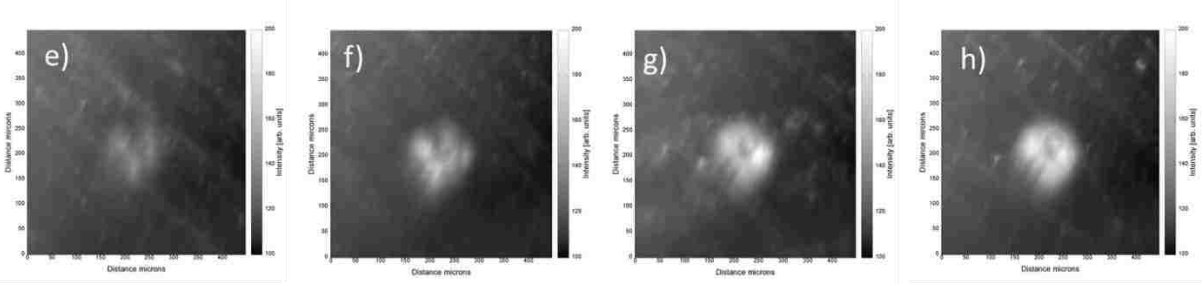

Figure 5.10. Microscopy images of aluminum alloy laser melting using single 75 fs, 800 nm pulses at energies (a) 0.3 mJ, (b) 0.5 mJ, (c) 0.8 mJ, and (d) 1.4 mJ.

In order to characterize the interaction of the laser pulse and the aluminum alloy surface, a spatial profile of a single laser pulse was taken using the optical microscope,

as shown in Figure 5.11. To confirm the intensity profile of the laser, the pulse image is integrated and fit with a Gaussian profile, shown in Figure 5.12. The focal size of the laser pulse is similar in diameter to the melt areas in Figures 5.9 and 5.10, which is a good indication of localized energy deposition of the ultrafast laser pulses.

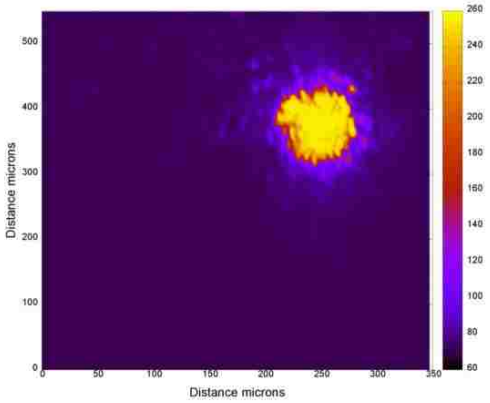

Figure 5.11. Optical microscopy image of a single laser pulse.

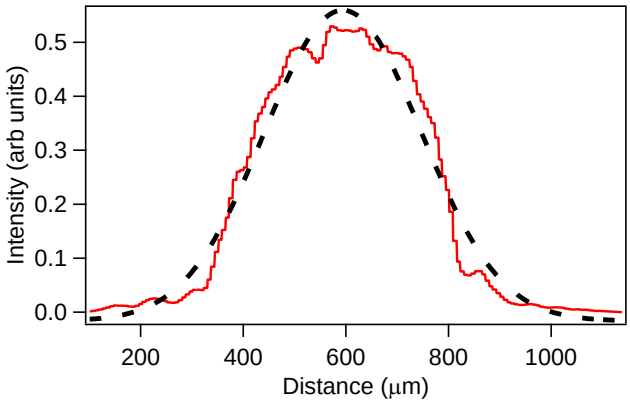

Figure 5.12. Integrated intensity profile fit with a Gaussian function to obtain a focal spot size of 216 μm.

5.4 Conclusion

The ultrafast heating and melting dynamics are presented for different metal, metal alloy, and semiconductor materials. Time-resolved reflectivity measurements for Ge (100) using 800 nm pump and both 800 and 400 nm probe pulses are presented under varying pump powers. Under certain pump powers, excited-state relaxation

dynamics show biexponential decays with overlapping acoustic phonon oscillations. Measuring the ultrafast time-dependent changes in reflectivity for these samples is a fundamental step in ultimately achieving single-pulse time-resolved microscopy for different materials. Additionally, extensive ultrafast reflectivity measurements under varying pump powers are used to characterize the heating and melting dynamics of aluminum thin film and silicon single crystal samples. Both results are in agreement with the two-temperature model where a sufficient power density is required to promote electron diffusion and electron-phonon coupling, leading to irreversible laser melting damage at higher laser powers. We have also shown preliminary optical imaging of ultrafast laser melting of an aluminum alloy substrate, demonstrating that the melting is driven by the high peak intensity of a single laser pulse. Future work will continue the power-dependent ultrafast reflectivity measurements of aluminum thin films under different thicknesses to determine the dependence of the metal film thickness on resulting heating and melting dynamics. Additional work extending these studies to iron and aluminum nanoparticles deposited on substrates will also be investigated to compare melting dynamics on the nanoscale. These fundamental investigations are important for developing a better understanding of laser heating and melting processes in metals, semiconductors, and metal alloys for the purpose of improving selective laser melting in additive manufacturing technologies.

5.5 References

(1) Kruth, J. P.; Froyen, L.; Van Vaerenbergh, J.; Mercelis, P.; Rombouts, M.; Lauwers, B. Selective Laser Melting of Iron-Based Powder. *J. Mater. Process. Technol.* **2004**, *149* (1), 616–622.

(2) Gamaly, E. G. The Physics of Ultra-Short Laser Interaction with Solids at Non-Relativistic Intensities. *Phys. Rep.* **2011**, *508*, 91–243.

(3) Recoules, V.; Clérouin, J.; Zérah, G.; Anglade, P. M.; Mazevet, S. Effect of Intense Laser Irradiation on the Lattice Stability of Semiconductors and Metals. *Phys. Rev. Lett.* **2006**, *96*, 055503.

(4) Lin, Z.; Zhigilei, L. V.; Celli, V. Electron-Phonon Coupling and Electron Heat Capacity of Metals under Conditions of Strong Electron-Phonon Nonequilibrium. *Phys. Rev. B Condens. Matter* **2008**, *77*, 075133.

(5) Sundaram, S. K.; Mazur, E. Inducing and Probing Non-Thermal Transitions in Semiconductors Using Femtosecond Laser Pulses. *Nat. Mater.* **2002**, *1*, 217–224.

(6) Siegal, Y.; Glezer, E. N.; Mazur, E. Dielectric Constant of GaAs during a Subpicosecond Laser-Induced Phase Transition. *Phys. Rev. B Condens. Matter* **1994**, *49*, 16403–16406.

(7) Van Vechten, J. A.; Tsu, R.; Saris, F. W. Nonthermal Pulsed Laser Annealing of Si; Plasma Annealing. *Phys. Lett. A* **1979**, *74*, 422–426.

(8) Kandyla, M.; Shih, T.; Mazur, E. Femtosecond Dynamics of the Laser-Induced Solid-to-Liquid Phase Transition in Aluminum. *Phys. Rev. B Condens. Matter* **2007**, *75*, 214107.

(9) Ernstorfer, R.; Harb, M.; Hebeisen, C. T.; Sciaini, G.; Dartigalongue, T.; Miller, R. J. D. The Formation of Warm Dense Matter: Experimental Evidence for Electronic Bond Hardening in Gold. *Science* **2009**, *323*, 1033–1037.

(10) Leguay, P. M.; Lévy, A.; Chimier, B.; Deneuville, F.; Descamps, D.; Fourment, C.; Goyon, C.; Hulin, S.; Petit, S.; Peyrusse, O.; et al. Ultrafast Short-Range Disordering of Femtosecond-Laser-Heated Warm Dense Aluminum. *Phys. Rev. Lett.* **2013**, *111*, 245004.

(11) Bonse, J.; Bachelier, G.; Siegel, J.; Solis, J. Time- and Space-Resolved Dynamics of Melting, Ablation, and Solidification Phenomena Induced by Femtosecond Laser Pulses in Germanium. *Phys. Rev. B Condens. Matter* **2006**, *74*, 134106.

(12) Zollner, S.; Myers, K. D.; Jensen, K. G.; Dolan, J. M.; Bailey, D. W.; Stanton, C. J. Femtosecond Interband Hole Scattering in Ge Studied by Pump-Probe Reflectivity. *Solid State Commun.* **1997**, *104*, 51–55.

(13) Bennemann, K. H. *Non-Linear Optics in Metals*; Clarendon Press, 1998.

(14) Guo, C.; Rodriguez, G.; Lobad, A.; Taylor, A. J. Structural Phase Transition of Aluminum Induced by Electronic Excitation. *Phys. Rev. Lett.* **2000**, *84* (19), 4493–4496.

Chapter 6. Electronic Sum-Frequency Generation of α-Quartz (0001)

6.1 Introduction

Second-order nonlinear spectroscopic techniques are powerful tools in characterizing and studying surfaces and interfacial chemistry.[1-5] For example, vibrational sum-frequency spectroscopy (VSFS) using infrared and visible pulses has been used to study the oxidation of CO on Pt (111),[6] electrochemistry of adsorbed CO at the liquid-electrode interface,[7] surface phonons of α-quartz (0001),[8] and excited-state dynamics of malachite green at the air-water interface.[9] Sum-frequency generation (SFG) is a nonlinear optical process in which two photons, or optical electric fields (E_1 and E_2), coherently add at a surface or interface to produce a third photon at the sum of their frequencies.[1] The interaction of E_1 and E_2 induce a second-order nonlinear polarization, $P^{(2)}$, which is described by Eq. 6.1, where E_1, E_2, and $\chi^{(2)}$ are the two incident optical electric fields and the second-order nonlinear susceptibility tensor, respectively. The SFG intensity, I_{SFG}, is approximated by $I_{SFG} \sim |P^{(2)}(\omega)|^2$, where

$$P^{(2)} = \chi^{(2)} E_1(\omega_1) E_2(\omega_2) \tag{6.1}$$

The susceptibility tensor $\chi^{(2)}$ can be further expressed in resonant (R) and nonresonant (NR) terms given by

$$\chi^{(2)} = \chi_R^{(2)} + \chi_{NR}^{(2)} = A_{NR} e^{i\varphi_{NR}} + \sum_n \frac{A_n}{\omega_1 - \omega_2 - i\Gamma_n} \tag{6.2}$$

where, A_{NR} is the nonresonant susceptibility amplitude, φ_{NR} is the phase difference between the resonant and nonresonant signal, A_n is the amplitude, and Γ_n is the transition linewidth of the nth mode, respectively. If the incident optical frequencies ω_1 and ω_2 are off resonance with optical transitions of the sample, then the SFG spectrum will be largely dominated by the nonresonant term, producing a signal that correlates

with the incident laser pulse spectra, which are usually Gaussian distributions. If ω_1 or ω_2 are on resonance with one or more electronic or vibrational transitions, the SFG signal will greatly enhanced at those transitions to provide spectral information on the relevant transitions of the sample. It is important to note that both centrosymmetric and noncentrosymmetric systems have resonant and nonresonant SFG signals. For centrosymmetric systems, the SFG will be produced only at the surface, making this a surface-sensitive spectroscopic technique. For noncentrosymmetric systems, the SFG will be produced from both the surface and the bulk, where a large nonresonant contribution arising from the hyperpolarizability of the bulk will often dominate the overall signal. Very few studies have investigated minimizing the bulk contribution of SFG in order to extract, or enhance, surface signals.[9-10] Recently, in collaboration with Dr. Plummer's research group at LSU, we have published a paper that investigates the azimuthal angular dependence of SFG on noncentrosymmetric gallium arsenide (GaAs) where our results show interference between the surface and bulk due to heterodyne amplification.[4] Furthermore, the technique we outline can be extended to surface studies of other noncentrosymmetric crystals that are extensively used in many applications.

In electronic-SFG (ESFG), E_1 and E_2 are both pulses in the visible optical energy range with wavelengths λ_1 and λ_2, respectively, that are spatially and temporally overlapped at a sample to study the electronic resonant and nonresonant optical transitions. ESFG can be used where one incident pulse has a broad energy bandwidth to cover a wide range of molecular or material electronic transitions.[11-13] ESFG is a very new and versatile technique that is being developed by a small number of research

groups. We ultimately would like to develop and study more complex systems and surface chemistries using ESFG. In this experiment, ESFG is used to study the polarization-dependent nonlinear response of α-quartz.

6.2 ESFG Optical Setup

The experimental setup for ESFG is shown in Figure 6.1. A seed pulse generated by a titanium:sapphire oscillator is amplified by a regenerative amplifier to produce 0.7 mJ, 75 fs pulses centered at 800 nm with a pulse repetition rate of 10 kHz. In order to control the relative powers of the two beams corresponding to E_1 and E_2, the amplified pulses pass through a half-wave plate (λ/2) and a polarizing beam splitter (PBS). Approximately 75% of the power passes through the PBS and is focused into a flowing water cell to produce ultrafast pulses of supercontinuum white light. The other 25% of the power is reflected off of the PBS and sent to a computer-controlled delay stage to optimize the temporal overlap of the white light and 800 nm pulses. The femtosecond white light is then filtered through a 600 nm long pass and a 1000 nm short pass filter and polarized through a polarizing beam cube (PBC). Finally, the 800 nm pulse passes through another λ/2 plate in order to control the polarization, then both beams are overlapped spatially and temporally on the sample surface. The reflected ESFG signal is then collimated, polarized using a linear polarizer, and focused into a monochromator coupled to a charged coupled device (CCD). A 530 nm short pass filter is used to block unwanted wavelengths resulting from simple white-light reflection. The quartz sample is mounted on a computer-controlled rotational stage. For each azimuthal angle, 20 ESFG spectra and 20 background spectra (with the incident 800 nm blocked)

are taken in the spectral range of 370-430 nm at acquisition times of 1 second under varying angles and pulse delays.

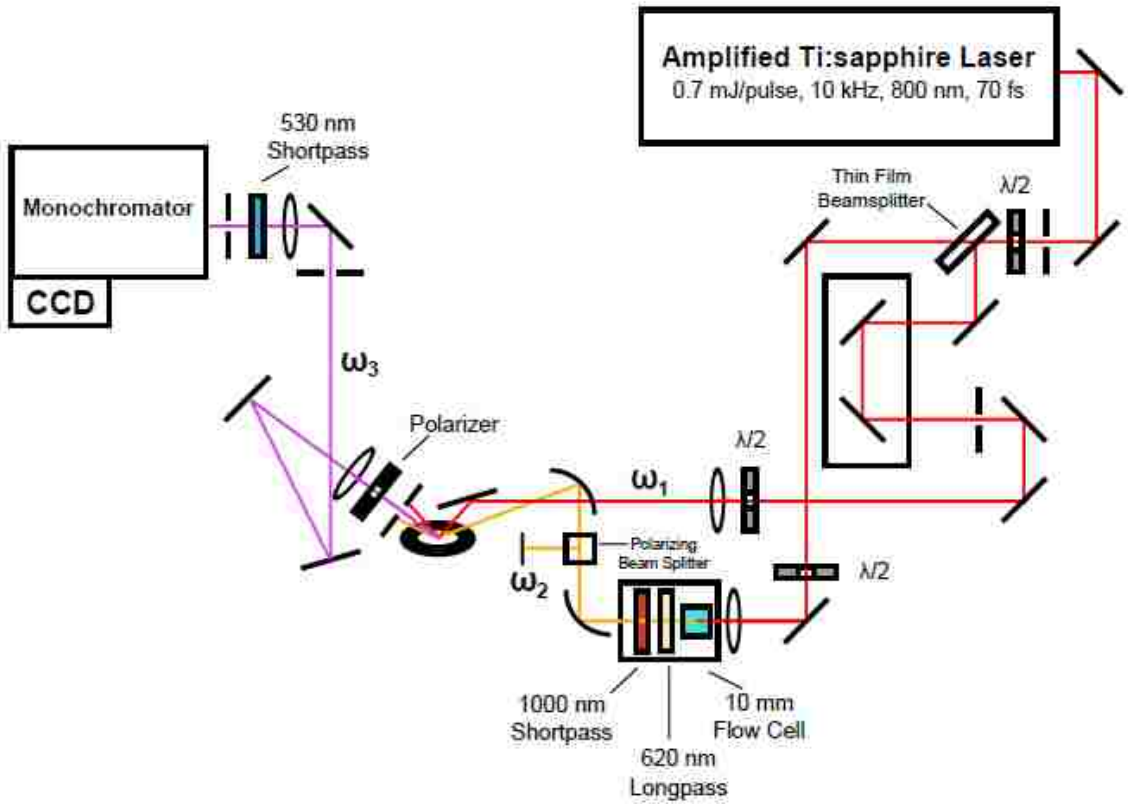

Figure 6.1. Experimental ESFG setup.

6.3 Results

The femtosecond white light pulses are chirped at the sample such that different wavelengths arrive at different temporal times in the pulse duration. By varying the temporal overlap of the 800 nm pulse with the broad visible white light pulses, the steady state ESFG spectrum can cover a broad energy bandwidth, as shown in Figure 6.2. When increasing the path length of the 800 nm pulse, the temporal overlap with the shorter wavelengths in the white light is enhanced. Conversely, by decreasing the path length, the 800 nm pulse enhances the temporal overlap with the longer wavelengths in the white light. By finely tuning the path length we can probe with ESFG wavelengths

ranging from 370-430 nm. The ESFG signal and corresponding ESG spectra also change under varying the azimuthal angular orientation of the α-quartz sample, as shown in Figure 6.2. This demonstrates that our optical setup is very sensitive to the angular-dependent nonlinear response of α-quartz at different optical wavelengths. By combining all this nonlinear optical information together, a very detailed picture of the nonlinear response of α-quartz can be obtained.

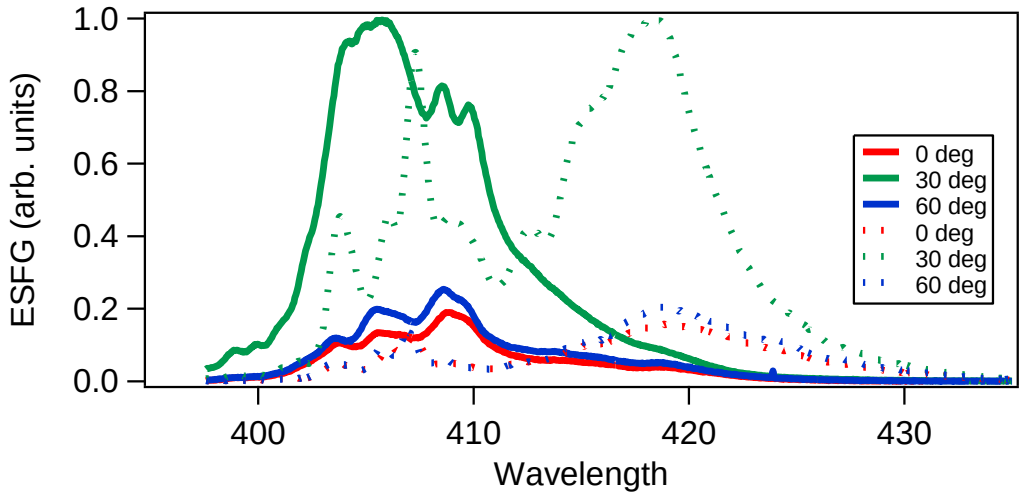

Figure 6.2. Steady-state ESFG spectrum at two different time delays of -0.33 ps (solid spectra) and +0.33 ps (dotted spectra), and as a function of azimuthal crystal angular orientation.

α-Quartz (0001) has a D_3 bulk point-group symmetry[8] with four nonvanishing second-order nonlinear susceptibility tensors given by

$$\chi^{(2)}_{xxx} = -\chi^{(2)}_{xyy} = -\chi^{(2)}_{yxy} = -\chi^{(2)}_{yyx} \quad (6.3a)$$

$$\chi^{(2)}_{xyz} = -\chi^{(2)}_{yxz} \quad (6.3b)$$

$$\chi^{(2)}_{xzy} = -\chi^{(2)}_{yzx} \quad (6.3c)$$

$$\chi^{(2)}_{zxy} = -\chi^{(2)}_{zyx} \quad (6.3d)$$

Here, the subscripts denote the $\chi^{(2)}$ nonlinear response of α-quartz dependent on the polarization of the incident electric fields and the relative crystalline angle in the laboratory framework in Cartesian coordinates. The crystal is oriented parallel to the x-y plane and the crystalline azimuthal axis z is perpendicular to the surface of the crystal

(Figure 6.3). For example $\chi^{(2)}_{xyz}$ denotes a $\chi^{(2)}$ response when E_1 and E_2 are polarized in the x and y direction, respectively, and the induced nonlinear ESFG polarization is in the z direction.

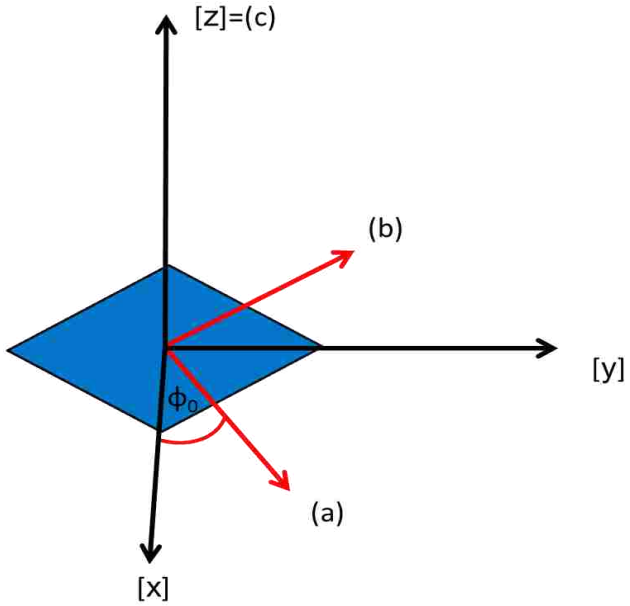

Figure 6.3. Schematic representation of crystalline axis (a, b, and c) in relation to the laboratory frame (x, y and c), where φ_0 is the relative angle of the α-axis away from the x-z plane.

The SSS polarization configuration is first studied, where E_1 and E_2 are s-polarized and the ESFG s-polarized response is measured. For clarity, and SPS polarization configuration, for example, denotes incident fields E_1 p-polarized and E_2 s-polarized with the ESFG s-polarized response measured. The plane of incidence in the x-z plane is defined such that an s-polarized pulse is perpendicular and a p-polarized pulse is parallel to the plane of incidence. The theoretical azimuthal angular dependence on ESFG for α-quartz in the SSS scheme is expected to be given by

$$I_{ESFG} = \left| \frac{L_{yy}(\omega_{ESFG}) L_{yy}(\omega_{800nm}) L_{yy}(\omega_{VIS}) \chi^{(2)}_{yyy} \sin(3\varphi)}{\Delta k} \right|^2 \quad (6.4)$$

$$L_{yy}(\omega_n) = \frac{2k_{0z}(\omega_n)}{k_{0z}(\omega_n) + k_z(\omega_n)} \quad (6.5)$$

where $L_{yy}(\omega)$ is the Fresnel transmission coefficient at frequency ω and Δk is the wave vector mismatch of ESFG. The Fresnel coefficients can be calculated by Eq. 6.5 where k_0 is the wave vector in air. Due to the fact that we are spectrally below the α-quartz bandgap (off resonance), $\chi^{(2)}_{yyy} = \chi_{yyy}{}^{(2)}_{NR}$. Based on Eq. 6.4, the ESFG response in the SSS polarization scheme is expected to have a $|\sin 3\varphi|^2$ dependence, where φ is the azimuthal angle. Therefore, as the crystal rotates 360° (or 2π radians) about the z-axis we would expect 6 minima and 6 maxima corresponding to an $|\sin 3\varphi|^2$ intensity distribution.

The experimental azimuthal angular distribution of I_{ESFG} from α-quartz (0001) in the SSS polarization configuration is shown in Figure 6.4. The results clearly demonstrate a general $|\sin 3\varphi|^2$ angular distribution over 180^0. However, although Eq. 6.4 predicts that I_{ESFG} should be zero at angles 0^0, 60^0, 120^0, and 180^0, the data shows small residual signals at these angles. The deviation from theory at these angles could be explained by the birefringence of the α-quartz causing slight rotations in the polarizations of the incident and ESFG signals occurring in the bulk. The experimental data for SSS can be fit to a simple sine function given by

$$I_{ESFG} \propto |A + B \sin f\varphi|^2 \tag{6.6}$$

where A is an offset value and $B = L_{yy}(\omega_{ESFG})L_{yy}(\omega_{800nm})L_{yy}(\omega_{VIS})\chi^{(2)}_{yyy}$. The fit for the resulting SSS distribution is shown in Figure 6.4. Currently, this project is at the preliminary and exploratory stage. Additional work to be done includes calculating the Fresnel coefficients and incorporating birefringence into the ESFG polarization-dependent models to account for the possibility of interference and polarization rotation in the bulk.

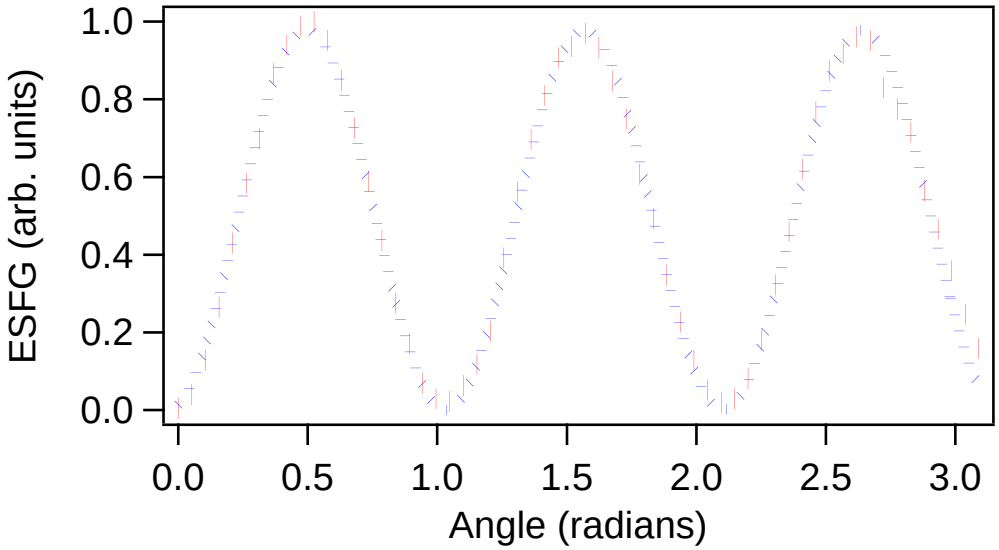

Figure 6.4. Azimuthal angular distribution of ESFG for SSS (red dots) and fit (blue dashed line) using Eq. 6.6 for where A=0.12±0.01, B=0.98±0.01, and f=2.89±0.01.

Additional work is being planned to extend these studies to other incident and outgoing polarization configurations in order to demonstrate a full understanding of the polarization-dependent and angular-dependent nonlinear response of α-quartz. Figure 6.5 shows the preliminary angular distributions of I_{ESFG} for the PSS and PPS polarizations. In order to qualitatively compare the relative $\chi^{(2)}$ values, the angular distributions of I_{ESFG} are plotted normalized to the PSS maximum intensity. This qualitative information shows that $\chi^{(2)}$ response for PSS and PPS are roughly an order of magnitude larger than the $\chi^{(2)}$ response for the SSS polarization configuration. Additionally, the maxima of the ESFG peaks for the PSS and PPS polarizations are approximately $\pi/2$ and 0 radians offset from the SSS peaks, respectively. This information is valuable in describing the second-order nonlinear response of α-quartz at different polarizations. It is clear from the experimental data that our ESFG optical setup is sensitive to changes in polarization and crystalline angle which are due to the structure of α-quartz. Future work will continue to investigate α-quartz and other

samples under varying azimuthal angle, optical wavelength, and polarization configuration.

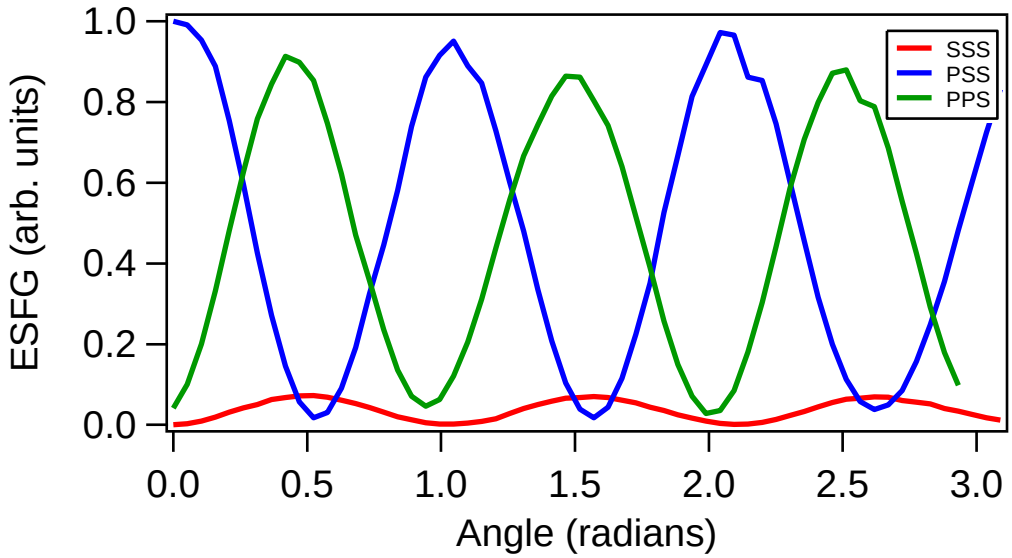

Figure 6.5. Angular distribution of I_{ESFG} as a function of azimuthal angle over 180^0 for SSS (red), PSS (blue), and PPS (green) polarization configurations.

6.4 Conclusion

The azimuthal angular-dependent electronic sum-frequency generation is measured on α-quartz (0001) and the results are compared to theory derived from the trigonal point-group symmetry (D_3). The ability to tune the broad probing energy bandwidth of ESFG by simply changing the temporal overlap of the two pulses is also shown. Our experimental data over 180^0 in the SSS polarization scheme shows a general $|\sin 3\varphi|^2$ dependence in accordance with the theory. In order to explore the relative $\chi^{(2)}$ contributions at different polarizations, the angular distribution of the ESFG signal is measured for the SSS, PSS, and PPS polarization configurations normalized to the maximum intensity under PPS. The results show that $\chi^{(2)}$ for PPS is roughly an order of magnitude larger than the $\chi^{(2)}$ for SSS. This is an important initial step for

developing future ESFG investigations on centrosymmetric and non-centrosymmetric crystals and nanomaterials.

6.5 References

(1) Shen, Y. R. Surface Properties Probed by Second-Harmonic and Sum-Frequency Generation. *Nature* **1989**, *337*, 519.

(2) Shen, Y. R. Optical Second Harmonic Generation at Interfaces. *Annu. Rev. Phys. Chem.* **1989**, *40*, 327–350.

(3) Vidal, F.; Tadjeddine, A. Sum-Frequency Generation Spectroscopy of Interfaces. *Rep. Prog. Phys.* **2005**, *68*, 1095.

(4) Zhang, Z.; Kim, J.; Khoury, R.; Saghayezhian, M.; Haber, L. H.; Plummer, E. W. Surface Sum Frequency Generation Spectroscopy on Non-Centrosymmetric Crystal GaAs (001). *Surf. Sci.* **2017**, *664*, 21–28.

(5) Arnolds, H.; Bonn, M. Ultrafast Surface Vibrational Dynamics. *Surf. Sci. Rep.* **2010**, *65*, 45–66.

(6) Su, X.; Cremer, P. S.; Shen, Y. R.; Somorjai, G. A. High-Pressure CO Oxidation on Pt (111) Monitored with Infrared- Visible Sum Frequency Generation (SFG). *J. Am. Chem. Soc.* **1997**, *119*, 3994–4000.

(7) Baldelli, S. Probing Electric Fields at the Ionic Liquid- Electrode Interface Using Sum Frequency Generation Spectroscopy and Electrochemistry. *J. Phys. Chem. B* **2005**, *109*, 13049–13051.

(8) Liu, W.-T.; Shen, Y. R. Surface Vibrational Modes of Alpha-quartz(0001) Probed by Sum-Frequency Spectroscopy. *Phys. Rev. Lett.* **2008**, *101*, 016101.

(9) Ostroverkhov, V.; Waychunas, G. A.; Shen, Y. R. Vibrational Spectra of Water at Water/α-Quartz (0001) Interface. *Chem. Phys. Lett.* **2004**, *386*, 144–148.

(10) Ostroverkhov, V.; Waychunas, G. A.; Shen, Y. R. New Information on Water Interfacial Structure Revealed by Phase-Sensitive Surface Spectroscopy. *Phys. Rev. Lett.* **2005**, *94*, 046102

(11) Sen, P.; Yamaguchi, S.; Tahara, T. Ultrafast Dynamics of Malachite Green at the Air/ Water Interface Studied by Femtosecond Time-Resolved Electronic Sum Frequency Generation (TR-ESFG): An Indicator for Local Viscosity. *Faraday Discuss.* **2010**, *145*, 411–428.

(12) Yamaguchi, S.; Tahara, T. Heterodyne-Detected Electronic Sum Frequency Generation: “Up” versus “down” Alignment of Interfacial Molecules. *J. Chem. Phys.* **2008**, *129*, 101102.

(13) Belkin, M. A.; Han, S. H.; Wei, X.; Shen, Y. R. Sum-Frequency Generation in Chiral Liquids near Electronic Resonance. *Phys. Rev. Lett.* **2001**, *87*, 113001.

.

Appendix A. TiO_2-Au Nanoparticle Size and Morphology Analysis

A.1 Additional TEM Images of TiO_2-Au Nanocomposites

Figure A.1 shows representative TEM images of the 9.9 ± 0.4 nm TiO_2 nanoparticles. The TiO_2 nanoparticles have a significantly lower contrast under TEM compared to gold nanoparticles. The contrast of the TEM images of the TiO_2 nanoparticles is darkened for clarity. The TEM images are taken using a JOEL 100CX microscope with carbon-coated copper grids. Figures A.2, A.3, and A.4 show representative TEM images of the 1:1, 1:2, and 1:3 TiO_2-Au nanocomposites, respectively. Figure A.5 shows the histograms of the size distributions of the (a) TiO_2 nanoparticles, as well as the (b) 1:1, (c) 1:2, and (d) 1:3 [TiO_2]:[Au] nanocomposite samples, respectively. The experimental results of the histograms are fit to log-normal functions, as shown with the dotted black lines. The histograms show that the TiO_2 nanoparticles and the 1:1, 1:2, and 1:3 [TiO_2]:[Au] nanocomposite samples all have size distributions that are clearly distinguishable.

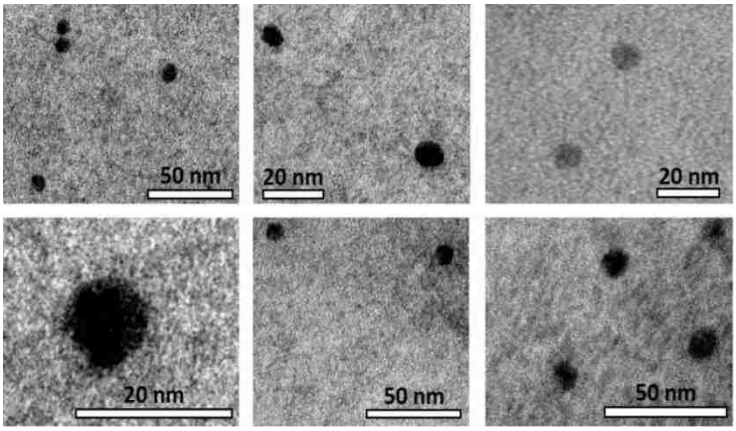

Figure A.1. Transmission electron microscopy images of 9.9 nm ± 0.4 nm TiO_2 nanoparticles sample.

Reprinted from Karam, T. E.; Khoury, R. A.; Haber, L. H., *J. Chem. Phys.* 144, 124704, 2016. With the permission of AIP Publishing.

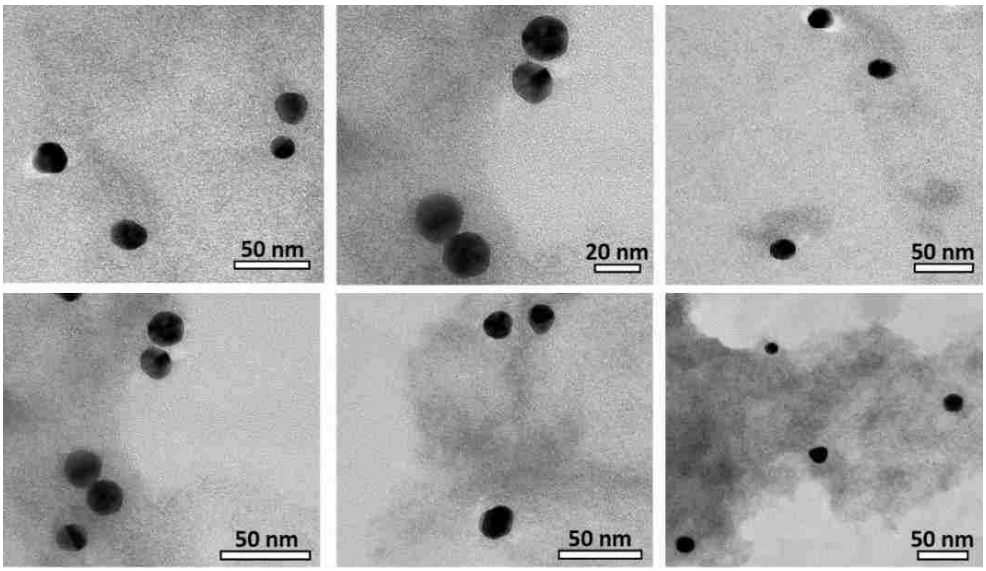

Figure A.2. Transmission electron microscopy images of the 1:1 TiO_2-Au nanocomposites sample.

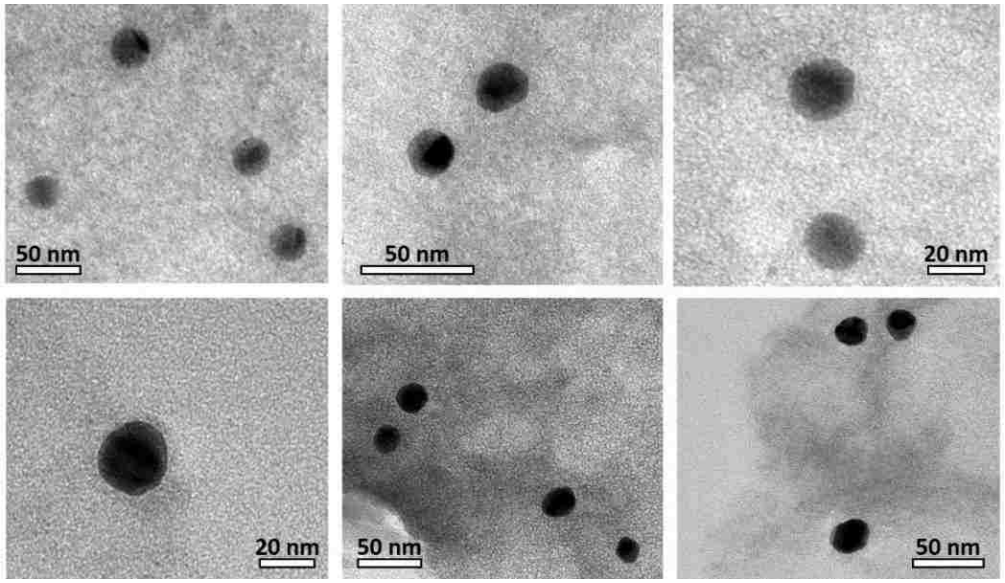

Figure A.3. Transmission electron microscopy images of the 1:2 TiO_2-Au nanocomposites sample.

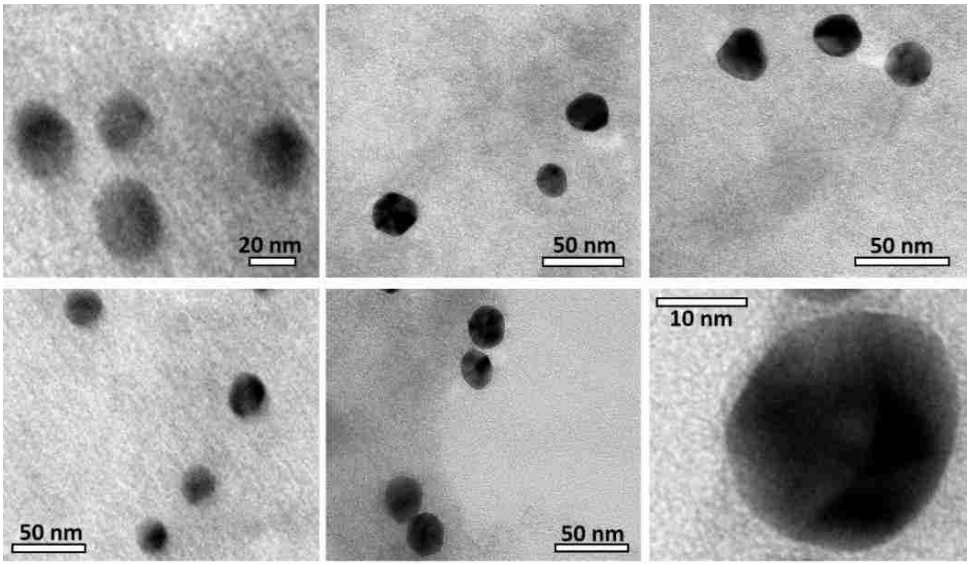

Figure A.4. Transmission electron microscopy images of the 1:3 TiO_2-Au nanocomposites sample.

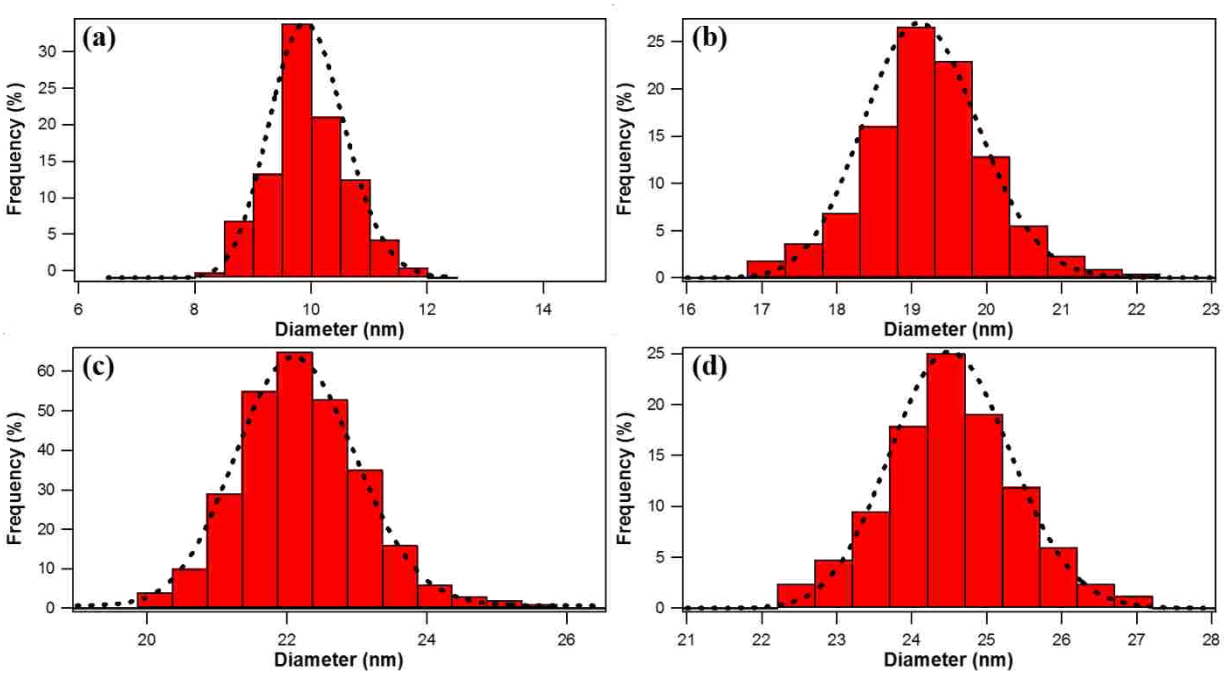

Figure A.5. Histograms representing the size distributions of the (a) TiO_2 nanoparticles, as well as the (b) 1:1, (c) 1:2, and (d) 1:3 [TiO_2]:[Au] nanocomposite samples. The experimental results are fit to log-normal functions, shown by black doted lines.

The errors in the measured nanoparticle sizes are determined from the standard deviations after surveying more than 400 nanoparticles. The size of the gold nanocluster shell surrounding the TiO_2 nanoparticle core is obtained from the increase

of the overall nanoparticle size. Table S4 lists the nanocluster shell sizes s determined by the TEM measurements given by the radius increase with $s = r_{TiO_2-Au} - r_{TiO_2}$ where r_{TiO_2-Au} is the average nanocomposite radius and r_{TiO_2} is the average radius of the TiO_2 nanoparticles. The errors in the sizes of the gold nanocluster shell surrounding the TiO_2 nanoparticle core are determined by error propagation from the standard deviations of the sizes of the TiO_2 nanoparticles and the TiO_2-Au nanocomposites.

A.2 Au Nanocluster Morphology by Phonon Frequency Analysis

The acoustic phonon oscillation frequencies from the different TiO_2-Au nanocomposites are compared to three different size-dependent models that are based on individual gold nanospheres, individual gold nanorods, and core-shell nanoparticles in order to assess the most likely description of the nanocomposite architecture. In the first model, the gold nanoclusters are assumed to form individual spheres tangentially adsorbed at the TiO_2 nanoparticle surface. In this case, the theoretical sizes of the gold nanospheres can be calculated from the experimental values of the phonon oscillation frequencies using the solution of the Navier equation given by $\omega_0 = Re\xi_0 v_L^s / r$, where v_L^s is the longitudinal sound velocity of the nanosphere, r is the radius of nanosphere, and ξ_0 is the normalized frequency of the radial mode.[1] This model has been successfully applied to free metallic nanospheres in water and embedded in glass.[1, 2] The theoretically predicted gold nanocluster radii calculated from the experimental values of the oscillation frequencies using this model are shown in Table A.1 for v_L^s = 3240 m/s and ξ_0 = 2.944 for the values for free gold nanospheres.[1] However, the radii of the nanoclusters calculated from this model are larger by almost a factor of two compared to the sizes obtained from the TEM measurements, assuming this architecture. This

suggests that the gold nanoclusters on the TiO_2 surface are not perfect spheres tangentially attached to the surface. In the second model of the acoustic phonon analysis, gold nanoclusters at the TiO_2 nanoparticle surface are assumed to have rod-like shapes. In this case, the lengths of the rods are calculated using an equation given by[2,3] $T = 2L/\sqrt{E/\rho}$, where E is the Young's modulus and ρ is the density. The calculated values of the gold rod lengths L determined from the experimental values of the oscillation periods T are shown in Table A.1 for $E = 42$ GPa and $\rho = 19.7$ g/cm^3. These values deviate from the sizes determined by the TEM measurements for the three TiO_2-Au samples, so the nanoclusters are not well described using the nanorod model. In the final model of analysis, the TiO_2-Au nanocomposites are assumed to have a core-shell architecture. In this case, the theoretical sizes of the gold nanoshells are calculated from the experimental values of the phonon oscillation frequencies using a model derived from the Helmholtz equation.[4] Here, the equation of the size-dependent oscillation frequency is given by $\omega_0 = \frac{2v_L^S\beta_S}{R_2}(3 - 4\beta_S^2)^{1/2}$, where R_2 is the sum of the core radius and the shell width, and β_S is given by v_T^S/v_L^S, where v_L^S and v_T^S are the longitudinal and transverse sound velocities in the gold shell, respectively, according to the heavy shell approximation. The calculated values of the shell widths w are shown in Table A.1 using the experimentally measured phonon frequencies with v_L^s and v_T^s equal to 3240 m/s and 1200 m/s, respectively. The shell width w equals $R_2 - R_1$, where R_1 is the core radius. The calculated values of w are larger than the experimental results obtained by TEM, which indicates that the nanocomposites are not accurately described by a core-shell architecture with a fully formed shell. However, previous studies show that very thin shells lead to larger oscillation periods than expected due to an

inhomogeneous and porous shell structure.[4] Therefore, the size-dependent acoustic phonon frequencies are best described using a nanocomposite architecture composed of an inhomogeneous, porous gold shell made of aggregated nanoclusters surrounding the TiO_2 core. More work is still needed to accurately determine the morphologies, size distributions, and separation distances of the gold nanoclusters adsorbed to the TiO_2 nanoparticle surface.

Table A.1. The nanocluster shell sizes $s\ (expt)$ measured by TEM for the three TiO_2-Au nanocomposite samples compared to theoretical size predictions from the experimentally measured acoustic phonon oscillations based on individual gold nanospheres of radius $r\ (sphere)$, individual gold nanorods of length $L\ (rod)$, and TiO_2-gold core-shell nanoparticles of shell width $w\ (shell)$.

Sample	s (expt)	r (sphere)	L (rod)	w (shell)
1:1 TiO_2:Au	4.6 ± 0.3 nm	4.3 nm	2.1 nm	5.8 nm
1:2 TiO_2:Au	6.0 ± 0.3 nm	5.8 nm	2.8 nm	9.5 nm
1:3 TiO_2:Au	7.2 ± 0.3 nm	6.9 nm	3.3 nm	12.1 nm

The lifetimes obtained from global analysis fits from the transient absorption spectroscopy results are listed in Table A.2 for the 1:1, 1:2, and 1:3 [TiO_2]:[Au] nanocomposite samples. The acoustic phonon frequencies and the phonon damping times are also included for these three nanocomposite samples. The lifetimes corresponding to electron-phonon scattering, phonon-phonon scattering, the electronic interband transition, and the acoustic phonon damping are all shown to remain constant, to within experimental uncertainty, for the three size-dependent nanocomposites. The electron-transfer lifetimes and the acoustic phonon frequencies are observed to change significantly as the nanocluster gold shell surrounding the TiO_2 core is increased in size.

Table A.2. The lifetimes obtained from the global analysis of the transient absorption results are listed for the different TiO_2-Au nanocomposite samples. The phonon frequencies and phonon damping times are also shown for the three nanocomposite samples.

	1:1 TiO_2:Au	1:2 TiO_2:Au	1:3 TiO_2:Au
τ_{ep}	3.0 ± 0.3 ps	3.3 ± 0.5 ps	3.2 ± 0.2 ps
τ_{pp}	49 ± 6 ps	53 ± 8 ps	55 ± 8 ps
τ_{ib}	7.9 ± 0.3 ps	8.2 ± 0.2 ps	8.5 ± 0.3 ps
τ_{et}	33.1 ± 0.4 ps	7.5 ± 0.1 ps	4.2 ± 0.1 ps
f	0.35 ± 0.02 ps^{-1}	0.26 ± 0.02 ps^{-1}	0.22 ± 0.01 ps^{-1}
τ_d	108 ± 7 ps	106 ± 8 ps	110 ± 7 ps

A.3 References

(1) Voisin, C.; Christofilos, D.; Del Fatti, N.; Vallée, F. Environment Effect on the Acoustic Vibration of Metal Nanoparticles. *Physica B Condens. Matter* **2002**, *316-317*, 89–94.

(2) Wang, L.; Takeda, S.; Liu, C.; Tamai, N. Coherent Acoustic Phonon Dynamics of Gold Nanorods and Nanospheres in a Poly (vinyl Alcohol) Matrix and Their Temperature Dependence by Transient Absorption Spectroscopy. *J. Phys. Chem. C* **2014**, *118*, 1674–1681.

(3) Hu, M.; Wang, X.; Hartland, G. V.; Mulvaney, P.; Juste, J. P.; Sader, J. E. Vibrational Response of Nanorods to Ultrafast Laser Induced Heating: Theoretical and Experimental Analysis. *J. Am. Chem. Soc.* **2003**, *125*, 14925–14933.

(4) Guillon, C.; Langot, P.; Del Fatti, N.; Vallée, F.; Kirakosyan, A. S.; Shahbazyan, T. V.; Cardinal, T.; Treguer, M. Coherent Acoustic Vibration of Metal Nanoshells. *Nano Lett.* **2007**, *7*, 138–142.

Appendix B. Additional In-situ SHG Results

B.1 TEM Images and Size Distributions of Gold Nanoparticles

Figures B.1, B.2, B.3, B.4, and B.5 show additional representative TEM images of gold nanoparticles synthesized from 25, 30, 35, 40, and 50 µL of precursor gold seeds, respectively, where the growth process is monitored using *in-situ* SHG. The TEM images are taken using a JEOL-1400 microscope with carbon-coated copper grids.

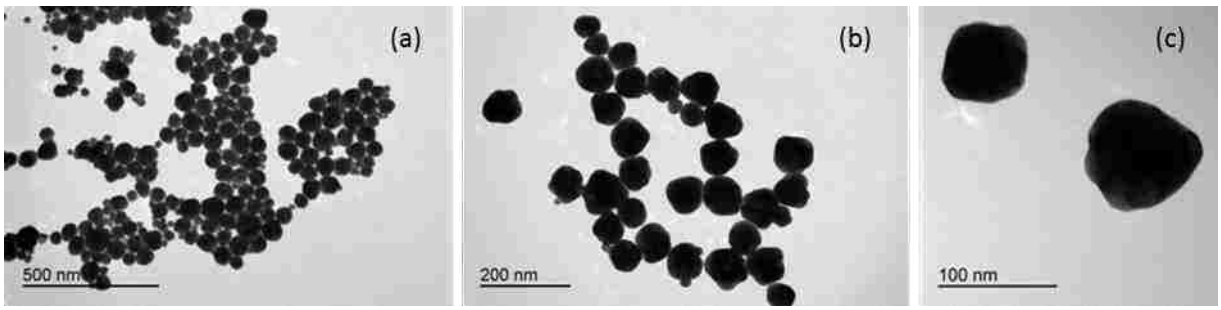

Figure B.1. Additional TEM Images of gold nanoparticles prepared using 25 µL precursor seeds.

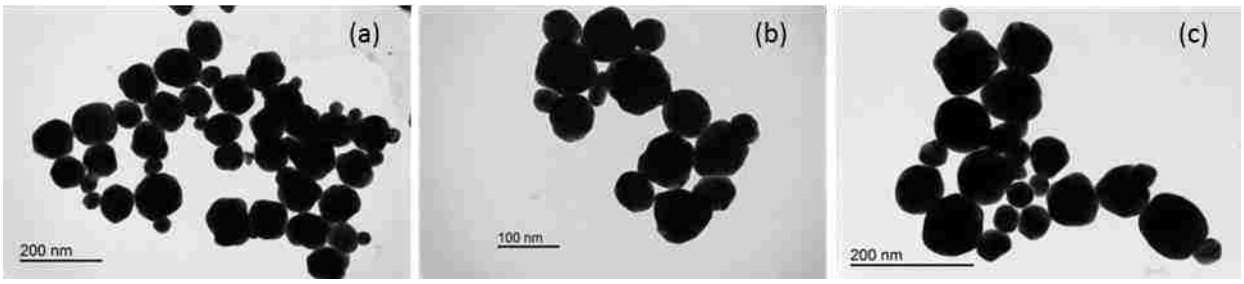

Figure B.2. Additional TEM Images of gold nanoparticles prepared using 30 µL precursor seeds.

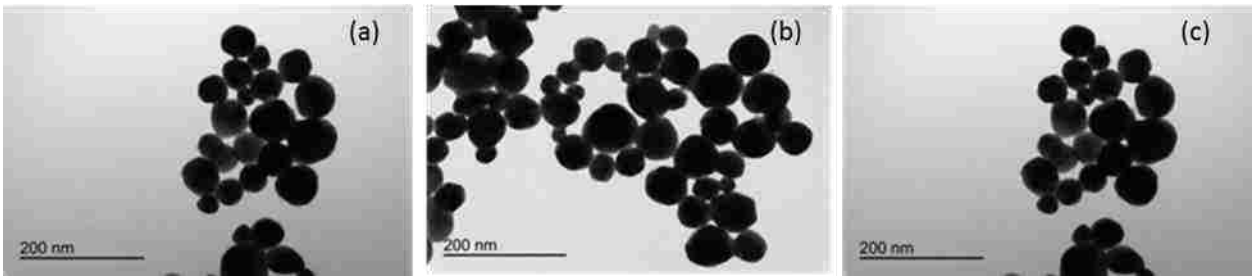

Figure B.3. Additional TEM Images of gold nanoparticles prepared using 35 µL precursor seeds.

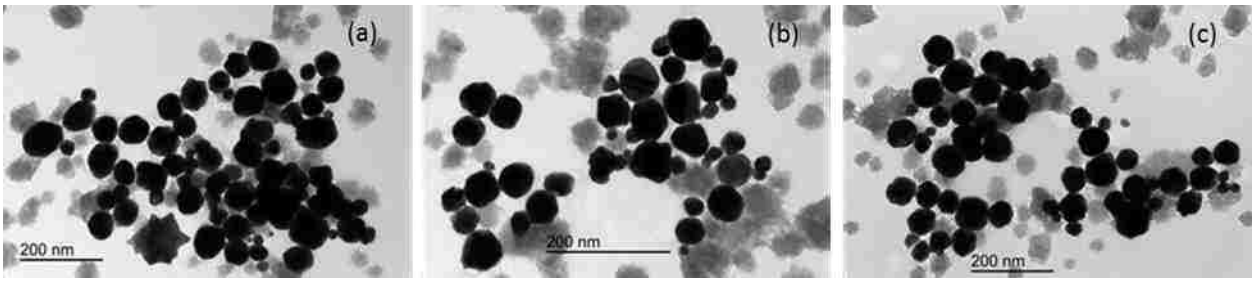

Figure B.4. Additional TEM Images of gold nanoparticles prepared using 40 µL precursor seeds.

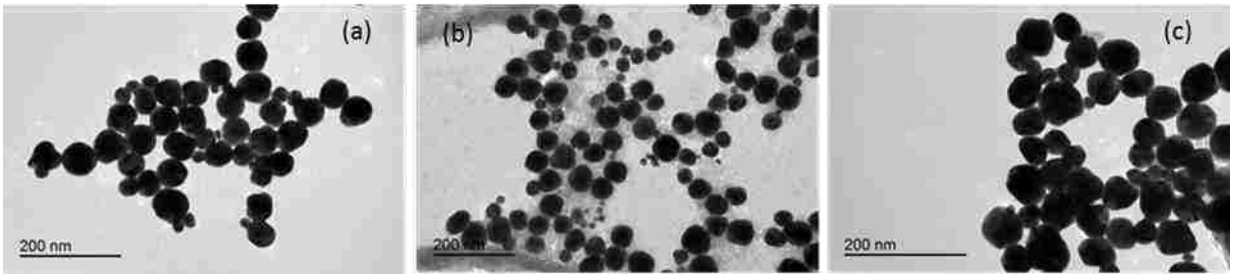

Figure B.5. Additional TEM Images of gold nanoparticles prepared using 50 µL precursor seeds.

The nanoparticle diameter histograms measured with TEM are fit to log-normal functions, shown by dotted lines in Figure S6. The sizes obtained from the fits are 93.2 $\pm$ 4.0 nm, 89.4 $\pm$ 4.3 nm, 74.3 $\pm$ 5.3 nm, 71.3 $\pm$ 4.8 nm, and 64.7 $\pm$ 5.0 nm for the nanoparticles prepared with 25, 30, 35, 40, and 50 µL precursor gold seeds, respectively. Due to the reduced volume and lack of fast stirring in this synthesis in a quartz cuvette with a small stir bar, smaller nanoparticles (21 $\pm$ 3 nm making up less than 15% of the nanoparticles) can be seen in the TEM images from secondary nucleation reactions. These smaller nanoparticles are caused by the slower stirring speeds in the optical cuvette and are not observed under the faster stirring conditions when doing with nanoparticle synthesis in vials with larger stir bars. The overall optical properties of each sample are dominated by the larger nanoparticles as shown by the accurate Mie theory fitting and the larger SHG signals.[1,2]

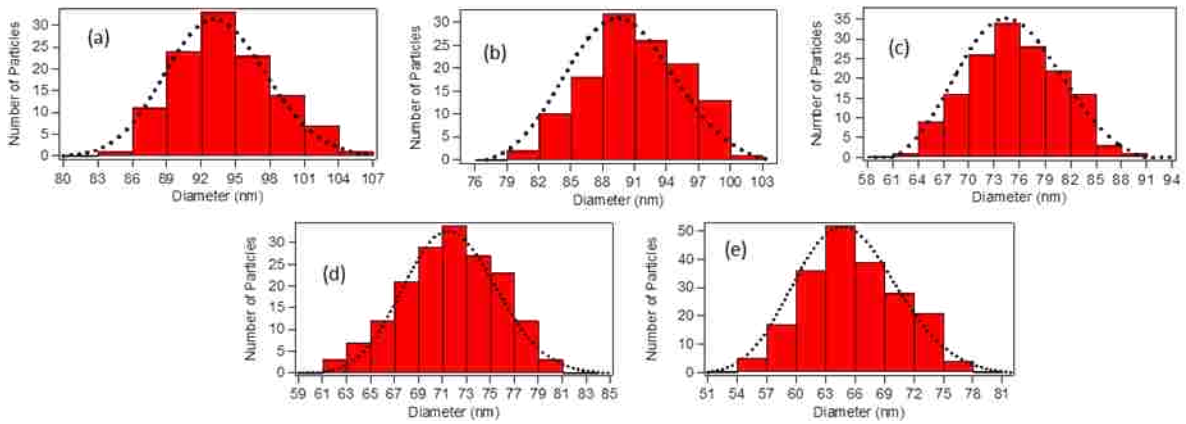

Figure B.6. Size distributions for gold nanoparticles prepared with (a) 25 µL, (b) 30 µL, (c) 35 µL, (d) 40 µL, and (e) 50 µL precursor gold seeds, respectively, and fit with log-normal distributions (dotted lines).

B.2 Analysis of Extinction Spectra and SHG Spectra

Figure B.7 shows the experimental extinction spectra (red line) and the corresponding Mie theory fits (black line) for the nanoparticle samples synthesized with 30, 35, 40, and 50 µL precursor gold seeds with Mie theory sizes of 89, 76, 72, and 66 nm, respectively. The measured diameters from experiment are in good agreement with the diameters obtained from Mie theory analysis.[3,4] The concentrations determined from fitting the final extinction spectrum to Mie theory are 4.46×10^9, 4.54×10^9, 6.45×10^9, 7.60×10^9, and 1.08×10^{10} nanoparticles/mL for the samples with 25, 30, 35, 40, and 50 µL of precursor gold seeds, respectively, using the prepared initial gold seed solution with a concentration of 6.67×10^{11} nanoparticle/mL. The final nanoparticle concentrations are approximately equal to the values obtained when assuming every colloidal seed grows into a larger nanoparticle according to the seed-mediated nanoparticle growth reaction. Figure B.8 shows SHG spectra at selected reaction times during the nanoparticle growth process. The SHG spectra are fit with Gaussian functions with a center wavelength of 400.0 nm and a full width at half-maxima of 4.8 nm, which are in good agreement with our previous SHG studies.[5]

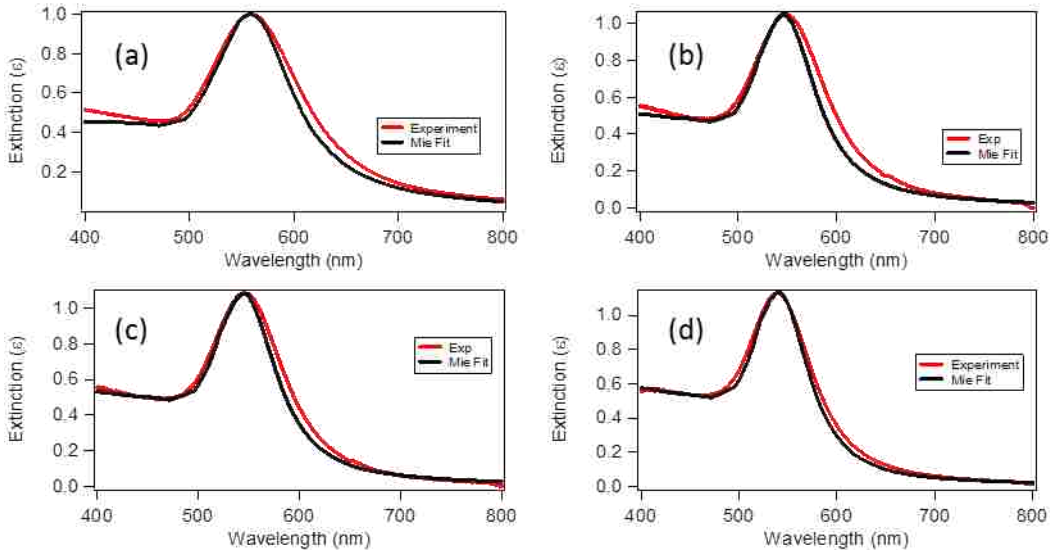

Figure B.7. Final extinction spectra for gold nanoparticles fit using Mie theory for sizes of (a) 89, (b) 76, (c) 72, (d) and 66 nm prepared using 30, 35, 40, 50 µL precursor gold seeds, respectively.

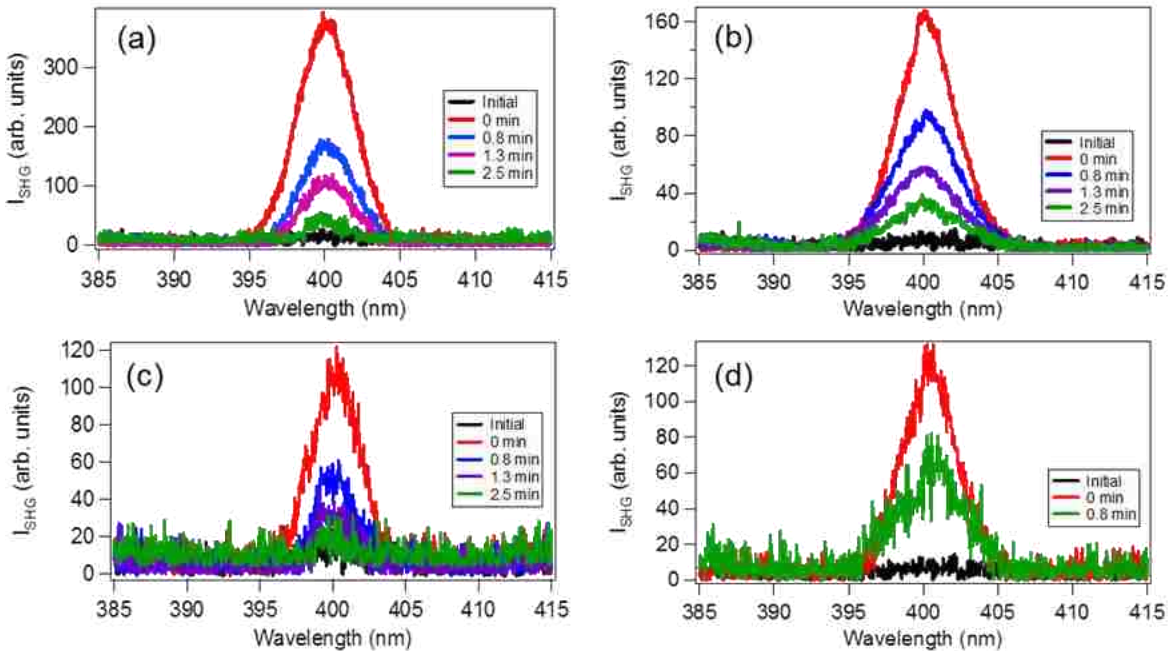

Figure B.8. SHG spectra for gold nanoparticles prepared using (a) 30, (b) 35, (c) 40, and (d) 50 µL precursor gold seeds at selected reaction times.

Figure B.9 shows additional *in-situ* extinction spectra at selected reaction times for gold nanoparticle samples synthesized from 30, 35, 40, and 50 µL precursor seeds. The growth dynamics follow a trend where a broadened red-shifted extinction peak is

observed at early times followed by a narrowing and blue-shifting in the extinction, which is attributed to a rough surface becoming more smooth and reducing in sample polydispersity over time.[6,7]

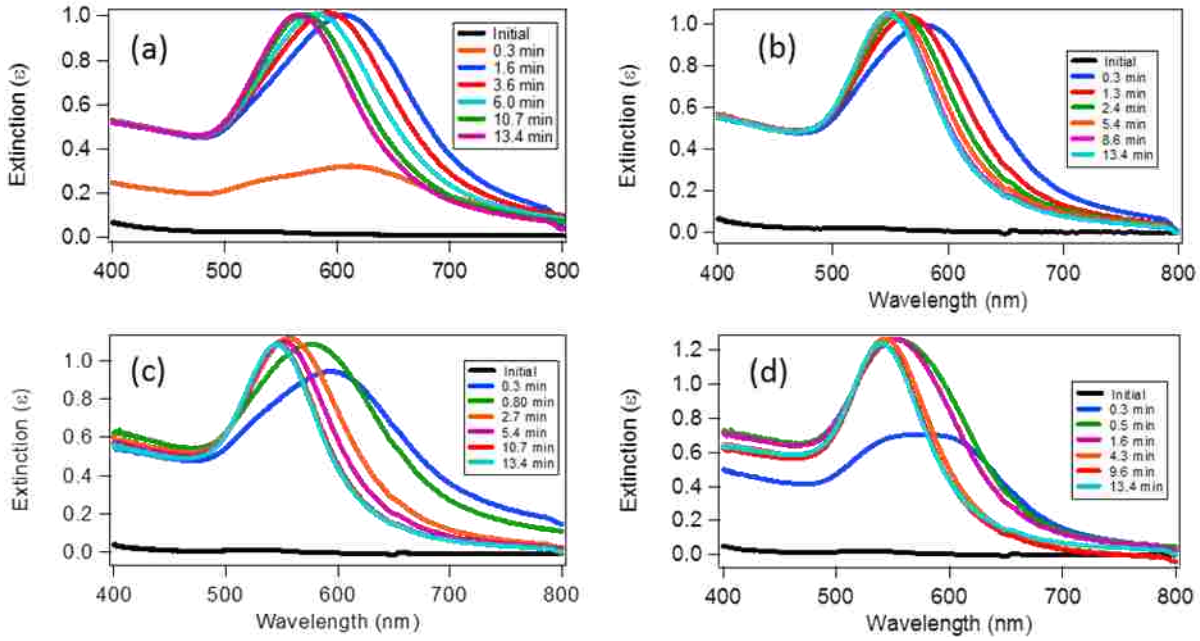

Figure B.9. *In-situ* extinction spectra for gold nanoparticles synthesized from (a) 30, (b) 35, (c) 40, (d) and 50 µL precursor gold seeds at selected reaction times.

B.3 Tabulated Growth Lifetimes from SHG Fits

The size-dependent growth dynamics of the gold nanoparticles are fit using an exponential function to obtain the growth lifetimes. Table B.1 shows the tabulated growth lifetimes τ, amplitudes A, and offsets y_0 from the corresponding fits given by the equation, $E_{SHG}(t) = y_0 + Ae^{-\frac{t}{\tau}}$, with the fits shown in Chapter 3**.** The combined *in-situ* SHG setup and *in-situ* extinction spectroscopy setup is shown in Figure B.10.

Table B.1. Reaction growth lifetimes obtained from fitting the *in-situ* SHG time trace.

Final Diameter (nm)	Growth Lifetime (min)	Amplitude (A)	Offset (y_0)
66.0 ± 4.9	0.37 ± 0.22	83.6 ± 6.8	33.8 ± 0.3
71.7 ± 4.7	0.98 ± 0.03	84.9 ± 3.0	25.2 ± 0.4
74.6 ± 4.8	1.06 ± 0.08	80.1 ± 3.7	32.1 ± 0.5
89.6 ± 4.5	1.50 ± 0.01	113.5 ± 1.5	26.3 ± 0.3
93.7 ± 4.0	1.66 ± 0.01	128.6 ± 1.2	32.3 ± 0.2

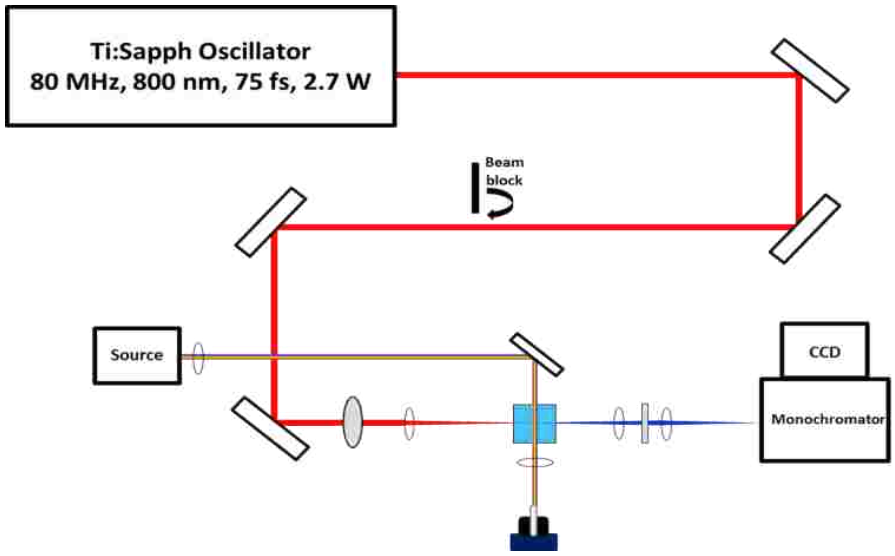

Figure B.10. *In-situ* SHG and extinction experimental setup.

B.4 References

(1) Dadap, J. I.; Shan, J.; Eisenthal, K. B.; Heinz, T. F. Second-Harmonic Rayleigh Scattering from a Sphere of Centrosymmetric Material. *Phys. Rev. Lett.* **1999**, *83*, 4045–4048.

(2) Bohren, C. F.; Huffman, D. R. *Absorption and Scattering of Light by Small Particles*, Wiley-VCH: Weinheim, Germany, 2004.

(3) Karam, T. E.; Haber, L. H. Molecular Adsorption and Resonance Coupling at the Colloidal Gold Nanoparticle Interface. *J. Phys. Chem. C* **2014**, *118*, 642–649.

(4) Perrault, S. D.; Chan, W. C. W. Synthesis and Surface Modification of Highly Monodispersed, Spherical Gold Nanoparticles of 50- 200 Nm. *J. Am. Chem. Soc.* **2009**, *131*, 17042–17043.

(5) Kumal, R. R.; Karam, T. E.; Haber, L. H. Determination of the Surface Charge Density of Colloidal Gold Nanoparticles Using Second Harmonic Generation. *J. Phys. Chem. C* **2015**, *119*, 16200–16207.

(6) Kimling, J.; Maier, M.; Okenve, B.; Kotaidis, V.; Ballot, H.; Plech, A. Turkevich Method for Gold Nanoparticle Synthesis Revisited. *J. Phys. Chem. B* **2006**, *110*, 15700–15707.

(7) Li, J.; Wu, J.; Zhang, X.; Liu, Y.; Zhou, D.; Sun, H.; Zhang, H.; Yang, B. Controllable Synthesis of Stable Urchin-like Gold Nanoparticles Using Hydroquinone to Tune the Reactivity of Gold Chloride. *J. Phys. Chem. C* **2011**, *115*, 3630–3637.

Appendix C. Additional LSMO/STO Results

C.1 LSMO/STO Structures

The bulk rhombohedral structure of crystalline LSMO ($R\bar{3}C$) is shown in Figure C.1.[1] The bulk structure of STO is shown in Figure C.2.[2] The self-assembled LSMO prepared by our collaborators under oxygen deficient conditions possess a 8-10 unit cell interfacial region where the space group is Imma.[3]

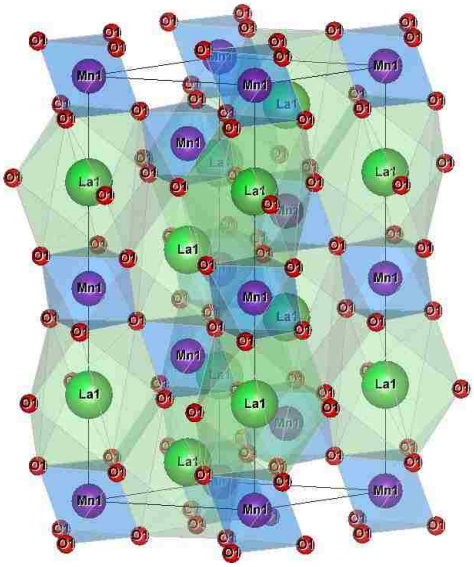

Figure C.1. Bulk structure of LSMO with space group $R\bar{3}C$.

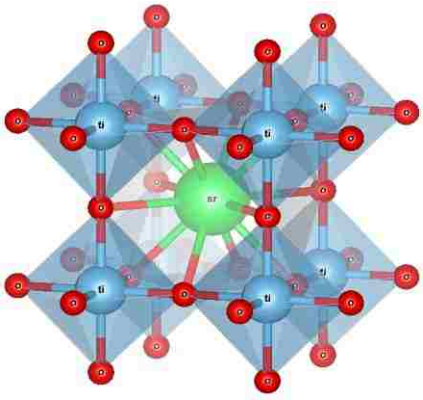

Figure C.2. Bulk Structure of STO with space group Pm3m.

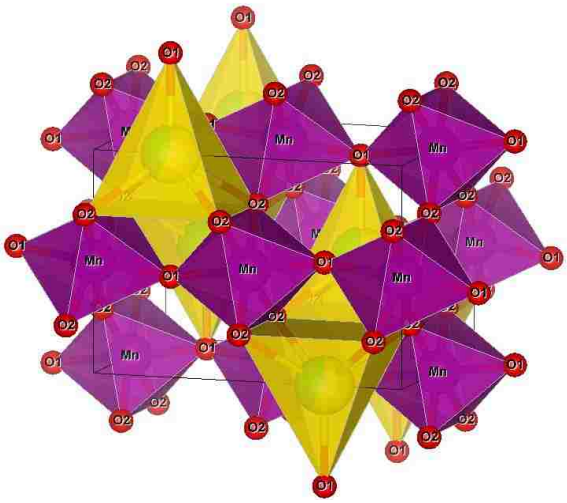

Figure C.3. Interfacial region of LSMO grown on an STO substrate with an Imma space group.

C.2 Tabulated Fitting Results

The biexponential function used to fit the excited-state dynamics of LSMO/STO in Chapter 4 is given by Eq. C.1 where A_{ep}, τ_{ep}, A_{pp}, and τ_{pp} represent the amplitude and lifetime of the electron-phonon coupling as well as the amplitude and lifetime of the phonon-phonon coupling, respectively.

$$R(t) = y_0 + A_{ep}e^{(-t/\tau_{ep})} + A_{pp}e^{(-t/\tau_{pp})} \quad \text{(C.1)}$$

The power dependent lifetimes and amplitudes are presented in Table C.1.

Table C.1. Power-dependent lifetimes obtained from biexponential fitting

Power (mW)	A_{ep}	τ_{ep}	A_{pp}	τ_{pp}	y_0
40	2541±4	46.9±8.2 ps	4415±12	1324±10 ps	442±2
15	1000±1	228±5 ps	1652±5	1074±10	427±26
10	993.6±4.6	314±6 ps	1010±3	1300±9 ps	295±10
8	1101±10	468±7 ps	301.8±6.2	972.8±8.3 ps	458±18

The fast and slow residual oscillations obtained after subtracting the biexponential fitting are fit with Eq. C.2 and Eq. C.3, respectively.

$$R(t) = y_0 + A_{slow}e^{(-t/\tau_{dslow})}\sin(2\pi f_{slow}t + \varphi) \quad \text{(C.2)}$$

$$R(t) = y_0 + A_{fast}e^{(-t/\tau_{dfast})}\sin(2\pi f_{fast}t + \varphi) \quad \text{(C.3)}$$

Where A_{slow}, $\tau_{d,slow}$, and f_{slow} are the slow oscillation amplitude, damping lifetime, and frequency while A_{fast}, $\tau_{d,fast}$, and f_{fast} are the fast oscillation amplitude, damping lifetime, and frequency, respectively. The tabulated fittings for these parameters used to fit the fast and slow oscillations are shown in Table C.2 and C.3, respectively.

Table C.2. Tabulated fitting parameters for fast phonon oscillations.

Power (mW)	A_{fast}	$\tau_{d,fast}$	f_{fast}	φ	y_0
40	297±32	285±35 ps	0.046±0.001 ps^{-1}	1.2±0.1	-3.1±3.7
15	89.3±14.5	377±60 ps	0.046±0.001 ps^{-1}	4.2±0.2	-2.4±1.5
10	64.5±9.7	405±71 ps	0.046±0.001 ps^{-1}	-2.1±0.2	0.15±0.11
8	50.5±9.5	401±64 ps	0.046±0.001 ps^{-1}	3.8±0.2	0.11±0.11

Table C.3. Tabulated fitting parameters for slow phonon oscillations.

Power (mW)	A_{slow}	$\tau_{d,slow}$	f_{slow}	φ	y_0
40	-94.4±41.5	1784±310 ps	0.0034±0.0003 ps^{-1}	-0.95±0.55	-2.1±1.2
15	-80.3±13.5	1027±322 ps	0.0018±0.0001 ps^{-1}	6.9±0.1	-16.6±2.5
10	-42.3±6.5	1526±633 ps	0.0018±0.0004 ps^{-1}	5.4±0.2	-5.3±1.7
8	-31.5±5.8	1250±516 ps	0.0018± 0.0005 ps^{-1}	5.4±0.1	-0.65±0.36

C.3 References

(1) Vailionis, A.; Boschker, H.; Siemons, W.; Houwman, E. P.; Blank, D. H. A.; Rijnders, G.; Koster, G. Misfit Strain Accommodation in Epitaxial O_3 Perovskites: Lattice Rotations and Lattice Modulations. *Phys. Rev. B Condens. Matter* **2011**, *83* (6), 064101.

(2) He, F.; Wells, B. O.; Shapiro, S. M. Strain Phase Diagram and Domain Orientation in SrTiO3 Thin Films. *Phys. Rev. Lett.***2005**, *94*, 176101.

(3) Saghayezhian, M. Manipulating Physical Properties of Complex Materials By Processing, Louisiana State University (2017).

Appendix D. Ultrafast Melting Dynamics of Aluminum and Silicon

D.1 Tabulated Fitting Values

The power-dependent lifetimes and reflectivity constants from the ultrafast reflectivity measurements of the Al thin film sample, corresponding to Figure 5.5, are fit to the single-exponential function $\Delta R = A + Be^{(-\frac{t}{\tau})}$, where A, B, and τ are the offset, amplitude, and electron-phonon coupling lifetime. Table D.1 shows these fitting values and corresponding errors.

Table D.1. Tabulated fitting values for heating and melting dynamics on the aluminum thin film.

Power (μJ)	A	B	τ
0.5	612 ± 347	N/A	N/A
1.0	913 ± 439	N/A	N/A
1.5	1185 ± 251	N/A	N/A
2.0	1210 ± 241	N/A	N/A
2.5	1189 ± 24	859 ± 278	33.5 ± 12.7 ps
3.0	648 ± 162	1505 ± 128	250.6 ± 68.6 ps
3.5	575 ± 28	586 ± 62	119.9 ± 27.8 ps
4.0	637 ± 22	609 ± 160	50.2 ± 17.6 ps

The power-dependent lifetimes and reflectivity constants obtained from fitting the ultrafast reflectivity time traces from Si, corresponding to Figure 5.7, using the same single-exponential function, are listed in Table D.2 along with errors.

Figure D.2. Tabulated fitting values for heating and melting dynamics on Si (001) single crystal.

Power (μJ)	A	B	τ
2.0	-264 $\pm$ 88	N/A	N/A
3.0	-333 $\pm$ 33	N/A	N/A
4.0	-363 $\pm$ 10	-275 $\pm$ 35	55.1 $\pm$ 12.3 ps
5.0	-8.1 $\pm$ 5.9	-54 $\pm$ 19	229 $\pm$ 180 ps

Appendix E: Publication Agreements and Permission

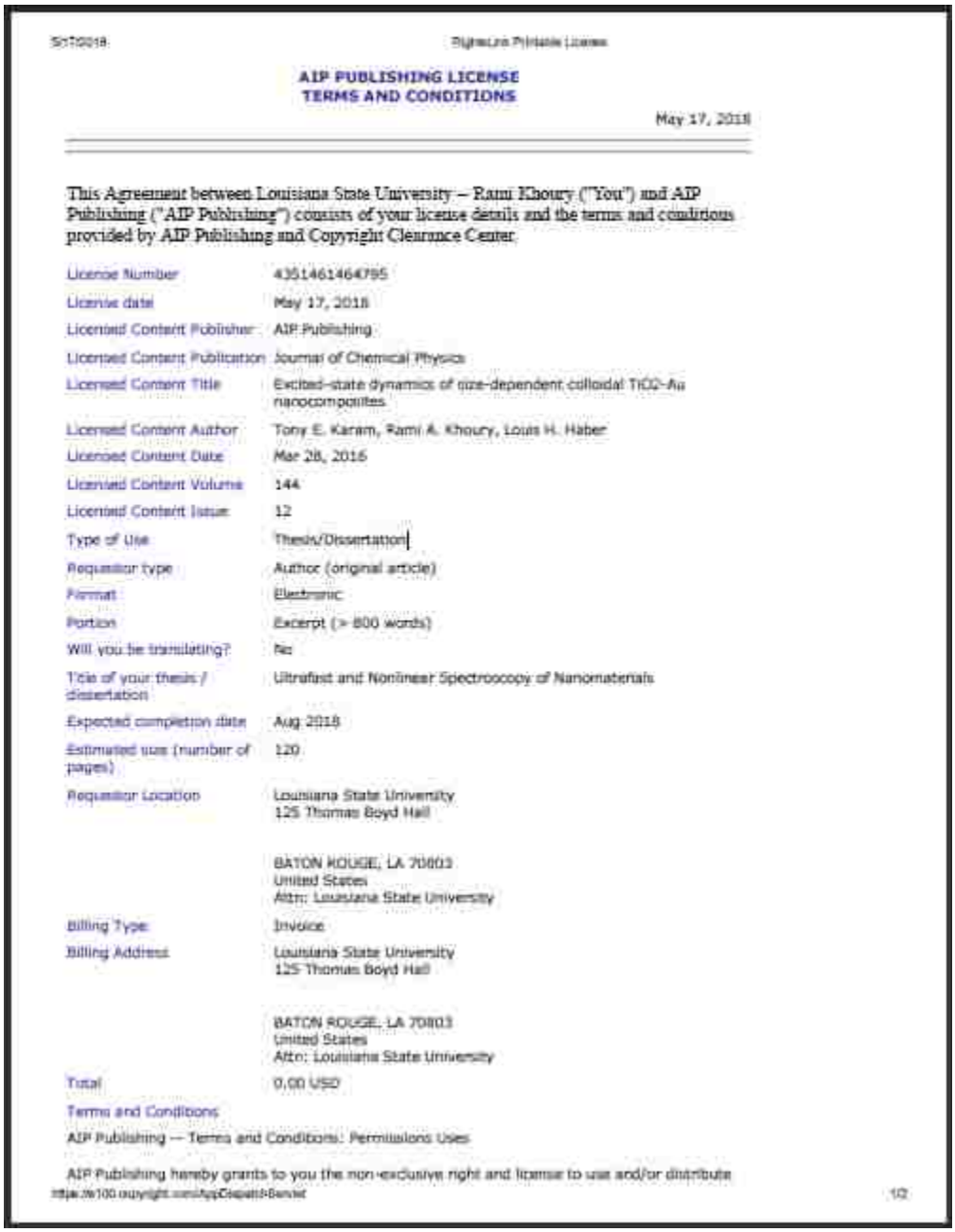

5/17/2018 RightsLink Printable License

AIP PUBLISHING LICENSE TERMS AND CONDITIONS

May 17, 2018

This Agreement between Louisiana State University – Rami Khoury ("You") and AIP Publishing ("AIP Publishing") consists of your license details and the terms and conditions provided by AIP Publishing and Copyright Clearance Center.

License Number	4351461464795
License date	May 17, 2018
Licensed Content Publisher	AIP Publishing
Licensed Content Publication	Journal of Chemical Physics
Licensed Content Title	Excited-state dynamics of size-dependent colloidal TiO2-Au nanocomposites
Licensed Content Author	Tony E. Karam, Rami A. Khoury, Louis H. Haber
Licensed Content Date	Mar 28, 2016
Licensed Content Volume	144
Licensed Content Issue	12
Type of Use	Thesis/Dissertation
Requestor type	Author (original article)
Format	Electronic
Portion	Excerpt (> 800 words)
Will you be translating?	No
Title of your thesis / dissertation	Ultrafast and Nonlinear Spectroscopy of Nanomaterials
Expected completion date	Aug 2018
Estimated size (number of pages)	120
Requestor Location	Louisiana State University 125 Thomas Boyd Hall BATON ROUGE, LA 70803 United States Attn: Louisiana State University
Billing Type	Invoice
Billing Address	Louisiana State University 125 Thomas Boyd Hall BATON ROUGE, LA 70803 United States Attn: Louisiana State University
Total	0.00 USD

Terms and Conditions

AIP Publishing – Terms and Conditions: Permissions Uses

AIP Publishing hereby grants to you the non-exclusive right and license to use and/or distribute

https://s100.copyright.com/AppDispatchServlet 1/2

the Material according to the use specified in your order, on a one-time basis, for the specified term, with a maximum distribution equal to the number that you have ordered. Any links or other content accompanying the Material are not the subject of this license.

1. You agree to include the following copyright and permission notice with the reproduction of the Material:"Reprinted from [FULL CITATION], with the permission of AIP Publishing." For an article, the credit line and permission notice must be printed on the first page of the article or book chapter. For photographs, covers, or tables, the notice may appear with the Material, in a footnote, or in the reference list.
2. If you have licensed reuse of a figure, photograph, cover, or table, it is your responsibility to ensure that the material is original to AIP Publishing and does not contain the copyright of another entity, and that the copyright notice of the figure, photograph, cover, or table does not indicate that it was reprinted by AIP Publishing, with permission, from another source. Under no circumstances does AIP Publishing purport or intend to grant permission to reuse material to which it does not hold appropriate rights.
   You may not alter or modify the Material in any manner. You may translate the Material into another language only if you have licensed translation rights. You may not use the Material for promotional purposes.
3. The foregoing license shall not take effect unless and until AIP Publishing or its agent, Copyright Clearance Center, receives the Payment in accordance with Copyright Clearance Center Billing and Payment Terms and Conditions, which are incorporated herein by reference.
4. AIP Publishing or Copyright Clearance Center may, within two business days of granting this license, revoke the license for any reason whatsoever, with a full refund payable to you. Should you violate the terms of this license at any time, AIP Publishing, or Copyright Clearance Center may revoke the license with no refund to you. Notice of such revocation will be made using the contact information provided by you. Failure to receive such notice will not nullify the revocation.
5. AIP Publishing makes no representations or warranties with respect to the Material. You agree to indemnify and hold harmless AIP Publishing, and their officers, directors, employees or agents from and against any and all claims arising out of your use of the Material other than as specifically authorized herein.
6. The permission granted herein is personal to you and is not transferable or assignable without the prior written permission of AIP Publishing. This license may not be amended except in a writing signed by the party to be charged.
7. If purchase orders, acknowledgments or check endorsements are issued on any forms containing terms and conditions which are inconsistent with these provisions, such inconsistent terms and conditions shall be of no force and effect. This document, including the CCC Billing and Payment Terms and Conditions, shall be the entire agreement between the parties relating to the subject matter hereof.

This Agreement shall be governed by and construed in accordance with the laws of the State of New York. Both parties hereby submit to the jurisdiction of the courts of New York County for purposes of resolving any disputes that may arise hereunder.

V1.2

Questions? customercare@copyright.com or +1-855-239-3415 (toll free in the US) or +1-978-646-2777.

Permission to Publish Joint Work

LH Louis H Haber
Today, 12:49 PM
Rami A Khoury

Reply all

Dear Rami,

Yes, I give my permission for you to use this publication, Karam, T. E.; Khoury, R. A.; Haber, L. H. Excited-State Dynamics of Size-Dependent Colloidal TiO2-Au Nanocomposites, J. Chem. Phys. 2016, 144 (12), 124704, in your thesis. Please let me know if you need any additional information on this.

Best regards,
Louis Haber

Get Outlook for iOS

RK Rami A Khoury
Today, 12:22 PM

Hi Dr. Haber,

I am writing to request permission to publish our joint work in my PhD dissertation under the citation: Karam, T. E., Khoury, R. A., Haber, L. H. Excited-State Dynamics of Size-Dependent Colloidal TiO2-Au Nanocomposites. *J. Chem. Phys.* 2016, *144* (12), 124704. If you are okay with this please write back confirming that you give me permission and just in case please restate the bibliographic citation.

Kind Regards,
Rami Khoury

Permission to Publish Joint Work

TK Tony Karam <tonykaram2@hotmail.com>
Yesterday, 6:07 PM
Rami A Khoury

Reply all

Dear Dr. Rami Khoury,

I grant you permission to publish our joint work in your PhD dissertation under the citation: Karam, T. E.; Khoury, R. A.; Haber, L. H. Excited-State Dynamics of Size-Dependent Colloidal TiO2-Au Nanocomposites. *J. Chem. Phys.* 2016, *144* (12), 124704.

Best regards,
Tony Karam

-------- Original message --------
From: Rami A Khoury <rkhour1@lsu.edu>
Date: 7/29/18 6:49 PM (GMT-05:00)
To: 'Tony Karam' <tonykaram2@hotmail.com>
Subject: Permission to Publish Joint Work

Hi Dr. Karam,
I am writing to request permission to publish our joint work in my PhD dissertation under the citation: Karam, T. E., Khoury, R. A., Haber, L. H. Excited-State Dynamics of Size-Dependent Colloidal TiO2-Au Nanocomposites. *J. Chem. Phys.* 2016, *144* (12), 124704. If you are okay with this please write back confirming that you give me permission and just in case please restate the bibliographic citation.

Kind Regards,
Rami Khoury

Vita

Rami Anthony Khoury majored in Chemistry at Louisiana State University, receiving his B.S. in Chemistry with a concentration in Education in 2012 with a license to teach secondary education. Following his undergraduate career, he worked as a Research Assistant at Lawrence Berkeley National Laboratory under the direction of Dr. Robert Kaindl where he studied carrier-envelope phase stabilization for the generation of attosecond pulses. He is currently pursuing a Ph.D. in Physical Chemistry as a doctoral candidate in the Haber research group at Louisiana State University. Upon competition of his Ph.D. he will be working at nLight as a fiber laser development engineer.